TECHNISCHE UNIVERSITÄT MÜNCHEN

Physik-Department
Lehrstuhl für Funktionelle Materialien

Nanostructures for polymer-based organic photovoltaics

Shuai Guo, M.Sc.

Vollständiger Abdruck der von der Fakultät für Physik der Technischen Universität München zur Erlangung des akademischen Grades eines

Doktors der Naturwissenschaften (Dr. rer. nat.)

genehmigten Dissertation.

Vorsitzender:	Univ.-Prof. Dr. Martin Zacharias
Prüfer der Dissertation:	1. apl. Prof. Dr. Peter Müller-Buschbaum
	2. apl. Prof. Dr. Martin S. Brandt

Die Dissertation wurde am 06.11.2014 bei der Technischen Universität München eingereicht und durch die Fakultät für Physik am 12.12.2014 angenommen.

Abstract

In this thesis, polymer:fullerene bulk heterojunction photoactive films and the corresponding solar cells are investigated for photovoltaic applications. The morphology of the active layer is widely recognized as a key factor influencing the overall photovoltaic performance of polymer-based solar cells. Thus, the focus of the present work is to elucidate the relationship between morphology and power conversion efficiency by intentionally varying external parameters during the processing. Both real and reciprocal space investigation techniques are applied in order to obtain the resulting representative morphology models. It is observed that the active layer morphology of the investigated PTB7:$PC_{71}BM$ bulk heterojunction system can be easily manipulated by a slight chemical modification of the used polymer, the usage of host solvent, or an additional solvent treatment, consequently leading to different device efficiencies. The reason for this sensitive alternation is mainly addressed in the present work.

Zusammenfassung

In dieser Arbeit werden Filme mit Polymer:Fulleren Bulk-Heteroübergang und die zugehörigen Solarzellen im Hinblick auf Anwendungen in der Photovoltaik untersucht. Die Morphologie der aktiven Schicht ist als wichtiger Faktor bekannt, der die photovoltaische Leistung polymerbasierter Solarzellen beeinflusst. Deshalb liegt der Fokus dieser Arbeit darin, die Beziehung zwischen Morphologie und Wirkungsgrad durch gezielte Beeinflussung der Prozessparameter zu untersuchen. Durch Untersuchungstechniken sowohl im realen, als auch im reziproken Raum, werden repräsentative Morphologiemodelle erstellt. Dabei wird beobachtet, wie die Morphologie der aktiven Schicht in dem untersuchten System eines PTB7:$PC_{71}BM$ Bulk-Heteroübergangs durch leichte chemisch Veränderungen des Polymers, der Nutzung von Änderung des Hauptlösemitteln oder zusätzlicher Lösemittelbehandlung beeinflusst werden kann und somit zu unterschiedlichen Effizienzen der Bauteile führt. Der Hintergrund dieser empfindliche Änderungen ist Hauptgegenstand der vorliegenden Arbeit.

Contents

List of abbreviations

AFM:	atomic force microscopy
BHJ:	bulk heterojunction
CB:	chlorobenzene
DB:	1,2-dichlorobenzene
DIO:	1,8-diiodooctane
DOS:	density of states
DWBA:	distorted wave Born approximation
FF:	fill factor
FTO:	fluorine doped tin oxide
FWHM:	full width at half maximum
GISAXS:	grazing incidence small angle X-ray scattering
GIWAXS:	grazing incidence wide angle X-ray scattering
HOMO:	highest occupied molecular orbital
HSPs:	Hansen solubility parameters
J_{sc}:	short circuit current
ITO:	indium tin oxide
IV curve:	current-voltage curve
LMA:	local monodisperse approximation
LUMO:	lowest unoccupied molecular orbital
M_w:	molecular weight
OFET:	organic thin-film transistor
OPV:	organic photovoltaic
PCE:	power conversion efficiency
$PC_{61}BM$:	[6,6]-phenyl-C61-butyric acid methyl ester
$PC_{71}BM$:	[6,6]-phenyl-C71-butyric acid methyl ester
PDI:	polydispersity
PEDOT:PSS:	poly(3,4-ethylenedioxythiophene):poly(styrenesulfonate)
PFN:	poly[(9,9-bis(3'-(N,N-dimethylamino)propyl)-2,7-fluorene)-alt-2,7-(9,9-dioctylfluorene)]

PPV:	poly(p-phenylene-vinylene)
PSD:	power spectral density
PTB7:	poly[[4,8-bis[(2-ethylhexyl)oxy]benzo[1,2-b:4,5-b']dithiophene-2,6-diyl][3-fluoro-2-[(2-ethylhexyl)carbonyl]-thieno[3,4-b]thiophenediyl]]
PV:	photovoltaic
PVDF:	polyvinylidene fluoride
P3HT:	poly(3-hexylthiophene-2,5-diyl)
RED:	relative energy difference
SDD:	sample detector distance
SEM:	scanning electron microscope
SLD:	scattering length density
TB:	1,2,4-trichlorobenzene
TOF-GISANS:	time of flight-grazing incidence small angle neutron scattering
UV/Vis:	ultraviolet/visible spectroscopy
V_{oc}:	open circuit voltage
XRD:	X-ray diffraction
XRR:	X-ray reflectivity

Chapter 1

Introduction

In order to harvest the natural energy sources, tremendous investigations on renewable energy have expanded into various fields, ranging from solar electricity, fuel, biomass, wind, tides, waves and geothermal energy. Among all, solar energy is considered as the largest renewable source without producing greenhouse gases and therefore a potential key to meet future energy needs.[1] Statistics show that the total solar energy received on earth in one hour is more than the total energy consumption all over the world in one year.[2] Many technologies have been explored to make use of solar energy, such as solar heating, solar thermo-electricity and solar photovoltaic (PV). Since electricity already has a well-established distribution network in most parts of the world, and thus can be easily transported, which has paved solid foundations for the development of PV technology. At present, the PV market is mostly dominated by inorganic systems such as thick polycrystalline silicon devices, as they show advantages in both efficiency in excess of 20% and the operation lifetime of more than 25 years.[3] However, the high energy consumption and consequently the high manufacturing cost become the hurdle for the wide implementation of polycrystalline silicon PV devices.

Organic photovoltaic (OPV), emerged as a relatively new PV technology. It has experienced rapid progress regarding the device efficiency and lifetime in the past two decades. OPV is based on organic molecules, which is widely used for organic thin-film transistor (OFET), organic light emitting diode (OLED) and photodetectors as well.[4] OPV demonstrates its competence by the dramatic improvement on device performance, promising potential to fabricate the solar cells at low cost with roll-to-roll technique, and rapid energy payback time.[5] Furthermore, the excellent mechanical flexibility and the light weight bring more conveniences for daily use.

In general, OPV mainly refers to polymer:fullerene solar cells, polymer:polymer solar cells, polymer:small organic molecules solar cells, and pure small organic molecules solar

cells. As one of the main components of OPV, polymers are commonly known as insulating materials. In 19th century, a striking discovery of conductive polymer polyacetylenes was made by Shirakawa et al.,[6] who were awarded with Nobel prize in Chemistry in the year 2000. Ever since the announcement of this significant discovery, researches on the use and understanding of conductive polymers has grown intensively. Considering the architecture of OPV, Yu et al. firstly employed only one conductive polymer as the photon-induced electricity layer, which gave rise to very low power conversion efficiency (PCE).[4] This issue was addressed soon by Sariciftci et al. with introducing the second organic material in a bilayer geometry, which greatly promoted the overall PCE due to a more efficient charge separation process.[7, 8] However, due to the short exciton diffusion length (10-20 nm), the thickness of this bilayer geometry device is limited within 20 nm to assure a high charge separation rate. As a result, the amount of photons absorbed by this ultra-thin active layer is not optimized. To overcome this problem with sustaining the high excition separation rate realized by the interfaces, a bulk heterojunction (BHJ) concept of blending two organic materials is tested and shown to be the most successful geometry in an active layer to date.[9, 10] However, it is challenging to control the film morphology of a BHJ active layer as it is based on a self-assembly solution drying process. It is widely recognized that the final device efficiency is directly determined by the intrinsic property of used materials and solvents, the preparation conditions, as well as additional post-treatment such as thermal annealing or solvent treatment. The theoretical ideal geometry for higher PCE organic photovoltaic is the interdigitated two components with the length scale on the order of the excition diffusion length such as 10 nm.

In order to optimize the efficiency of polymer solar cells and cross the 10% PCE threshold for commerical appplication of this technique, rapid development especially in chemicial synthesis field has been evident. PCE around 0.1% was firstly obtained from poly(p-phenylene-vinylene) (PPV) system, and further reached about 4% for prototype P3HT:PCBM (poly(3-hexylthiophene-2,5-diyl):[6,6]-phenyl-C61 butyric acid methyl ester) BHJ system, until the recent success in synthesizing low bandgap polymers with reaching almost 10%, an increase in efficiency was gained.[11, 12, 13] The presence of low bandgap polymers has greatly drawn the efficiency chart of OPVs to a promising region. Poly[[4,8-bis[(2-ethylhexyl)oxy]benzo[1,2-b:4,5-b']dithiophene-2,6-diyl][3-fluoro-2-[(2-ethylhexyl)carbonyl]-thieno[3,4-b]thiophenediyl]], denoted as PTB7, represents one of the highly efficient low bandgap polymers. Although the efficiencies of solar cells made of PTB7 has proved its speciality, the understanding on PTB7 system are still very limited. In order to better understand this newly ermerged polymer and the mechanism behind its excellent efficiency, PTB7 is selected as the p-type electron donor material throughout the whole investigation.

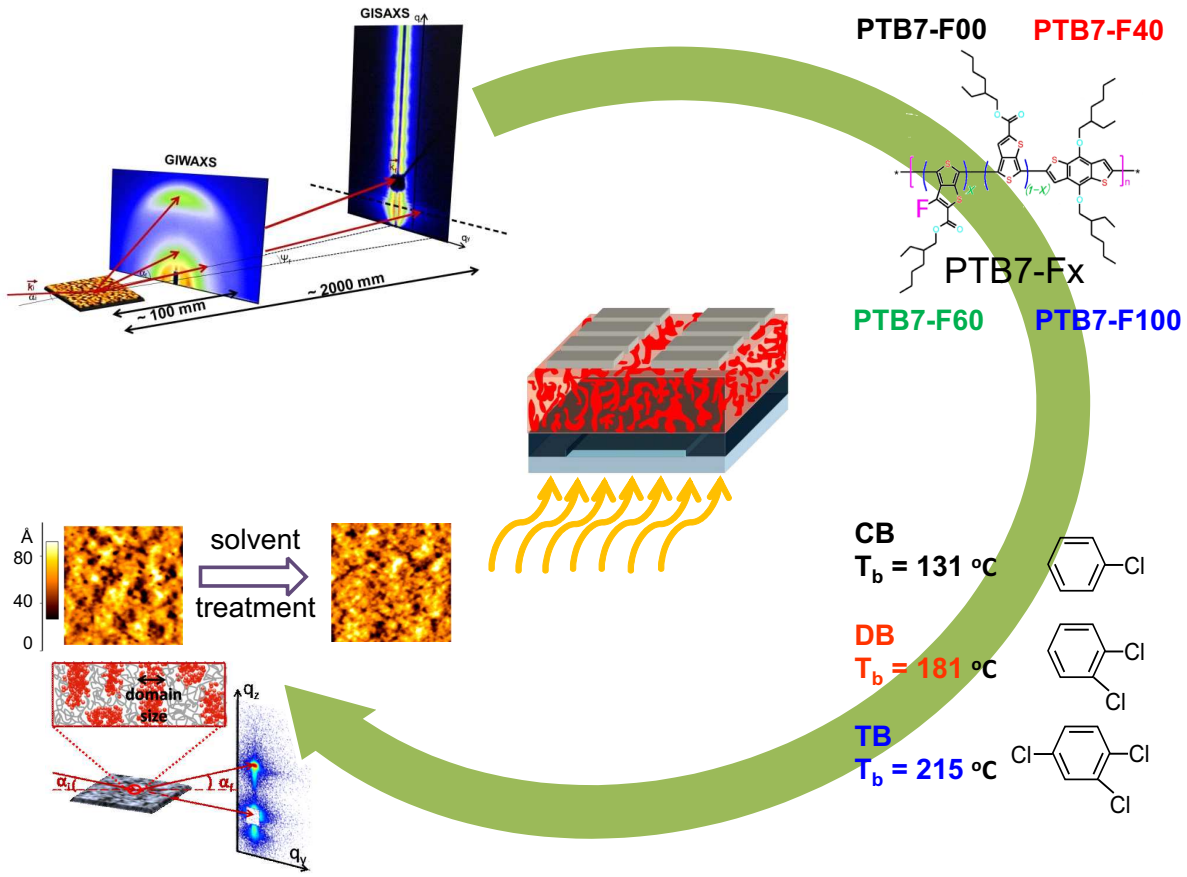

Figure 1.1: *Schematic illustration of an organic solar cell (center). Clockwise, an overview of the different material combinations investigated within the framework of this thesis. More details regarding each topic are introduced in the text.*

In Figure 1.1, an overview of the different projects investigated in this thesis is illustrated. In the center an exemplary polymer based solar cell is schematically displayed. A polymer based solar cell typically has a multilayer architecture, which consists of an active layer, electron/hole blocking layers, and electrodes. As it is well recognized that the morphology of the active layer is of utmost significance for the overall device efficiency of OPV, several general questions are to be elucidated in this thesis: What parameters can affect the PCE of the organic solar cells? To what extent can these parameters influence the film morphology? What is the property-morpholgy-efficiency relationship? Is there a golden rule to optimize the PCE of PTB7:PCBM BHJ organic photovoltaic? To answer the questions, the access of the whole photoactive film morphology based on the nanostructure is highly important. However, traditional imaging techniques cannot provide the information of inner film, where the main energy conversion process occurs. Therefore, advanced X-ray or neutron scattering techniques are particularly included to solve this

challenging problem. An exemplary X-ray scattering setup mainly used in this thesis is depicted on the left corner of Figure 1.1. Consequently, the device performance of the novel PTB7:$PC_{71}BM$ BHJ system and its dependence on the molecular structure of the polymers, the selection of the host solvent, and post solvent treatment are systematically investigated. The focus of this thesis is to correlate the different efficiencies with the resulting morphology induced by above mentioned parameters.

To start with, the theoretical background covering the working principle of OPV, properties of polymers, phase diagram of the used materials and solvents, as well as scattering basics are illustrated in chapter 2. All the involved characterization techniques and the sample preparation procedures are introduced in chapter 3 and 4, respectively. The highlight part of this thesis, namely, the investigation results based on PTB7:$PC_{71}BM$ BHJ system with different focuses are presented from chapter 5 to 7 consecutively. The corresponding representative sketch of each investigated theme is placed clockwisely in Figure 1.1.

First, the used polymer is varied by modifying the amount of fluorine content along the polymer backbone, whereas other components are kept unchanged such as the used fullerene part ($PC_{71}BM$) and the host solvent (chlorobenzene). Accordingly, active layers spin-coated from the blend of polymer PTB7-Fxx:$PC_{71}BM$ without and with solvent additive DIO are thoroughly investigated. The impact of fluorine content is therefore correlated with the corresponding device performance as detailed in chapter 5.

Second, the influence of the used host solvent on the solar cell performance is studied by using polymer PTB7-F40 blended with $PC_{71}BM$. Three commonly used solvents: chlorobenzene, 1,2-dichlorobenzene and 1,2,4-trichlorobenzene are tested without and with the addition of the solvent additive DIO on the pure polymer PTB7 and PTB7:$PC_{71}BM$ BHJ system, respectively. The best solvent for particular PTB7:$PC_{71}BM$ BHJ solar cells is identified, and the resulting morphology-efficiency relationship is addressed as well. The corresponding investigation is presented in chapter 6.

Third, to further improve the solar cell efficiency of the PTB7:$PC_{71}BM$ BHJ system, additional facile solvent treatments are applied and shown to be an effective method. For the first time a systematic study of the effect of solvent treatment with a series of four different alcohol solvents on the polymer solar cell efficiency is reported. The reason for the efficiency enhancement induced by alcohol solvent treatment is addressed in detail in chapter 7.

In the end, the conclusion completes the whole systematic investigation and additionally the outlook points out the direction for the future researches concerning the OPV as present in chapter 8.

Chapter 2

Theoretical aspects

Prior to the introduction of the specific topics investigated in this thesis, the theoretical background applied throughout the thesis is presented in this chapter. In section 2.1, the basic working principles of organic solar cells starting from the preliminary light absorption to the final charge extraction are explained systemically. In section 2.2, the theories about relatively new low bandgap polymers used in this thesis are introduced; Moreover, the physical phenomena which are typical for low bandgap polymers in the thin film state such as phase segregation and polymer crystallization are also discussed. In section 2.3, the advanced X-ray and neutron scattering techniques in the grazing incidence mode used for structure investigations of thin polymer films are elucidated.

2.1 Organic photovoltaics

Photovoltaics represent the type of optoelectronic devices which convert solar radiation into electricity. By using organic materials (i.e. carbon-based polymers or compounds) instead of traditional silicon based materials, organic photovoltaics have attracted tremendous attention in the past decades. Literally, organic photovoltaics comprise all types of solar cells where organic materials are included in the light absorbing layer, e.g. polymer-fullerene solar cells, polymer-polymer solar cells, and hybrid solar cells (organic-inorganic solar cells). In this thesis, organic photovoltaics only refer to polymer-fullerene BHJ solar cells. This section is structured in the following way: First, an overview of organic photovoltaics including the device physics and the photo-induced charge carriers generation process is presented in section 2.1.1; Next, the commonly recognized charge carriers generation is illustrated in detail, that is, light absorption and exciton generation (section 2.1.2), exciton diffusion (section 2.1.3), exciton dissociation (section 2.1.4),

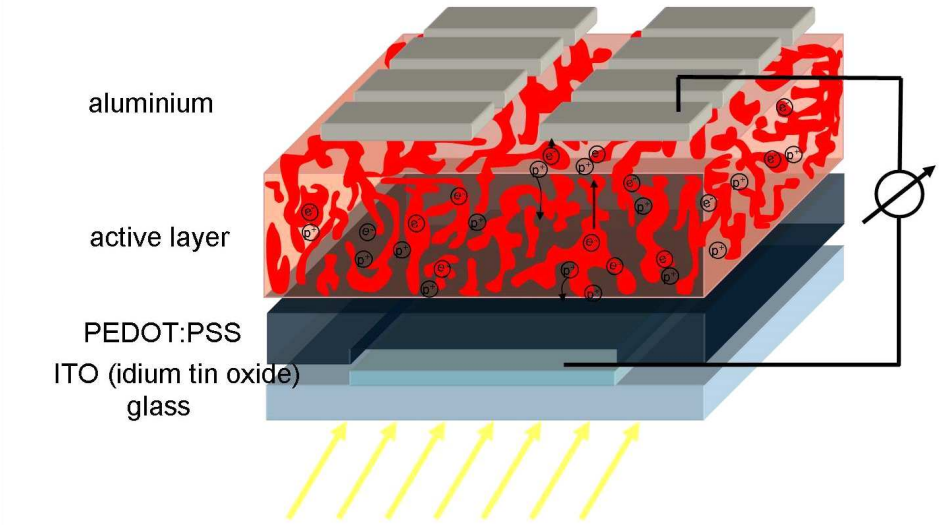

Figure 2.1: *Representative sketch of polymer-based solar cell.*

charge carrier transport (section 2.1.5), and charge carrier extraction (section 2.1.6). In addition, a summary of possible loss mechanisms in organic photovoltaics is discussed in section 2.1.7.

2.1.1 Basic principles

Organic photovoltaics are typically multilayer devices as seen in Figure 2.1. A polymer-based solar cell normally consists of one active layer, two electrodes, and functional layers. The active layer is responsible for the light conversion process, which is based on the semiconducting nature of the used polymers. Transparent conducting oxides such as ITO (indium tin oxides) or FTO (fluorine doped tin oxide) are commonly used as one electrode, whereas ultra-thin metal materials like aluminum, silver, or gold are the counter electrode. Between the electrodes and the active layer, the optical spacer (TiOx), and the electron (PEDOT:PSS) or hole blocking layer (PFN) are sometimes applied to enhance the light absorption and assist the charge transport efficiency.[14, 15] The fabrication procedure of the whole polymer solar cell can be found in Chapter 4.3.

As the most crucial layer in the organic photovoltaic device, the active layer converts the light into electricity by the semiconducting properties of the carbon based materials, which are, in our case, made from the mixture of conducting polymers and fullerene derivatives. It is well-known that most polymers are insulators such as polystyrene. However, some insulating polymers like polyacetylene can become semiconducting or even

conducting by doping due to increased number of free charge carriers. Consequently, binding and anti-binding states are generated in the conducting polymers, which results in the highest occupied molecular orbital (HOMO) level and lowest unoccupied molecular orbital (LUMO) level with an energy bandgap of E_g. Details about polymer band gap can be found in section 2.2. In Figure 2.2, a multi-step electricity generation process of a polymer solar cell is depicted.

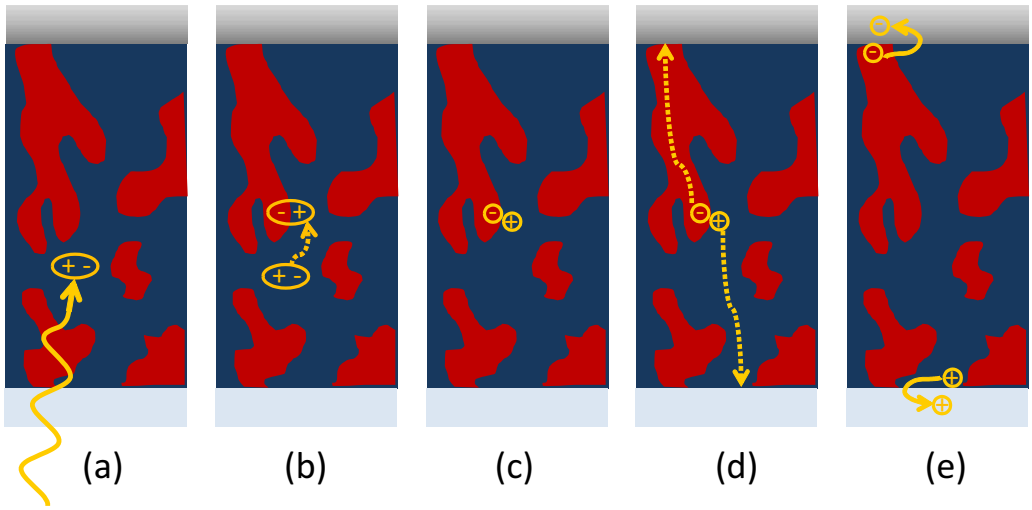

Figure 2.2: *Illustration of the solar energy conversion process from light to electricity: (a) light absorption and exciton creation, (b) exciton diffusion, (c) exciton dissociation, (d) charge transport and (e) charge extraction. The blue and red colors represent the polymer and fullerene in the active layer, respectively. In this thesis, the bottom electrode corresponds to ITO and top electrode to aluminum.*

2.1.2 Absorption

To start the light conversion process, light must be absorbed by the photoactive layer of organic photovoltaics. By receiving the photon energy E from the light (E $\geq$ Eg), an electron is excited from the HOMO level to the LUMO level in the conductive polymer. Simultaneously, an electron-hole pair, namely, a Frenkel exciton is generated in the polymer phase with high binding energy on the order of 0.5 eV. In contrast, the binding energies of Wannier-Mott excitons in inorganic semiconductors are only around 25 meV and can be overcome at room temperature. Due to the significantly higher binding energy of the Frenkel excitons than the thermal energy, additional forces are required to separate the charges. Such forces can be provided by the donor/acceptor interfaces.

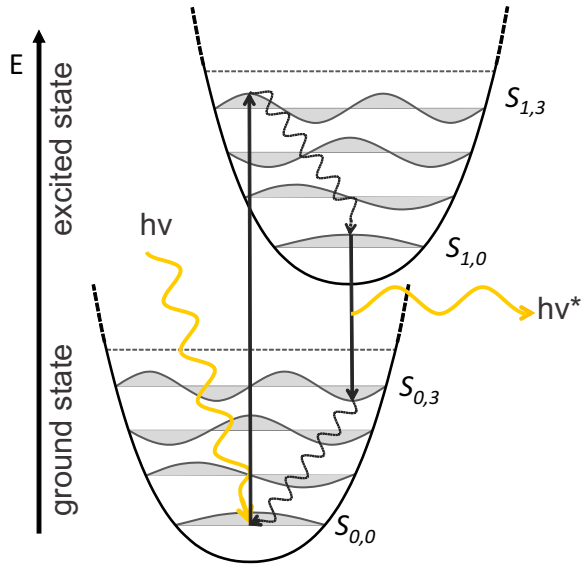

Figure 2.3: *Energy profiles for ground and excited states, including harmonic molecule vibrations according to the Franck-Condon principle. The radiant transition is depicted via straight arrows, and non-radiant transition is indicated as the wavy arrows.*

Moreover, the shape of the absorption spectrum as a function of the wavelength of light is mostly determined by the monomer of the used polymer. For organic molecules, broad bands of absorption due to vibrational excitations are observed, leading to an energetic fine structure. In Figure 2.3, two different electronic states are presented: ground state and excited state. The Franck-Condon principle assumes that electronic transitions are significantly faster than the motion of the nuclei. Accordingly, the electronic transitions are depicted as straight lines perpendicular to the vibrational excitations state illustrated as horizontal lines. Once the photon with energy of hv is absorbed, in an organic molecule the excitation occurs from the vibrational ground state $S_{0,0}$ to the corresponding excited state $S_{1,3}$. After the excitation, the electron transits down to lowest electronic level of the same excited electronic state $S_{1,0}$ via vibrations in the form of non-radiant relaxation, which are indicated by the wavy arrows. The transition probability is determined by the overlapping area of the initial and final state wave functions. The electronic excitation then transits back to the initial electronic ground state but a higher vibronic state $S_{0,3}$ via the emission of a photon. In the end, the electron transits again within the same excited electronic state down to its initial state $S_{0,0}$ by sending out non-radiant energy hv*, i.e. thermal energy. So far, only singlet electron transition is introduced as it is the dominant transition compared to triplet one.

In addition, for conjugated polymers the conjugation length defines the position of absorption spectrum. The conjugation length represents the length of undisturbed $\pi - \pi$

delocalized electron system in a polymer chain, which is smaller than the length of the polymer chain due to the inevitable defects, like kinks. It has been observed that an increased conjugation length arising from an extended π electron system results in a red-shift of the absorption spectrum, which can be realized by increasing the number of the monomers, a proper crystallization route, and so on.

2.1.3 Exciton diffusion

In the case of organic photovoltaics, exciton diffusion contains two main processes to complete the energy transfer, including the trivial energy transfer and Förster transfer (also known as FRET, fluorescence resonance energy transfer). In the case of the trivial energy transfer, which is also referred as photon reabsorption, describes the process that fluorescence emitted by a donor material and reabsorbed by an acceptor material, thus generating a new exciton. The trivial energy transfer mainly occurs if the distance between donor and acceptor molecule R > 10 nm. Thereby it lengthens the apparent lifetime (up to a factor of 2) of the exciton. The relation between the transfer rate $K_{D\to A}^{ET}$ and R is described as follow:

$$K_{D\to A}^{ET} \propto R^{-2} \tag{2.1}$$

The Förster transfer, also known as resonant transfer, is a non-radiant energy transfer from a donor to an acceptor via dipole-dipole coupling.[16] It dominates for short ranged energy transfer with R < 10 nm. The transfer rate for Förster energy transfer is given by:

$$K_{D\to A}^{FRET} = \frac{1}{\tau_D}\left(\frac{R_0}{R}\right)^6 \tag{2.2}$$

In general, the exciton diffusion process including multi energy transfer steps can be understood as a random walk of the exciton via hopping from one polymer site to the next. Due to the random nature of the diffusion, the absolute exciton diffusion distance is smaller than the overall walked distance:

$$l_D = \sqrt{ZD\tau_D} \tag{2.3}$$

An exciton diffusion length of 4-14 nm is proved for conjugated polymers such as P3HT, [17, 18] whereas a relatively larger exciton diffusion length of 14-40 nm is found for the fullerene C_{60}.[19, 20]

2.1.4 Exciton dissociation

Ideally, the excitons arrive at the interface between the donor and acceptor without recombination. The exciton dissociation describes mostly exciton generation in the donor material as electron transfer instead of hole transfer dominates in polymer:fullerene systems. This is due to much more photons are absorbed by the used polymer where absorption typically takes place in the visible light regime. However, exciton dissociation with equivalent charge (hole) transfer is also possible in the acceptor phase.

As soon as an exciton reaches the interface between two electronically matching donor and acceptor materials, exciton dissociation takes place on the time scale of about 10 fs for polymer:fullerene systems. From now on, to differentiate the excitons at the interface with other quasiparticles, especially those excitons under other surroundings, a new term polaron pair is used instead of excitons. Polarons describe quasiparticles, i.e. charges (e^- or h^+) in combination with a distorted environment. Consequently, a polaron exists within a polaron pair (intermediate step from exciton to a pair of free charge carriers) or as subsequent individual polarons. In order to describe the polaron pair dissociation, the Braun-Onsager model is applied, which describes the separation of Coulomb-bonded charges under assistance of an external electric field.[21, 22] Under the electronic field, either the bonded polaron pairs dissociate with a rate K_d, or they recombine with a rate of K_r back to the ground state. Therefore, the dissociation probability can be described by:

$$P(F) = \frac{k_d(F)}{k_d(F) + k_r} \tag{2.4}$$

and the field-dependent dissociation rate is given by:

$$k_d(F) = \frac{3\gamma}{4\pi r_{pp}^3} \exp\left(-\frac{E_b}{kT}\right) \frac{J_1\left(2\sqrt{-2b}\right)}{\sqrt{-2b}} \tag{2.5}$$

where $\gamma = q\mu/\epsilon\epsilon_0$ is the Langevin recombination factor [23] with the elementary charge q, the sum of hole and electron charge carrier mobilities μ and the effective dielectric constant of the organic semiconductor system $\epsilon\epsilon_0$. r_{pp} is the initial polaron-pair radius, $E_b \propto 1/r_{pp}$ the Coulombic binding energy of the polaron pair, kT the thermal energy, J_1 the Bessel function of first order and b the reduced external electric field with $b = q^3F/(8\pi\epsilon\epsilon_0(kT)^2)$. As the polaron-pair separation yield $P(F)$ strongly depends on the charge carrier mobilities μ and the polaron-pair lifetime τ_f, the polaron pair-separation yield $P(F)$ can be alternatively written as:

$$P(F) = \frac{\mu\kappa_d(F)}{\kappa_d(F) + (\mu\tau_f)^{-1}} \tag{2.6}$$

2.1.5 Charge transportation

Followed by the exciton dissociation, the polarons need to be transported through the active layer toward each electrode. The charge transport is closely related to the conductivity of the respective materials as well as the imbalanced hole and electron mobilities. For crystalline semiconductors, charge carriers can transport easily along valence band and conduction band, which is unlikely for organic semiconductors due to their highly disordered system. In the latter, charge carriers are predominantly transported via hopping among the adjacent energy states. Hopping is a thermally activated tunneling process, and the contribution of both thermal activation and tunneling effect are described by the Miller-Abrahams hopping rate:[24]

$$\nu_{ij} = \nu_0 \exp\left(-\gamma' r_{ij}\right) \begin{cases} \exp\left(-\frac{\Delta E_{ij}}{kT}\right) & \Delta E_{ij} > 0 \quad \text{(hopping up)}, \\ 1 & \Delta E_{ij} \leq 0 \quad \text{(hopping down)} \end{cases} \tag{2.7}$$

where ν_0 is the maximum hopping rate, γ' is the inverse localization radius, and r_{ij} is the distance between the site i and j. However, this model can only simulate the mesoscopic hopping transport.

In order to describe the macroscopic charge transport, additional methods such as the Master equations and Monte Carlo simulations need to be included.[25, 26, 27] To describe the charge transport in an organic semiconductor, the Gaussian disorder model is applied.[28] In Figure 2.4, the hopping transport is illustrated. The spatial and energetic disorder existing particularly in organic materials is approximated by a Gaussian distribution of the density of states (DOS) with a width σ. The charge density is defined by $-\sigma^2/kT$, resulting in a defined transport energy as indicated with the horizontal dashed line in Figure 2.4. The free charge carriers are transported in space under an external electric field and relax from an initial higher energy state to a quasi-equilibrium state. Depending on the external energy (e.g. thermal energy K_bT) of a charge carrier, it can hop towards higher energy states or relax towards lower energy states. As for $k_bT > 0$, the charge carriers are transported around the transport energy level with hopping up possible as depicted in Figure 2.4. If $k_bT = 0$, meaning no external energy is available, the charge carriers can only hop towards lower energy states until they get immobile and do not account for charge transport any more.

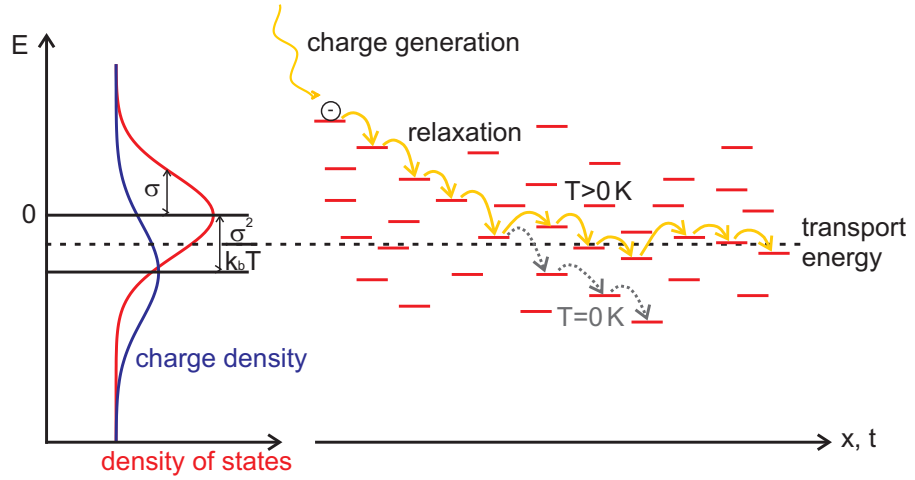

Figure 2.4: *Sketch of the hopping transport process: A Gaussian distribution of the density of states (red curve) and of the charge density (blue curve) are assumed. The free charge carriers transport via hopping in time t and space x under an external electric field. The original presentation can be found in reference [28].*

Moreover, it is worth to mention that the charge carrier mobility in crystalline regions of the polymer is much higher than in the amorphous regions due to the hindrance among different highly disordered polymer chains. Overall, the charge carrier mobility for polymer material with hopping transport mechanism is about $\mu \geq 10^{-2}$ cm^2/V·s, which is several magnitudes lower as compared with metals of $\mu \geq 10^2$ cm^2/V·s where band transport takes place.

2.1.6 Charge extraction

The free charge carriers need to be collected by the corresponding electrodes once they are transported to the interfaces between the active layer and each electrode. The accumulated charge carrier concentration at the interface, the device architecture, as well as the applied electric field (e.g. the direction) strongly influence the charge extraction rate. For instance, interlayers can be applied between the active layer and two respective electrodes to assist the charge extraction process. Interlayers have been proved to have several functions in a polymer solar cell: (1) they can act as an intermediate media to adjust the work function between the electrode materials and the organic materials in the active layer, thus lowering the energy barrier for efficient charge extraction. (2) they can reduce the charge recombination rate at each electrode by forming selective contacts for different types of charge carriers. It is suggested that an electron blocking layer (or a hole

conducting layer) installed next to the bottom ITO electrode and a hole blocking layer (or an electron conducting layer) next to the top metal electrode are beneficial for charge extraction.[29, 30]

So far, a field-dependent charge generation mechanism and drift-diffusion photocurrent without a field-dependent model are commonly used to obtain information on the charge carrier extraction. For the field-dependent charge generation model the charge carrier generation also depends on the electric field, which has been shown by Mihailetchi et al.[31] In combination with the Braun-Onsager model (section 2.1.4) and the Sokel and Huges model,[32] the photocurrent is given by:

$$J_{ph,SH} = J_{ph,max}\left(\frac{\exp(qV/kT)+1}{\exp(qV/kT)-1} - \frac{2kT}{q}\right) \tag{2.8}$$

where $J_{ph,max}$ is the maximum photocurrent, V the internal voltage and kT/q the thermal voltage with the elementary charge q. It is noticed that the photocurrent in equation (2.8) depends on the voltage across the device.

Due to certain limitations of the field-dependent charge generation mechanism, a numerical drift-diffusion model is used to investigate the influence of injection barriers, selective contacts, different recombination mechanisms, and series resistances on the competition between charge extraction and nongeminate recombination of free charge carriers.[33] The current densities for electrons $J_{contact,n}$ and holes $J_{contact,p}$ (including extraction, injection, and recombination) are given by:

$$J_{contact,(n,p)} = qS(n, p - n_0, p_0) \tag{2.9}$$

implying that the contact behavior is determined by the surface recombination velocity S and the charge-carrier equilibrium concentrations n_0 and p_0. As they are related to the electron and hole injection barriers ϕ_n and ϕ_p via Boltzmann approximation (k_bT), the equilibrium concentrations n_0 and p_0 locate at the position x = d (device thickness) are written as:

$$n_0(d) = N_c \exp\left(\frac{-\phi_n}{k_bT}\right) \tag{2.10}$$

$$p_0(d) = N_v \exp\left(\frac{-E_g + \phi_n}{k_bT}\right) \tag{2.11}$$

where N_c, N_v are the effective densities of states (DOS) of LUMO and HOMO, respectively.

This model shows its consistency with published experimental data without the need of a field dependent exciton dissociation mechanism or other additional parameters. It reduces different experimental observations to a single, fundamental mechanism in solar cells with intrinsic absorber layers: position dependent equilibrium concentrations and lifetime of the charge carriers.[33] Other factors such as imbalanced hole and electron mobilities or surface recombinations also affect charge carrier extraction.[28, 34]

2.1.7 Loss mechanisms

So far, we only focus on the light-electricity conversion processes which contribute to the final electricity generation. However, the investigation of loss mechanisms of an organic solar cell is as well crucial. To sum up, different loss mechanisms (i-vi) exist as presented in Figure 2.5, mainly involving charge recombination at different stages and charge carrier trapping.

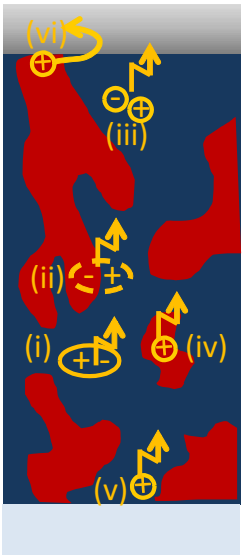

Figure 2.5: *Illustration of the possible loss mechanisms (i) exciton recombination, (ii) germinate recombination, (iii) non-germinate recombination, (iv) a trap assisted recombination, (v) surface recombination occurring in an organic solar cell with an electron acceptor (blue) and donor (red), (vi) charge extraction at wrong electrodes. Recombinations are depicted as yellow arrows.*

As depicted in Figure 2.5, the photon-induced excitons can recombine immediately after their creation (i) or diffuse mostly within the polymer phase. During the diffusion process, they can either recombine if they cannot reach the interface within the exciton

lifetime (typically in the range of ns) or possibly form triplet excitons.[35] Triplet excitons have a total spin S = 1, and they are partially responsible for the reduced photocurrent with the radiative recombination.[36] Such exciton recombination during exciton diffusion are called germinate recombination (ii), which occurs between the positive or negative polarons originating from a common exciton. For those excitons which successfully diffuse to the donor-acceptor interface, exciton dissociation occurs. Consequently, free charge carriers are created and transported through each phase. During the charge transport process, the dominant loss mechanism - nongeminate recombination (iii) of separated free charge carriers from different precursor excitons takes place.[37] Moreover, a trap assisted recombination (iv) could happen when the free charge carriers are tropped or hop into an isolated electron or donor phase. Finally, surface recombination (v) at the contacts or charge extraction at wrong electrodes (vi) can also jeopardize the photovoltaic performance. To avoid the loss of the latter case hole/electron blocking layers as mentioned in section 2.1.6 are used as interlayers to create selective contacts.

In an organic solar cell, before recombination a polaron-pair is formed by Coulomb force between a negative and positive polarons. The recombination process can be described as a two step process with the primary finding of the partners (step I) followed by the actual recombination (step II). Due to the low carrier mobilities in organic materials, the recombination rate is limited by step I. In total, the recombination dynamics depend on the amount of the mobile charge carriers, the electron and hole mobilities, and the dielectric constant of the organic materials.

2.2 Polymer nanomorphology

A polymer and a fullerene derivative are used as the two major components in the photoactive layer. The basics of conducting low bandgap polymers are discussed in section 2.2.1. Followed by the description of polymer crystallization in section 2.2.2, which greatly affects the mobility of the free charge carriers. It is known that the mobility in polymer crystalline regions is several orders of magnitudes higher than that in the amorphous phase.[38] Other general aspects of organic photovoltaics regarding material solubility, miscibility, and the ternary phase diagram of polymer and fullerene blends are introduced in section 2.2.3.

2.2.1 Basics of Low bandgap polymers

Most polymers were widely recognized as insulators before the discovery of conducting polymers, e.g. doped polyacetylene in 1977. Since then, the conducting polymers open up broad applications in many fields. The conductivity is realized by the movement of charge carriers along one polymer chain and from chain to chain, which differs in crystalline and amorphous parts of polymers. In the following, first the band structure of polymers is introduced, followed by the description of the development of low band gap polymers, which is used as one of the main components investigated in this thesis.

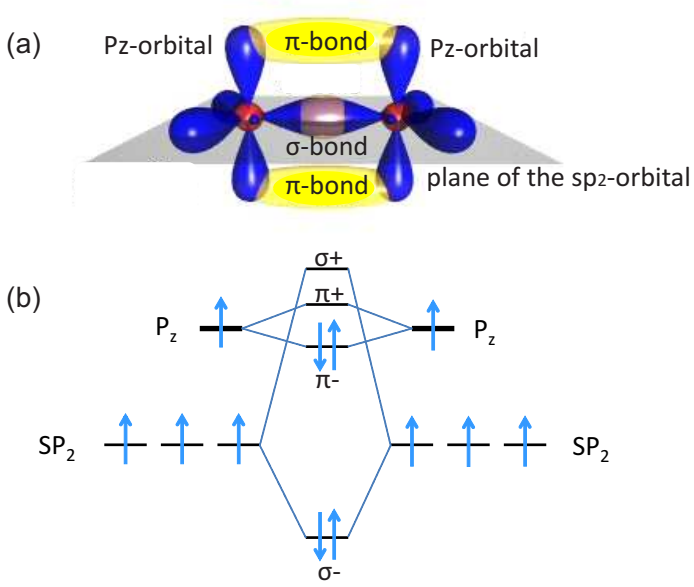

Figure 2.6: *Scheme of (a) the orbitals and (b) the bonds for two sp_2-hybridised carbon atoms.[39]*

Band structure of polymers

The bonding of sp_2-hybridised carbon

Organic Semicoductors are based on the special properties of the carbon atoms. For certain configurations, the so-called sp_2-hybridisation takes place and forms a triangle sp_2-orbitals within a plane, which is perpendicular to the p_z-orbitals plane as shown in Figure 2.6. Due to the axially overlapping sp_2-orbitals of two carbon atoms, a σ-bond is formed between them. The resulting energy difference is quite large between the occupied binding orbitals and the unoccupied anti-binding orbitals. Besides, a π-bond is also formed due to the p_z-orbitals in the sp_2-hybridisations. The energy difference of π-bonds

is much smaller, enabling strong absorption in the visible spectral range. The alternating single and double π-bonds are mainly responsible for the semiconducting properties.

Small-molecule organic semiconductors

For small molecule based on carbon atoms, the π-bonds tend to be delocalized and form a π-system extending over the molecule. With benzene rings as the basic unit (particularly for the polymer PTB7 investigated in this thesis), delocalization implies the electron-pair bonds of six neighboring atoms instead of only two (localized). Due to the π-bonds delocalization (can be found everywhere else), the energy gap between occupied and unoccupied states becomes smaller as shown in Figure 2.7, resulting in the absorption and fluorescence in the visible spectral range. Delocalization of π-bonds is also responsible for the color of many organic molecules. These small molecules can exhibit remarkable transport properties due to the close coupling of the π-system.

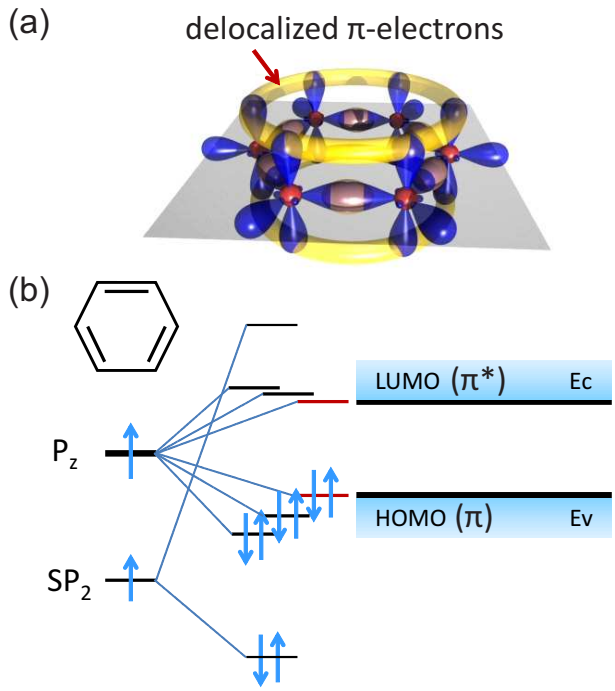

Figure 2.7: *Scheme of (a) a benzene ring and (b) the energy structure of small-molecule organics.[39]*

Polymer organic semiconductors

For the case of long polymer chains with a large amount of bonded carbon atoms, the π-bonds are delocalized along the polymer chain, forming a 1D electronic band with certain band width (on the scale of an eV). Polymer organic semiconductors have a filled valence band and an empty conduction band, which is associated with HOMOs and LUMOs,

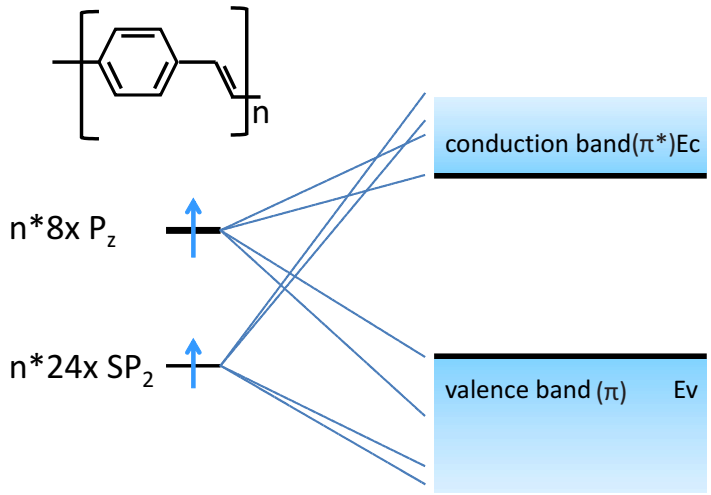

Figure 2.8: *Scheme of energy structure of polymer organics.*

respectively (as shown in Figure 2.8). The energy level difference between the HOMO and the LUMO in a polymer is the corresponding bandgap.

Low bandgap polymers

Low band gap polymers are roughly defined as polymers with a band gap below 2 eV, which can absorb the light with wavelength longer than 620 nm, i.e. red and infrared light. Due to a better overlap of their absorption spectrum with the solar spectrum, low band gap polymers have the possibility to improve OPV device performance, and therefore are strongly needed for a maximum photon harvesting in OPV devices. For instance, well studied P3HT (poly(3-hexylthiophene)) has a band gap of 650 nm (1.9 eV). As a consequence, it has the possibility to harvest up to 22.4% of the available photons, resulting in a maximum theoretical current density of 14.3 mA/cm^2 on the assumption of only singlet excitons exist. In comparison, extending the band gap to 1000 nm will allow for absorption of 53% of the available photons with a maximum current density of 33.9 mA/cm^2 (note that the theoretical current density may increase for a BHJ device due to the contribution of the acceptor).[3]

In order to optimize device performance, besides an increase of current density, a high V_{oc} given by a low band gap polymer is also an effective strategy.[40, 41] It is widely accepted that V_{oc} is determined by the difference of the HOMO of the polymer and the LUMO of the fullerene. Thus, an optimum alignment of the energy levels in OPV is of utmost significance. In Figure 2.9, a schematic illustration of the energy levels in a polymer BHJ solar cell is shown.

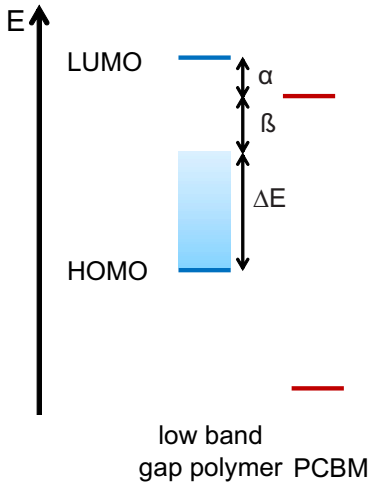

Figure 2.9: *Alignment of energy levels in bulk heterojunctions with a low band gap polymer (LBG) and PCBM. HOMO and LUMO are represented with blue lines. The acceptable range of energies for the HOMO level of the donor is shown as a shading. α represents the energy difference between the LUMO of the polymer and the LUMO of PCBM. β represents the minimum acceptable value for V_{oc}. When knowing the band gap of the polymer and the acceptable levels of a and b it is possible to estimate the energy range that is acceptable for the HOMO level of the donor according to $\Delta E = E_g$-α-β.[3]*

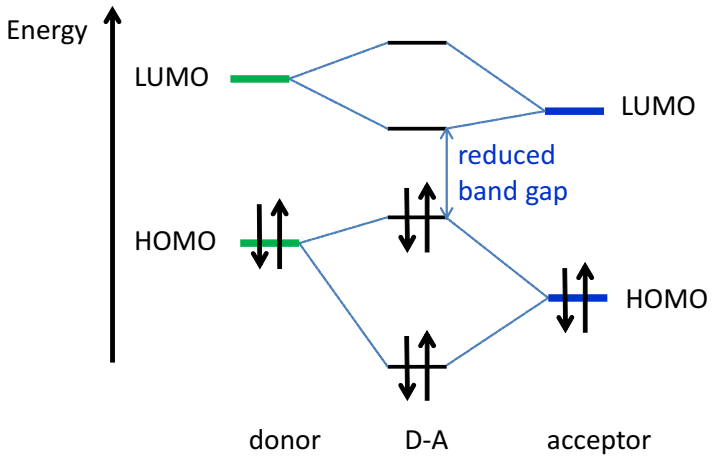

Figure 2.10: *An example of controlling the molecular orbital energy levels through the hybridisation of donor-acceptor intramolecular interactions.[42]*

To obtain an efficient low band gap polymer, several factors that influence the band gap of a conjugated polymer need to be considered: (1) intra-chain transfer (2) bond-length alternation (3) aromaticity (4) substituents effects (5) intermolecular interactions (6) conjugation length.[3] By following these design considerations, and especially by use

of alternating donor-acceptor units (shown in Figure 2.10), the most efficient low band gap polymer published so far PTB7 was synthesized,[13] which is used as a major component in this thesis. The HOMO level of the donor and the LUMO level of the acceptor are close in energy, resulting in a reduced low band gap polymer with using electron withdrawing groups (fluorine atom for the case of PTB7) on the acceptor part and electron donating groups on the donor part.

2.2.2 Molecular order and crystallinity

Polymers are long molecular chains comprising repeating chemical units, which form irregular, entangled coils in the melt. Some of them are able to crystallize upon cooling from the melt, mechanical stretching or solvent evaporation. Crystallization affects optical, mechanical, thermal, and electrical properties of the polymer. However, the entanglements result in high entropic activation barrier, which hinders a full crystallization of polymers, thus crystallized polymers mostly exist in a semicrystalline state instead of large single crystals. Additonally, polydispersity is also responsible for partly crystallized polymers. The properties of semicrystalline polymers are determined by the degree of crystallinity, and the size and orientation of the molecular chains. The crystallinity has profound impact on the charge transport properties of conducting polymers. As an example, the charge carrier mobility and consequently conductivity in the crystalline region is orders of magnitudes higher than that of the amorphous region.[38] The crystallization process of a polymer can be described with a multistage model proposed by Strobl,[43, 44] which is widely accepted but still under debate.

Nucleation

Defects like chain ends, entangled chains, and impurities are located only in the amorphous region. With the assistance of the thermal fluctuations, crystallite embryos form at these spots if they grow fast enough. Polymer crystallization starts with embryos, and followed by the formation of nuclei. The nucleation rate τ_{nuc}^{-1} yields an exponential function of the temperature.[45]

$$\tau_{nuc}^{-1} \propto \exp\left(-\frac{\Delta U + \Delta F_c}{k_b T}\right) \tag{2.12}$$

where ΔU represents an activation energy barrier for diffusion across the phase boundary, which is dominant due to the low mobility of the polymer at low temperatures. At high temperatures the critical free energy barrier for primary nucleation, ΔF_c, takes over due to the formation of nuclei, resulting in a gain in free energy.[46] k_b is the Boltzmann constant and T is the temperature. As a result, a maximum nucleation rate is found at intermediate temperatures which change with chain length.[47]

Experimentally, the nucleation rate is proportional to the volume v of the crystallized domain:[48]

$$\tau_{nuc}^{-1} \propto v \tag{2.13}$$

Growth kinetics

After the formation of the nuclei, polymer crystals start to grow. The growth of polymer crystals is always perpendicular to the chain direction with a lateral expansion up to micrometers. Branching, splaying, and symmetry growth give rise to so-called spherulite structures, as indicated in Figure 2.11(d). However, these relatively large polymer crystals are not desirable for organic photovoltaics due to the short exciton diffusion length (about 10 nm). Therefore, only the early stages of polymer crystal formation which are commonly observed in organic photovoltaics are detailed in this section.

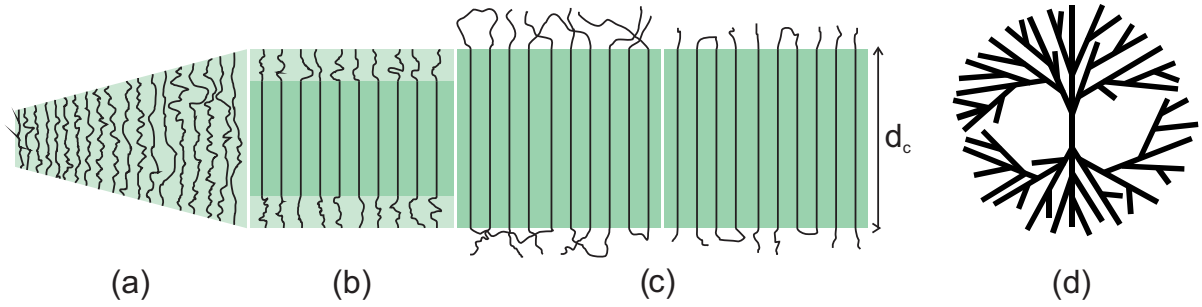

Figure 2.11: *The crystallization process in the multistage model is devided into three steps (a) growing of a mesomorphic layer, (b) solidification by core crystallization, and (c) stabilization by surface ordering by Strobl.[43] (d) A spherulite structure is formed in the case of branching and splaying.*

Polymer crystallization is not the reverse process of melting of polymers or vice versa. It has been demonstrated that polymer crystallization and melting of polymers in bulk can be described by different laws using three characteristic temperatures: T_{am}^{∞}, T_{ac}^{∞}, and T_{mc}^{∞}. T_{am}^{∞} describes the transition from the amorphous (melt) to the mesomorphic phase (an intermediate state between liquid and crystal), T_{ac}^{∞} is the transition from the amorphous to the crystalline phase (equilibrium melting point) and T_{mc}^{∞} represents a virtual transition between the mesomorphic and the crystalline phase whereas

$$T_{am}^{\infty} < T_{ac}^{\infty} < T_{mc}^{\infty}. \tag{2.14}$$

In Figure 2.11, the crystallization process described by a multistage model is presented. A thin mesomorphic layer (b) stabilized by epitaxial forces grows out of the melting phase (a). The core region solidifies when a critical thickness is reached and a crystal block (c) is formed. The crystal thickness d_c is determined by the crystallization temperature. Consequently, the polymer crystals stabilize after the chains at the surface of the block get ordered.[44] Due to high inner chain mobility, defects can be excluded from the mesophase while a thicker mesomorphic layer is formed spontaneously.

According to this multistage model, a thermodynamic phase diagram is constructed by Strobl as shown in Figure 2.12.[49] In this phase diagram, different stable phases and the transition line between the adjacent phases are plotted as a function of the inverse crystal thickness $1/d_c$ and temperature T. The Gibbs-Thomson equation is used to describe the effect of surface free energy and transition temperatures. The generalized equation can be applied to different equilibrium stage:

$$T_x n = T_x^{\infty}(1 - \frac{2\sigma_x}{n\Delta h_x}) \propto \frac{1}{d_c} \tag{2.15}$$

where x is the coexistence for all lines, i.e., x could be *ac*, representing for the theoretical melting lines, *mc* for crystallization and recrystallization lines, or *am* for the transition from the melt to the mesophase. σ_x is the surface free energy and Δh_x the heat of fusion.

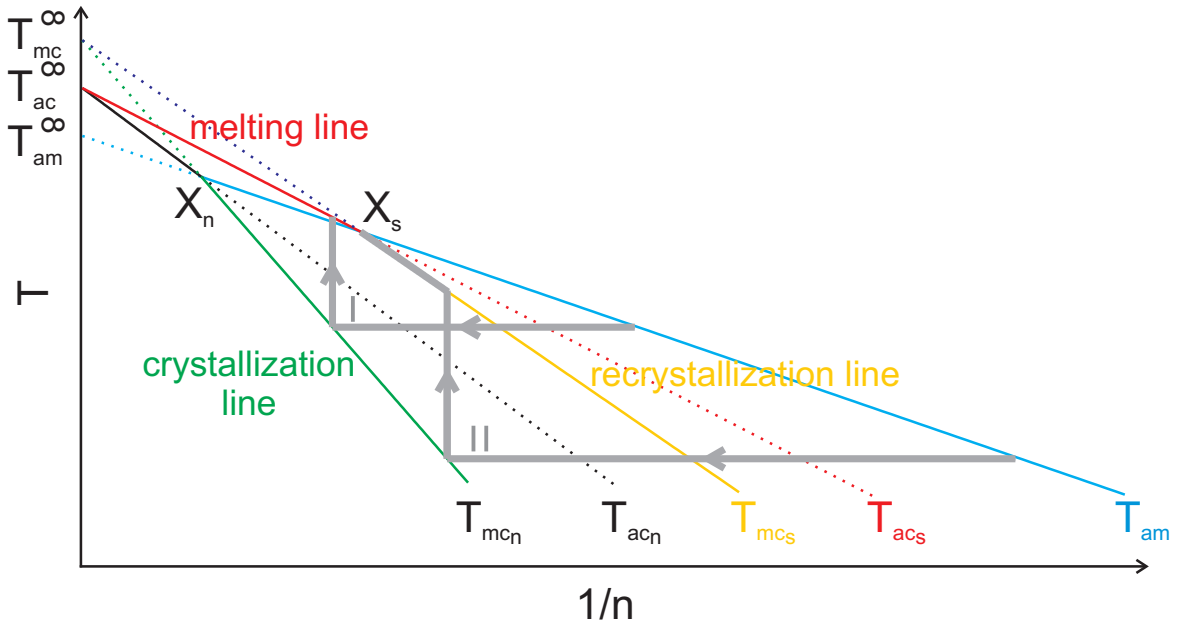

Figure 2.12: *T/n^{-1} phase diagram of layered polymer crystals in an amorphous melt after Strobl's work.[43] Four phases are separated by the transition lines, namely (a) melt, (m) mesophase, (c_n) native crystals and (c_s) stabilized crystals are described by equations (2.15).*

Growth rate

The crystallization temperature sets the crystal thickness d_c, while the lateral dimension of the crystallite lamellae, containing several crystalline blocks merged together during growth, is proportional to the crystal thickness d_c but not limited. The growth rate of the crystalline v is given by Vogel-Fulcher law:

$$v = v_0 \exp\left(-\frac{T_A^*}{T}\right) \exp\left(-\frac{T_G}{T_{zg} - T}\right). \tag{2.16}$$

where T_A^* is the effective activation temperature, T_G is the glass transition temperature, and T_{zg} is the zero-growth temperature (a characteristic temperature for a given polymer). Therefore, the growth rate of the crystallite is highly temperature dependent. At low temperatures, the growth rate is dominated by the first exponential due to the decisive segmental mobility of the melt, and it follows an Arrhenius law. At high temperatures, an activation barrier expressed as the second exponential dominates. As the crystal surface can be destabilized and additional segmental mobility is introduced at higher temperatures, the growth rate is observed to reach a global maximum.

Secondary crystallization

At the end of a primary isothermal crystallization process, further changes in polymer structure associated with a density increase occur. This density increase is called secondary crystallization. Secondary crystallization is realized by lamellar insertion in the amorphous areas and results in a spatial homogenization of the crystallinity at a given temperature. The inserted lamella thickness is decreasing with decreasing temperature.[44] The extent of secondary crystallization is affected by the perfection of crystalline structure produced during primary crystallization.[50]

2.2.3 Other aspects

An optimized BHJ nanomorphology is recognized as an important key to achieve higher efficiency for organic photovoltaics.[51] The BHJ film morphology strongly depends on thermodynamic and kinetic aspects during the film formation process. The kinetics of the system is mainly influenced by the solvent properties such as the solvent vapor pressure (speed of evaporation) and solubility properties, whereas the thermodynamics is primarily determined by the intrinsic properties of the used materials such as their miscibility.

Vapor pressure

The arrangement of the materials from the liquid to the solid states can be influenced by the drying kinetics. For the well-investigated P3HT:PCBM system, it was often observed

that solvents with lower vapor pressure give rise to higher device performance.[52, 53] During solvent evaporation, the drying kinetics competes with the thermodynamics of the film. Solvents with lower vapor pressure allow polymer chains to self-assemble within a longer time frame. In the case of highly volatile solvents (high vapor pressure), the speed of evaporation is faster than that of the crystallization. However, there is not much fundamental thermodynamic and kinetic knowledge about the effect of solvent vapor pressure on the morphology formation.[54]

Solubility

Since solubIlity is one of the decisive parameters for processing the active layer and therefore obtaining better device performance, different approaches have been used to determine the solubility of a material. The mostly used method is the Hansen solubility theory using Hansen solubility parameters (HSPs), which describes the interactions between a solvent and a solute. Three components are considered for HSPs: dispersion interactions σ_D, permanent dipolar-permanent dipolar molecular interactions σ_P, and hydrogen bonding interactions σ_H. The solubility "distance" R_A between the HSPs of the solvent and the HSPs of the solute is calculated using the equation as below:

$$R_A{}^2 = a\left(\sigma_{D2} - \sigma_{D1}\right)^2 + b\left(\sigma_{P2} - \sigma_{P1}\right)^2 + c\left(\sigma_{H2} - \sigma_{H1}\right)^2 \tag{2.17}$$

where R_A is the solubility "distance" parameters, σ_{D2} is the dispersive component for the solvent, σ_{D1} is the dispersive component of the solute, and a, b, c are the weighting factors. Hansen sets a = 4 and b = c = 1 based on empirical testing. In order to differentiate between "sufficient" and "nonsufficient" interactions from a solubility standpoint, a boundary of solute's solubility is needed. As a consequence, in the Hansen solubility space of a solute is treated as a sphere with the HSPs as the coordinates of the center of the sphere, and R_0 is introduced as the radius of the sphere representing the boundary of solubility. By comparing R_A and R_0, the relative energy difference (RED) is obtained using the equation:

$$RED = \mathrm{R}_A/\mathrm{R}_0 \tag{2.18}$$

where a good solvent is expected with Red between 0 and 1, and a poor solvent when RED is higher than 1.[54] Such prediction theory of solubility has been proved to be a very powerful tool to reduce the expensive and time-consuming experimental efforts.[55]

Miscibility

Besides the solubility of each component of the active layer, the miscibility between polymer and fullerene is another determining factor for organic photovoltaics applications. From a thermodynamic point of view, the change in free energy due to mixing, "Gibbs free energy" is usually used to describe the miscibility. Depending on Gibb's free energy, blends of two components can either form a homogeneous mixture as one phase or phase separation as multiphase systems. Since the Gibbs free energy cannot be determined directly, Flory and Huggins came up with a mean-field theory to study the thermodynamics of polymer solutions and polymer blends. The free energy ΔG_m can be expressed by the sum of the change of entropy ΔS_m and the change of enthalpy ΔE_m due to mixing of A and B.

$$\Delta G_m = -T\Delta S_m + \Delta E_m \tag{2.19}$$

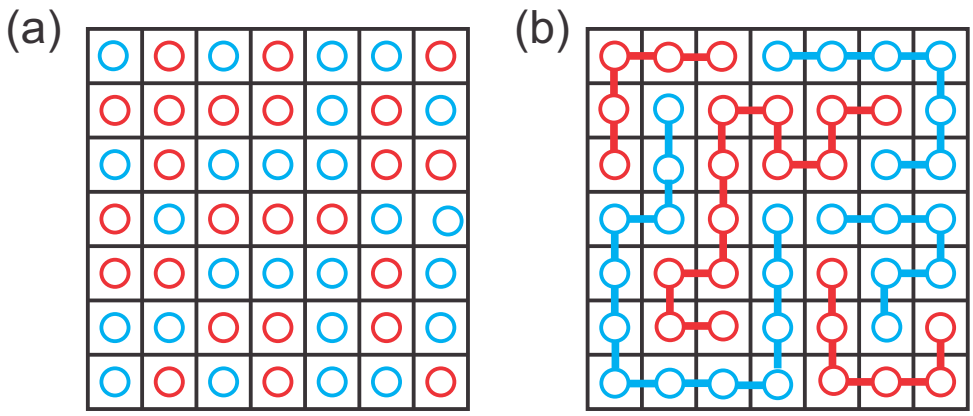

Figure 2.13: *Lattice model of a mixture of (a) two low molecular components and (b) two polymers.*

To estimate the change in the entropic part, a lattice model where all sites are fully occupied with no repeating entry of each lattice site is applied (Figure 2.13). Consequently, the change of entropy ΔS_m due to mixing is derived from $S = k_B \ln(\Omega)$ with Ω as the number of possible configurations and k_B the Boltzmann constant .

$$\Delta S_m = S_{AB} - (S_A + S_B) = -k_B n \left[\frac{\phi_A}{N_A} \ln \phi_A + \frac{\phi_B}{N_B} \ln \phi_B \right] \tag{2.20}$$

where N_i is the degree of polymerization, ϕ_i is the volume ratio of component $i \in$ [A,B], and n is the total number of molecules on the lattice. The entropy increases after mixing as the combinatorial possibility of the mixture is higher than a pure component. The entropy increase of polymer-polymer mixtures is lower than the increase of mixing two low molecular weight components due to the significant lower number of possible configurations as seen in Figure 2.13.

Together with the enthalpic contribution to the Gibbs free energy (accounts for the interaction between the monomers of two components), the resulting Flory-Huggins theory is obtained as:

$$\Delta G_{mix} = RT \left[\frac{\phi_A}{N_A} \ln \phi_A + \frac{\phi_B}{N_B} \ln \phi_B + \chi \phi_A \phi_B \right] \tag{2.21}$$

where $R = k_B N$ is the gas constant, N is Avogadros number, and χ is the Flory-Huggins interaction parameter. It should be noticed that in the mean-field formalism of the Flory-Huggins model, an incompressible system is assumed, and thus χ is independent of pressure, composition, molecular weight, and chain architecture. However, experimental results suggest further correction of χ is needed due to an additional entropic contribution χ_S. As a result, the empirical Flory-Huggins interaction parameter χ can be expressed as:

$$\chi = \chi_S + \chi_H / T \tag{2.22}$$

with the enthalpic contribution χ_H.

Ternary phase diagram of polymer, fullerene, and solvent

Taking all the above mentioned factors into account, it is concluded that there is a subtle interplay between many parameters in the ternary system of polymer, fullerene and solvent. In order to optimize the film morphology, the combinatorial impact of several parameters need to be considered at the same time: the chemical compatibility between polymer and fullerene, the miscibility and solubility of both in the solvent and appropriate drying behavior at solvent extraction during the film formation process.

To illustrate the relationship of all related parameters, the ternary phase diagram of polymer, solvent and fullerene at a constant temperature T and a constant pressure p is suggested by Hoppe et al. as shown in Fig 2.14.[56] In a solution (located at the top of the triangle phase diagram), the amount of polymer and fullerene are relatively much less than

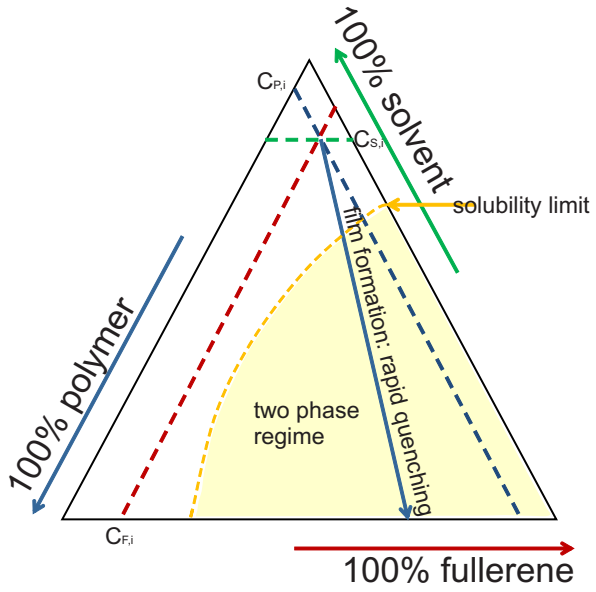

Figure 2.14: *Schematic ternary phase diagram of a polymer-fullerene-solvent system at constant temperature T and constant pressure p. $C_{P,i}$, $C_{F,i}$, and $C_{S,i}$ are the initial concentrations of polymer, fullerene, and solvent in the solution, which increase according to the arrow direction. During film formation a transition from the blend solution towards a solid-state blend takes place. Upon extraction of the solvent, film morphology is eventually determined by the combinational effects of solvent volatility, solubility and miscibility of both components. The original graph can be found in reference [56].*

that of the solid film state. The solvent then can be regarded as a compatibilizer where the mixing of the two components occurs. During the film drying process (transition from solution state to solid film state), the amount of solvent is decreasing, resulting in more repulsive interactions between polymer and fullerene. Subsequently, temperature dependent phase separation or spinodal decomposition will take place. In the case of highly volatile solvent (high vapor pressure), i.e. chloroform, a mixed state of polymer-fullerene blend are formed (the two phase regime in the ternary phase diagram), and the system is quenched into a metastable state which phase separation cannot proceed at lower temperatures due to their low mobility. Reactivation of phase separation can be realized with the assistance of external treatment such as thermal annealing or solvent vapor annealing. As a result, the molecule mobility increases, thus both polymer and fullerene start to diffuse or crystallize, depending on the conditions. In contrast, for the solvent with low vapor pressure, the polymer and fullerene molecules are mobile for a longer time during the drying process. Therefore, phase separation of both materials can immediately take place, forming larger coarsened domain structures.

Besides the volatility of the solvent, the solubility of both components also plays a significant role upon film formation. Within the limited film drying time, fullerene molecules tend to precipitate into pure large fullerene domains. The onset for fullerene precipitation is when the ternary system steps into the two phase regime (corresponding to the yellow region in Figure 2.14) where the solubility limit of the fullerene is reached upon solvent evaporation. For the PTB7:PCBM system investigated in this thesis, additional solvent additive with different volatility and solubility is used for some samples. Due to the complexity of the case of additional solvent additive, it is not included in this ternary phase diagram but discussed in details in chapter 6.

2.3 Scattering techniques

As explained in section 2.1, the nanomorphology of the active layer directly affects the final PCE of the polymer solar cell. In order to probe the film morphology, namely, the nanomorphology formed by phase separation and crystallization described in section 2.2, X-ray and neutron scattering techniques are applied in this thesis as they can offer statistical information of a large volume of the investigated films compared with the traditional real space imaging techniques. First, the basic scattering principles for X-ray are discussed in section 2.3.1, which can also be applied for neutrons. The physical background of X-ray reflectivity measurement is detailed in section 2.3.2; Followed by the introduction of GISAXS and GISANS measurement in the time-of-flight mode in section 2.3.3, which are the main techniques applied in this thesis for probing the structure formed by phase separation; In the end, GIWAXS measurement as widely used to probe crystalline structures of the active layers is explained in 2.3.4.

2.3.1 General principles

The physical definition of scattering is that an electromagnetic wave or a particle deflects at an object or in matter with a different refractive index.[57] In the following part, the scattering basics generally applied both for X-rays and neutrons are introduced. The positon dependent electric field vector $\vec{E}(\vec{r})$ of an electromagnetic wave traveling through a medium with the position dependent refractive index $n(\vec{r})$ is described by the Helmholtz equation:[57]

$$\Delta\vec{E}(\vec{r}) + k^2 n^2(\vec{r})\vec{E}(\vec{r}) = 0 \tag{2.23}$$

depending on the the modulus k of the wave vector $\vec{E}$ of the electromagnetic wave and the position $\vec{r}$, the refractive index can be expressed as:

$$n(\vec{r}) = 1 - \delta(\vec{r}) + \mathrm{i}\beta(\vec{r}) \tag{2.24}$$

in relevance with the dispersive part δ and the absorbing part β. In this thesis, the refractive index n of a material is assumed to be positon independent, thus the dispersion and absorption of a material are simplified as δ and β. For a homogeneous medium far away from absorption edges, δ and β are dependent on the wavelength of the beam, and can be expressed as:

$$\delta = \frac{\lambda^2}{2\pi}\rho_e, \tag{2.25}$$

$$\beta = \frac{\lambda}{4\pi}\mu, \tag{2.26}$$

where ρ represents the scattering length density (SLD) and μ is the absorption coefficient. The SLD of investigated materials interacting with X-rays is determined by the classical electron radius $r_e = 2.814 \cdot 10^{-5}$ Å and the electron density of the investigated material ρ_e, which is written as $\rho = r_e\rho_e$. In comparison, the SLD of neutron experiments is affected by the number density of atoms N and the coherent scattering amplitude of a bound atom b, and thus described as $\rho = Nb$. Typically, for hard X-rays dispersion δ is in the order of 10^{-6} and absorption β in the order of 10^{-8}, whereas for neutrons, dispersion $\delta = \mathcal{O}(10^{-6})$ and $\beta = \mathcal{O}(10^{-12})$.[57] Consequently, the absorption plays a minor role for neutrons and is mostly negligible.[58] Scattering experiments with X-rays or neutrons strongly depend on the difference in scattering length densities, i.e. for X-rays the difference in electron density of the investigated materials, which is also referred as scattering contrast.

In Figure 2.15 a standard scattering setup including specular scattering and diffuse scattering is presented. The coordinate system is defined by the sample plane and the plane of the incident beam $\vec{k_i}$ and exiting beam $\vec{k_f}$. As a result, the scattering plane is expanded to 3-dimensional coordinates with the x, y and z axes. The incident beam $\vec{k_i}$ impinges on the sample surface with an incident angle α_i. It can reflect or transmit in a specular geometry in the xz plane, or diffuse in the xy plane. The specular beam and the diffuse scattered beam $\vec{k_f}$ exit with the angle α_f, and the transmitted beam as $\vec{k_t}$ with refracted angle α_t. α_t can be calculated via Snell's law of refraction, which can be found everywhere else. For the case of diffuse scattering in the xy plane the exit out-of-plane angle ψ_f and the exit angle α_f are additionally included. The momentum transfer (used to analyze the interaction), also named as scattering vector $\vec{q}$ is defined by

$$\vec{q} = \vec{k_f} - \vec{k_i}. \tag{2.27}$$

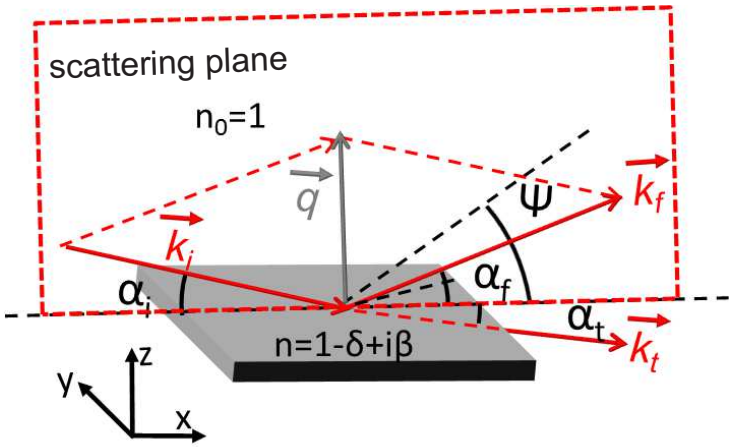

Figure 2.15: *Scattering setup is depicted in reflection geometry with incident beam $\vec{k_i}$ and and exiting beam $\vec{k_f}$. The incident angle α_i and exit angle α_f originating from specular scattering as well as the refracted angle α_t lie in the xy scattering plane, the out-of-plane angle ψ_f arising from diffuse scattering exists in the xz scattering plane.*

In this thesis, only elastic scattering is considered for both X-rays and neutrons, i.e. the wavelength, and therefore the energy of the beam is conserved during the scattering event. Therefore, the scattering vector only describes a change of direction whereas its modulus remains the same. For a beam with wavelength λ, the modulus of the wave vector is $k = 2\pi/\lambda$. Since $\delta > 0$, the refractive index $n < 1$, meaning that X-rays or neutrons enter from the air with higher refractive index than the investigated film. As a result, a total reflection occurs in a small angle approximation when the incident angle α_i is smaller than the critical angle α_c, which is given by

$$\alpha_c = \alpha_i \approx \sqrt{2\delta} = \lambda\sqrt{\frac{\rho}{\pi}}. \tag{2.28}$$

For this case, the intensity at penetration depth Λ is reduced to 1/e of its original intensity ($\approx$ 37%). However, a so-called escape depth has to be considered due to the second damping on the way from the scattering event to the film surface. Therefore, the scattering depth Λ can be estimated to be approximately half of the penetration depth for most materials (in the order of 50 Å).[59, 60] However, for the case of $\alpha_i > \alpha_c$, the penetration depth is commonly observed in the order of hundreds of nanometers, which is only limited by absorption.

2.3.2 X-ray reflectivity

For X-ray reflectivity (XRR) measurements, only the specular scattering as a function of the incident angle α_i is recorded, i.e. $\alpha_i = \alpha_f$ and the out-of plane angle $\psi_f = 0$. Consequently, the scattering vector $\vec{q}$ is normal to the sample plane and therefore only the q_z component is different from 0.[57]

$$\vec{q_z} = \vec{k_f} - \vec{k_i} = \frac{4\pi}{\lambda}\sin(\alpha_i) \tag{2.29}$$

As a result, the electron density distribution in the vertical direction is detected. To analyze the reflectivity curves, the simple assumption of one interface is not sufficient for the reason that typically the polymer films investigated in this thesis often contain a certain inner layering. Therefore, a model with N layers whereas the refractive index $n_j(z)$, the thickness as well as the roughness of each layer i are used to simulate the reflectivity data. For most cases, air and the sample substrate (i.e. silicon) are used as the confining layers with infinite layer thickness. In addition to the absorption, at each single interface between two layers with different refractive index the incident beam is partially reflected and partially transmitted. The reflectivity and transmission are defined by $R^F = |r^F|^2$ and $T^F = |t^F|^2$,[57] and the ratio of the amplitudes of the reflected and transmitted beam is given by the Fresnel reflection coefficient r^F and the Fresnel transmission coefficient t^F, respectively. For the interface between layer j and j+1 the ratio of reflectivity and transmission $X_j = R_j/T_j$ is calculated under the condition of $R_{N+1} = 0$ (representing zero reflection at the interface N+1). As a consequence, R_1 can be obtained as the final reflectivity using a matrix formalism by Abelès.[61]

However, an equivalent but numerically more efficient model developed by Parratt is more widely used.[62] The finally reflected intensity at the top layer is calculated iteratively by a recursive algorithm. Up to now, the formalism assumes perfectly smooth interfaces and thus interfacial roughness are considered as zero. In reality, however, the interfaces show certain roughness leading to a change of the refractive indices. The roughness of an interface σ_{rms} is commonly described by the root mean square roughness ρ:

$$\sigma_{rms} = \sqrt{\frac{1}{N_{\sigma_{rms}}}\sum_{i=1}^{N_{\sigma_{rms}}}\Delta z_i^2} \tag{2.30}$$

Where $N_{\sigma_{rms}}$ is the number of sampling points along the interface and Δz_i is the deviation from the mean interface at the sampling point i. The roughness can be included in the Parratt algorithm using an exponential function called N-C factor based on the assumption of a Gaussian distribution of the height at the surface. It is realized by correcting the

Fresnel reflection coefficients by an additional factor. This correction reaches its limit when the roughness is also in the range of the layer thickness. However, this problem can be solved by dividing the corresponding layer into multiple sub-layers, which is called slicing procedure.[63] More details regarding the theoretical background of XRR can be found elsewhere.[57]

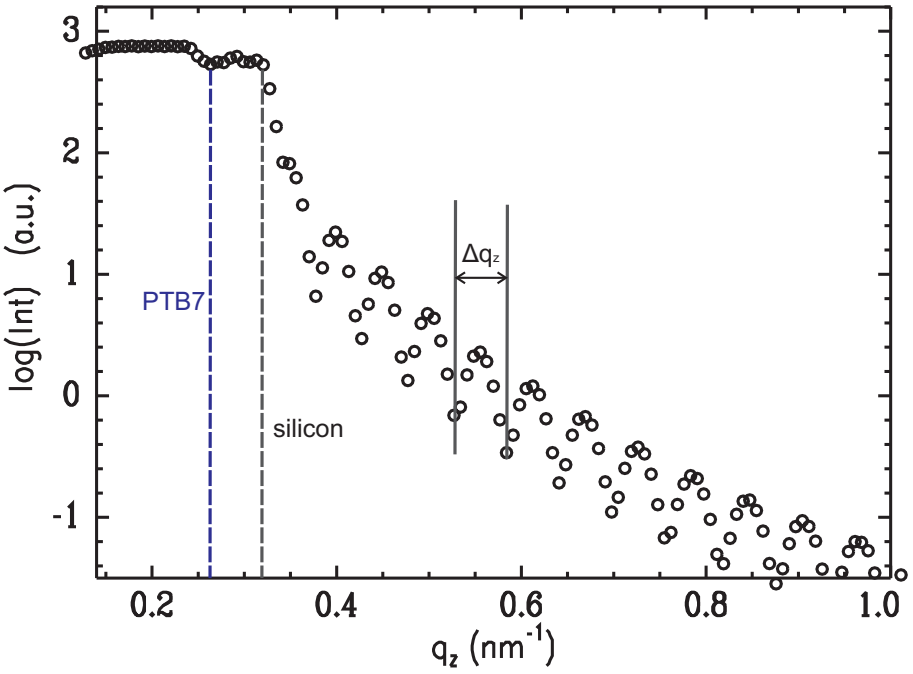

Figure 2.16: *Measured reflectivity data of a PTB7:$PC_{70}BM$ film spin-coated of solvent mixture trichlorobenzene:DIO on a silicon substrate. The critical q_z values of PTB7 and silicon are highlighted. The distance between the minima of the Kissing fringes is Δq_z.*

As an example, the measured XRR data of a PTB7:$PC_{70}BM$ film on a silicon substrate is presented in Figure 2.16. At low incident angles ($\alpha_i < \alpha_c$), the normalized intensity is 1 due to total reflection. For $\alpha_i = \alpha_c$, an intensity minimum in the reflectivity and a strong intensity decay with q^{-4} for $\alpha_i > \alpha_c$(Si) are observed. For a thin film on a substrate, in addition to the Fresnel reflectivity function, so-called Kiessig-fringes are observed due to interference effects.[64] The amplitude of the fringes decreases with increasing interfacial roughness σ_{rms}. The distance between two interference maxima Δq_z is directly determined by the layer thickness d via $d \approx 2\pi/\Delta q_z$.[64]. Information including layer thickness, interfacial layer roughness, and especially the scattering length density profile is extracted when the experimental data is fitted using the recursive algorithm model introduced by Parratt.[62, 65]

2.3.3 Grazing incidence small angle scattering

Besides the specular reflection measured in XRR, the interfacial roughness included in the last section can cause diffuse scattering in the sample plane (xy plane). Moreover, for the case of polymer films, statistically regular lateral structures also give rise to diffuse scattering, which is beyond the contribution of the simple interfacial roughness. In this thesis, the diffuse scattering is measured in grazing incidence geometry with a fixed incident angle $\alpha_i < 1^\circ$ so that a large scattering volume can be measured. For a given sample-detector distance (SDD), the scattered intensity is recorded with a two-dimensional detector whereas each pixel corresponds to certain out-of-plane angle Ψ_f and certain exit angle α_f. The scattering vector is $\vec{q}$ is:

$$\vec{q} = (q_x, q_y, q_z) = \vec{k_f} - \vec{k_i} \tag{2.31}$$

With each component:

$$\begin{aligned} q_x &= \frac{2\pi}{\lambda} \left(\cos\alpha_f \cos\Psi - \cos\alpha_i\right) \\ q_y &= \frac{2\pi}{\lambda} \cos\alpha_f \sin\Psi \\ q_z &= \frac{2\pi}{\lambda} \left(\sin\alpha_f + \sin\alpha_i\right) \end{aligned} \tag{2.32}$$

whereas the q_x component is negligible as the angles are generally very small in the grazing incidence geometry. The q_y component is mainly attributed to the lateral structures, and the vertical structures parallel to the film yield diffuse scattering in q_z direction. A special intensity oscillation along the q_z direction due to correlated roughness is observed for some thin films.[66, 67] Correlated roughness occurs when certain length scales are replicated from the film underneath, and more details can be found in chapter 6.1.

To analyze the GISAXS data, the distorted wave Born approximation (DWBA) is commonly used as the ideal framework, where the scattering process is treated as a perturbation of an ideal system with flat interfaces.[68, 69] Consequently, first-order perturbation theory is applied, in which the roughness and lateral structures are included as the disturbance. Depending on the value of the scattering vector $\vec{q}$ and the roughness σ_{rms} of the sample surface, as well as the intensity distribution in the region of total external reflection, the differential cross section is described by:

$$\left|\frac{d\sigma}{d\Omega}\right|_{diff} = \frac{C\pi^2}{\lambda^4} \left(1 - n^2\right)^2 |T_i|^2 |T_f|^2 P(\vec{q}) \propto P(\vec{q}) \tag{2.33}$$

in which C is the illuminated surface area, λ is the applied wavelength, n is the refractive index, T_i, T_f are the Fresnel transmission functions determined by the incident and exit angle, and $\mathrm{P}(\vec{q})$ is the probed diffuse scattering factor. When the the incident angle is equal to the critical angle of the investigated material, the transmission function has its maximum value observed as Yoneda peak.[70] The out-of-plane cut is therefore performed at this position in order to achieve the highest material sensitivity.
In total, the diffuse scattering factor can be expressed as follows for N identical and centro-symmetrical objects with a random orientation:

$$P\left(\vec{q}\right) \propto NF\left(\vec{q}\right) S\left(\vec{q}\right) \tag{2.34}$$

where $\mathrm{P}(\vec{q})$ depends on the form factor of the individual objects, $\mathrm{F}(\vec{q})$, and the structure factor $\mathrm{S}(\vec{q})$. The form factor $\mathrm{F}(\vec{q})$ is the Fourier transform of the particle shape.[71] Note that in this thesis only scattering factors in q_y direction are particularly assumed with such a model. Accordingly just the information of lateral structures such as the object size and the structure distance is extracted, which is commonly referred as the effective surface approximation.[72]

To analyze the scattering data, the q_y relevant horizontal line cuts at a specific Yoneda peak need to be fitted with a one-dimensional paracrystal model within the frame of the DWBA as mentioned above. Actually the DWBA includes four terms as a product of both scattering and reflection: simple scattering (i), reflection on the substrate followed by scattering (ii), scattering followed by reflection (iii) and first reflection followed by scattering with another reflection on the substrate (iv). The four terms in the DWBA are included through a final corrected form factor by the sum of all contributions.

The 1D paracrystal model further includes more influential contributions such as the object shape and the object size distribution, and additionally defines the spatial arrangement of the objects by the structure factor $\mathrm{S}(\vec{q})$. To simulate the scattering, cylinders or spheres are used as they can provide the typical orientation insensitive isotropy of the investigated polymer films. In a paracrystalline lattice, the objects exhibit only a short-range order due to the deviation of the theoretical object position is increasing with increasing distance from the origin of this lattice. As for the object size distribution, a typical local monodisperse approximation (LMA) is used. It is assumed in LMA that local domains have the size of the coherence length of the beam, meaning that each object only scatter with those with the same size, thus objects with different sizes are independent of each other. The effective interface approximation assumes that the scattering occurs at only one surface, allowing the decoupling of the height and the radii of the scattering objects.[73] As a result, a one-dimensional paracrystal model containing maximum three form factors (cylinder or sphere) and three corresponding structure factors together with

three independent 1D paracrystal lattice distributions is applied.

GISANS

In analogy to GISAXS experiments, neutrons can be used to replace X-ray, and the theory introduced above is still applicable to GISANS due to the similarities between the Helmhlotz equation used for X-ray and the Schrödinger equation used for neutrons. In this thesis, GISANS is performed additionally in a time-of-ight (TOF) mode, which describes the pulse of neutron is separated with a chopper system and thus the neutrons with different velocities can be detected with a time-resolved 2D detector. Thus, TOF-GISANS provides sets of scattering data with varying wavelengths simultaneously. The wavelength of neutrons λ is defined by the deBroglie wavelength:

$$\lambda = \frac{h}{p(v_n)} \tag{2.35}$$

where h is Planck's constant, and $p(v_n)$ is the momentum of the neutrons depending on the velocity of the neutrons v_n. According to this formular, neutrons with low velocity give rise to a long wavelength, which are greatly affected by the gravity. Due to the influence of gravity on these slow neutrons, they travel to the detector with a parabola track along q_z direction. However, as the whole measurement is performed in small angle approximation with an incident angle less than 1°, the influence of gravity on several characteristic feautures (such as exit angle, specularly reflected peak and direct beam positions) can be neglected.

2.3.4 Grazing incidence wide angle scattering

As explained in section 2.2.2, crystalline structures are one influential factor governing the charge carrier mobility. To gain information about the crystal structure of polymer films at nanometer length scale, wide angle scattering in grazing incidence mode is applied.

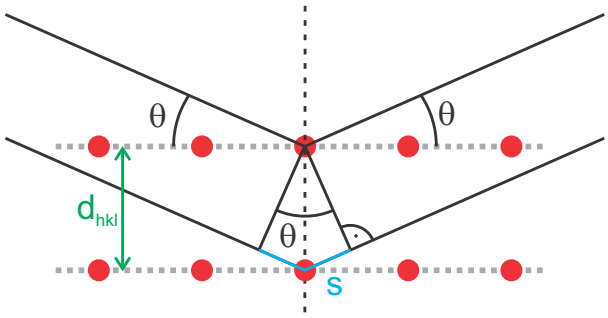

Figure 2.17: *Illustration of X-rays (black solid lines) scattering at two lattice planes (gray dotted lines) with a distance of d_{hkl} (green). The path difference of X-rays between two planes is indicated as S (blue).*

A monochromatic X-ray beam impinges at different lattice plane of a crystal with a grazing incident angle α_i. The incident angle is chosen above the critical angle of the investigated materials so that the X-ray beams can penetrate the whole polymer films. The scattered X-rays interfere and yield a maximum intensity if several lattice planes fulfill Bragg's law (as shown in Figure 2.17), which is given by:

$$n\lambda = 2d_{hkl}\sin\theta \tag{2.36}$$

where d_{hkl} is the distance of the hkl-lattice planes.

In principle, a GIWAXS setup is in analogy to GISAXS but with a much shorter SDD. Therefore, scattering signals with large angles are detected rather than small ones as compared with GISAXS. As a consequence, information about lattice constants, the degree of crystallinity and crystallite sizes are obtained from the scattering data under certain assumptions (i.e. small crystallites). In the 2d GIWAXS data, the Bragg reflections are detected as a function of q_{xy} and q_z. Due to the very short SDD and fixed incident angle α_i, in a GIWAXS measurement one cannot access the full q-range. In Figure 2.18, the original scattering data recorded from a 2D detector and the scattering data as a function of q_{xy} and q_z are presented, respectively. The inaccessible q-range is marked within the red curves. For measuring the Bragg peaks with q_z being the only non-zero component, the Bragg peak has to fulfill $\alpha_i = \alpha_f$ or an additional XRD measurement has to be performed. The measurement under $\alpha_i = \alpha_f$ condition is only necessary for a pole figure analysis. For polymer films investigated in this thesis, one measurement at a constant incident angle is sufficient. This is because the investigated polymer (PTB7) in the prepared films have a very low crystallinity of 20%.[74] We assume that a missing crystal population extracted from the inaccessible region in Fig 2.18 is unlikely. Therefore, the data analysis

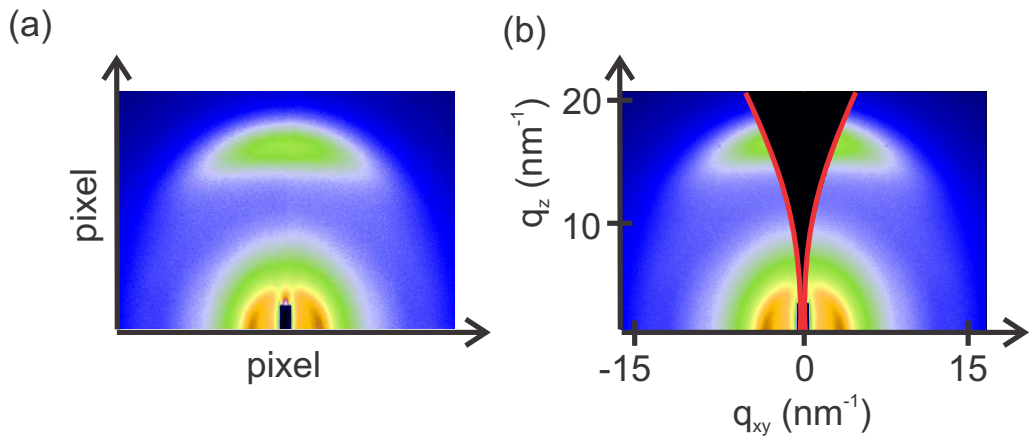

Figure 2.18: *(a) Original 2d GIWAXS data of a low crystalline PTB7 film spin-coated of solvent mixture trichlorobenzene:DIO as recorded by a 2d detector. (b) The same 2d GIWAXS data as a function of q_{xy} and q_z with the inaccessible q-range highlighted by two red curves.*

is proceeded on the original 2D detector images for particularly this system as commonly done in many other works.[75, 76] Furthermore, additional intensity corrections have to be applied due to the flat instead of spherically shaped 2D detector, which allows for an absolutely constant SDD distance for the whole measurement.

As all films investigated in this thesis are an assembly of semicrystallites embedded in an amorphous matrix, with the restriction of thin film configuration, the polymer crystallites show certain preferential orientation depending on the type of polymers. Hence, the resulted Bragg reflections presented in a GIWAXS pattern are more arc-like. In comparison, a ring-like Bragg reflection can be observed for isotropically orientated organic molecules such as fullerenes used in this work. From the analysis of these arc-like Bragg peaks, the prominent orientation of the crystallites can be extracted.

Chapter 3

Characterization methods

To address the morphology-property relationship of polymer thin films, characterization of their spectroscopic behavior, lateral and vertical structure, and the photovoltaic performance are performed in this thesis. In this chapter, all the involved experimental techniques are presented and the fundamental mechanisms are explained.

3.1 Spectroscopic and device characterization

Spectroscopic characterization methods like UV/Vis spectroscopy (section 3.1.1) is used to record the wavelength dependent absorption behavior of the investigated films. Moreover, electronic property such as the photovoltaic response (section 3.1.2) of the solar cell devices is explored by current-voltage measurements.

3.1.1 UV/Vis spectroscopy

In this thesis, a *Lambda* 35 UV/Vis spectrometer by *PerkinElmer Ltd.* is used to obtain the absorption spectra of polymer thin films. The light comes from a halogen and a deuterium lamp with complementary spectra, covering the ultraviolet and visible light range with a wavelength range from 190 nm to 1100 nm. The halogen lamp is switched to the deuterium one at the wavelength of 326 nm. The light beam generated from the lamps is modified as a monochromatic beam after passing through an optical grating and splitted into two beams, which will transmit through the investigated polymer thin film and the reference glass substrate separately. By subtracting the difference of two transmission signals, the transmission spectrum of the polymer thin film is obtained. The slit width can be varied to control the spectral resolution of each measurement. In general, smaller

slit widths yield greater spectral resolution but at the cost of total beam intensity that is transmitted through the monochromator.

The software *UV WinLab* by *PerkinElmer* is used to operate the spectrometer. An auto-zero measurement is carried out before the samples are measured in order to perform 100% transmission by eliminating the influence of the experimental equipment. An acid cleaned glass substrate is used as a reference sample. In this thesis, all absorption measurements are performed above the wavelength of 260 nm due to the classic signal-to-noise problem. Each absorption curve is recorded with a velocity of 120 nm/min and a slit width of 2 nm. The interval wavelength is 0.1 nm. Based on Beer-Lambert law, the transmission signal detected by a photo diode is converted to the wavelength dependent absorption spectra presented below:

$$A(\lambda) = -\log_{10}\left(\frac{I_t(\lambda)}{I_0(\lambda)}\right) = \alpha(\lambda) h \log_{10} \mathrm{e} \tag{3.1}$$

whereas $A(\lambda)$ is the wavelength dependent absorbance factor, $I_t(\lambda)$ and $I_0(\lambda)$ are transmitted beam intenisty and original incoming beam intensity, respectively. Using Beer-Lambert law, the fomular can be written in the form of absorbance as a function of film thickness h and absorption coefficient $\alpha(\lambda)$. Therefore, a simple thickness control method of different films made of the same material combination can be realized by the measurement of absorption curves of each film. Instead of using time-consuming film thickness measurement such as X-ray reflectivity, from the measured absorption spectrum $A(\lambda)$ one could easily obtain films with roughly the same thickness by adjusting film absorption. Moreover, one could extract the linear absorption coefficient $\alpha(\lambda)$ for samples with known film thickness h.

3.1.2 IV characterization

To characterize the photovoltaic behavior of polymer solar cells, a solar simulator *Solar - Constant* from *K. H. Steuernagel Lichttechnik GmbH* is used as the illumination source. A metal halide lamp provides an irradiation spectrumm similar to the solar spectrum, which is AM1.5 with a standard light intensity of 1000 W/m^2. This standard spectrum is calibrated with a reference silicon solar cell $WPVSRS - ID$ 3 by $FraunhoferISE$. In addition, a *Keithley* 2400 sourcemeter together with a readout software based on *Testpoint v*6 are applied to record the light induced photovoltaic performance, namely, current-voltage (IV) curves.

The solar cell device is placed 320 mm above the light source. Before starting the measurement, sweeping voltage instead of sweeping current is selected and the sweeping

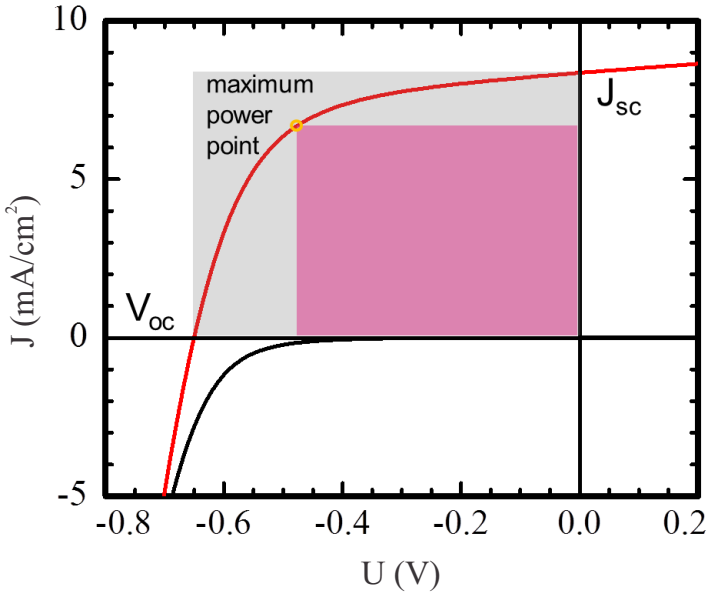

Figure 3.1: *Exemplary IV curve measured in dark (black solid line) and under standard illumination AM1.5 (red solid line) conditions. The maximum power point (yellow circle), V_{oc} and J_{sc} are depicted. The rectangle area colored with light pink indicates the maximum output power, and the grey rectangle area represents the product of V_{oc} and J_{sc}, and the ratio between these two area defines FF.*

range is defined between -1 V and +1 V with an interval of 0.01 V in the software *Testpoint*. To assure that only the probed pixel of the solar cell is exposed to the light during the measurement, a shadow mask is applied. The size of each pixel is individually measured with optical microscopy and not just taken from the size of the shadow mask. From the IV curves under dark and illumination conditions, the electronic characteristics about the solar cell are obtained. Particularly from the IV curve recorded under standard AM1.5 spectrum, detailed parameters such as the open circuit voltage V_{oc}, the short circuit current J_{sc} and the fill factor FF are extracted.

The overall power conversion efficiency is determined by following equations:

$$\eta = \frac{P_{out}}{P_{in}} = \frac{V_{oc} * J_{sc} * FF}{P_{in}} \tag{3.2}$$

$$FF = \frac{J_m * V_m}{J_{sc} * V_{oc}} \tag{3.3}$$

Here, P_{out} is the output power and P_{in} and input power, which is calibrated as 1000 W/m^2. J_m and V_m are the current and voltage values at the maximum power point. The decisive parameters regarding the solar cell efficiency are V_{oc} and J_{sc}, which are obtained by the intercept of the IV curves with the voltage and current axises, respectively. FF is

the ratio between the maximum output power and the product of V_{oc} and J_{sc}, as depicted in Figure 3.1, which is easily visualized by the slope of the obtained IV curve under illumination.

3.2 Structural characterization

3.2.1 Optical microscopy

As one of the most fundamental imaging techniques, optical microscopy is used to assure the sample quality and study the sample surface morphology in this thesis. Moreover, it is used to calculate the electrode size of the solar cells in order to obtain the power conversion efficiency. An *Axiolab* microscope (including a lamp Halogen 100) by *Carl Zeiss* is used and the images are captured via a *PixeLink USB Capture BE* 2.6 CCD camera. In general no polarization filters are used. Five different object lenses with five different magnifications: 1.25×, 2.5×, 10×, 50×, 100× can be selected, leading to different resolutions.

In this thesis, magnification of 1.25× and 100× are mostly used, giving resolution of 12.2 μm and 570 nm, respectively. The low magnification 1.25× is mainly used to check the overall film quality and to evaluate the pixel size of solar cells. The higher magnification 100× is used to investigate the film surface morphology in micrometer length scale. During the measurement of one set of samples, it is recommended not to change the light intensity.

3.2.2 Atomic force microscopy

Atomic Force Microscopy (AFM) is widely used to explore the surface topography, the phase contrast and the roughness of polymeric, biological and metallic materials. An *Autoprobe CP* Research AFM instrument (Thermomicroscope - Veeco, California, USA) is in use. For this type of AFM set-up, there are three main parts: the scanning part, the monitor part (including an optical microscopy), and the operating software.

Generally, the scanning part consists of an AFM tip, the laser system including a photodiode, a sample holder with a noise-damping system, and a feedback software. The tip used in this thesis is a conical shaped silicon tip covered with gold and has a curvature radius of 10 nm. It is attached to the bottom side of a triangle silicon microcantilever. The resonance frequency of this tip is between 40 kHz and 90 kHz.

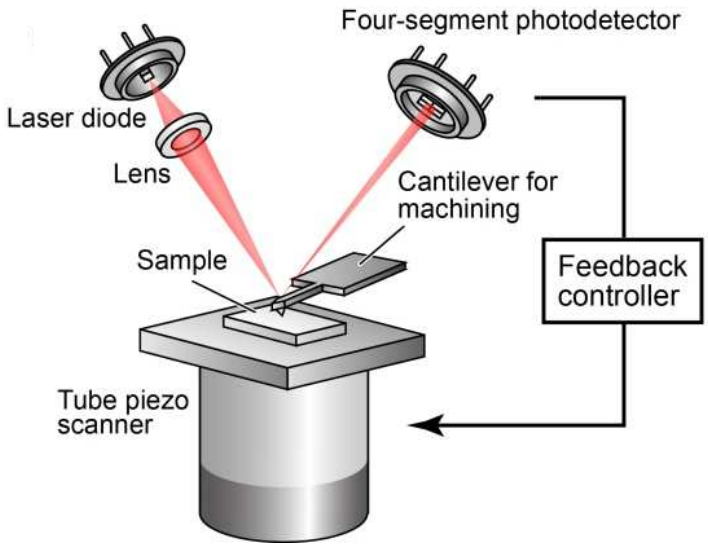

Figure 3.2: *Typical AFM setup is shown. Image taken from reference [77].*

Depending on the sample-tip distance and operation conditions three scanning modes are commonly used: contact mode, tapping mode and non-contact mode. When contact mode is in use, the sample-tip potential is measured in the repulsive region based on the Lennard-Jones potential, while the attractive potential dominates when tapping or non-contact modes are selected. In this thesis, our samples are made of soft polymers compared with hard silicon tip in use, therefore, tapping or non-contact mode is preferred to assure the sample surface is in a safe condition. However, in tapping mode the tip is occasionally touching the film surface.

Generally, four images are recorded for each measurement: two topography images with opposite scanning direction, one phase image and one error image. Phase images are particularly useful for materials such as the diblock polymers with different hardness for each block, or polymer embedded with metal nanoparticles due to the sharp contrast between each phase of the sample. For polymer-fullerene system investigated in this thesis, topography images are mainly used because the topographical characteristics are sufficient to provide the required information about the surface structure. The frequency is set slightly above the resonance frequency of the tip (40 kHz to 90 kHz) for tapping mode. All images are scanned 5% larger than the required scan size to assure the image quality. The overall two dimensional scan images contain 256 lines where each line contains 256 data points. For each sample, different spots are measured to obtain representative information, and at each spot images with different scan sizes from 1×1 to 8×8 μm^2 are taken. By applying the radial average and a Fourier transformation on these 2d images with different scan sizes, the power spectral density (PSD) function is obtained, which

provides statistical evaluation of the structure size of the film surface with the relevance to the reciprocal space. Consequently, the characteristic film surface structure revealed by PSD curves can be easily compared with the inner film structure obtained from X-ray scattering data.[78] Moreover, the roughness of the measured area can also be determined from the AFM data using the software $IP^{1.3}$.

3.2.3 X-ray reflectivity

As most properties of thin films are thickness dependent, the determination of the film thickness at a high precision is of utmost significant. X-ray reflectivity (XRR) measurements are very well suited to detect the film thickness from 2 up to 200 nm (determined by the angular range and resolution of the used XRR setup) at a very high precision of about 1-3 Å. The experiments are performed at a *Siemens D*5000 diffractometer at the Chair E21. The X-ray beam with a wavelength of $\lambda = 0.154$ nm is generated from a Cu target with a working voltage of 40 kV and current of 30 mA. The sample is mounted on a vacuum stage and a tantalum knife edge collimator is placed right above the sample (as shown in Figure 3.3) to cut off the large footprint of the X-ray at low incidence angles. A lead glass door is used to block the radiation of the X-ray in the direction of the operator. The collimated X-ray beam is obtained through a slit system, and impinges on the sample at an incidence angle θ. The reflected X-ray beam is guided through a graphite monochromator and recorded by a scintillation counter. An automatic absorber is used to reduce the X-ray intensity by a factor of 100, preventing the saturation on the detector.

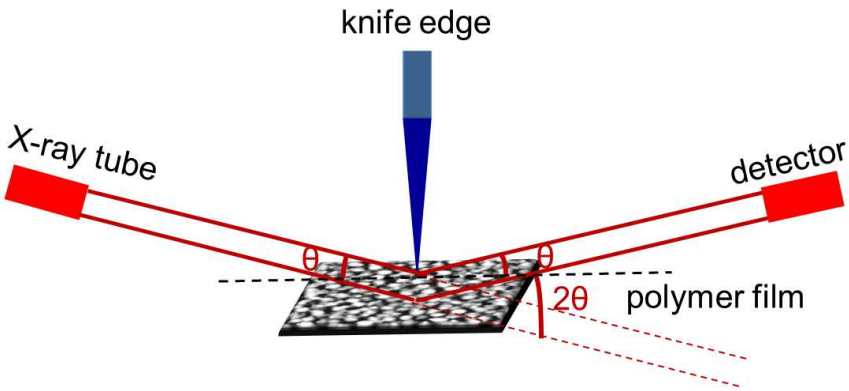

Figure 3.3: *Typical XRR setup using the $\theta/2\theta$ operation mode. A knife edge collimator is placed right above the sample to cut off the large footprint of the X-ray at lower incidence angle.*

XRR intensity is recorded as a function of the incident angle θ in the specular reflection

$\theta/2\theta$ mode. Due to different electron densities of different layers in the probed films, the reflection at the surface and interfaces occurs. For most materials the critical angle α_c is below 0.3°. If the incident angle is lower than the critical angle, total external reflection occurs. Above α_c the reflection from the different interfaces gives rise to interference fringes, which are measured as the oscillation in the XRR profiles. The thickness and roughness information of the layer is directly related to the period of the interference fringes, the height of the intensity and the slope of the curve. Normally the incident angle θ is varied from 0 to 7°. For the XRR measurements in this thesis, each measurement is divided into three angular ranges. For the measurement taken in the low incident angles range, an automatic beam absorber is selected to protect the detector from over saturation, whereas for higher angle measurement, the beam absorber is removed. The obtained data from three angular ranges are normalized and merged in a single XRR master curve. By fitting this curve with the software *Parret* 32, an iterative calculation is performed within the algorithm and compared with the measured reflectivity data. Therefore, the film thickness, the roughness of the surface and the interfaces, and the scattering length density values of the layers are extracted.[65]

3.2.4 Grazing incidence scattering

To detect buried structures of polymer thin films, grazing incidence X-ray scattering or neutron is used because it can deliver average statistical information over the illuminated area, and it can monitor possible phase transformations in real time without ultra-high vacuum conditions or any specific gas atmosphere. Thus, it gains tremendous attentions and popularity as an advanced technique to probe the structure of polymer thin films. In order to achieve the highest possible sensitivity, a grazing incidence angle is chosen depending on the system under investigation. The grazing incidence mode, by changing the sample-detector distance (SDD), different length scales are resolved as explained in section 2.3. In Figure 3.4, the principle setup of a grazing incidence scattering experiment is presented.

Grazing incidence wide/small angle X-ray scattering

The GIWAXS/GISAXS experiments are carried out at different beamlines. For the samples studied in Chapter 5, the GIWAXS/GISAXS experiments are performed at the P03 beamline at the third generation synchrotron ring PETRA III, DESY, Hamburg.[79] For those studied in Chapter 6, the scattering measurements are performed at the BW4 beamline at DESY, Hamburg. The X-ray beam of the P03 beamline is 750 times (12.8 keV) more intense than that of the BW4 beamline.[80] At BW4, the size of the X-ray beam is defined as 30×40 μm^2 by an assembly of several beryllium compound refractive lenses.

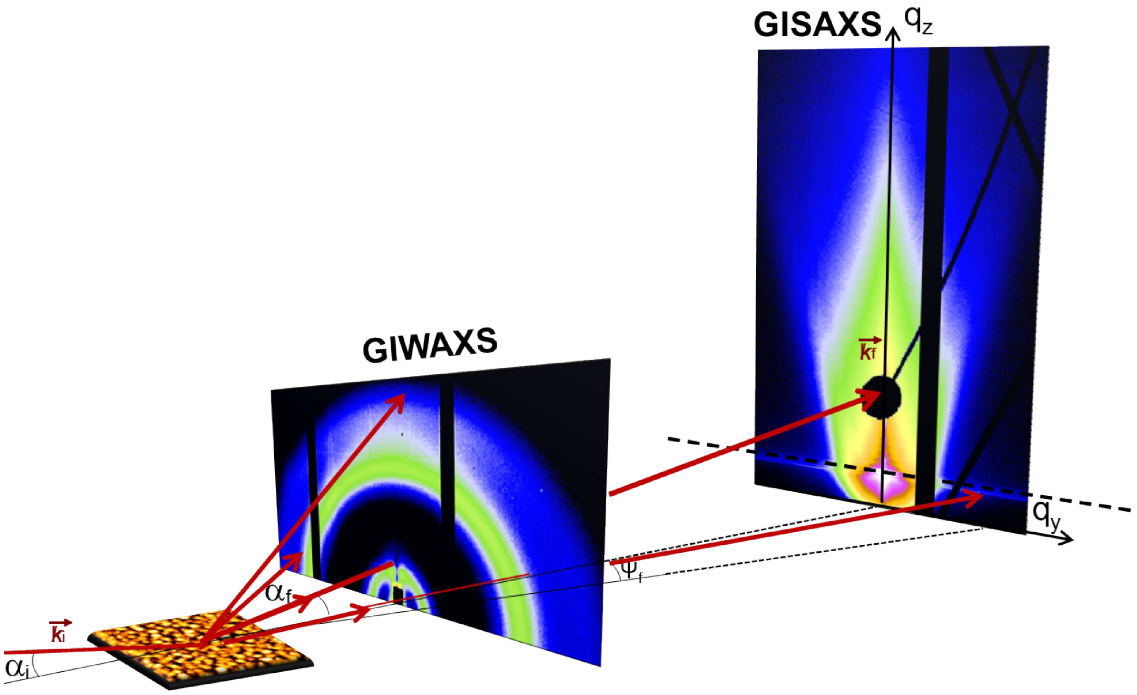

Figure 3.4: *Schematic presentation of the grazing incidence X-ray scattering setup. The X-ray beam (red) impinges on a sample with a grazing incident angle α_i and reflected with an angle of α_f. The 2d detector records the scattered intensity. Depending on the sample-detector distance different measurements are taken, consequently different length scales are resolved. Exemplary scattering data from PTB7-F100:$PC_{71}BM$ BHJ film (more details in Chapter 5) for grazing incidence wide angle X-ray scattering (GIWAXS) and grazing incidence small angle X-ray scattering (GISAXS) setups are shown.*

The X-ray beam with a wavelength of 0.138 nm irradiates on the sample and the scattering beam intensity is recorded by a *MARCCD* detector, which has 2048×2048 pixels with pixel size of 79.1×79.1 μm^2. For P03, a small sized X-ray beam (20×40 μm^2) with a wavelength of 0.0969 nm is used. Moreover, a three segments 2D detector Pilatus 300 K with no read-out noise is applied. It has in total 487×619 pixels with a pixel size of 172×172 μm^2. Nevertheless, the GIWAXS/GISAXS setups for both beamlines are in principle the same as depicted in Figure 3.4, the SDD is about 10 cm and 200 cm for GIWAXS and GISAXS measurements, respectively. The incident angle is selected according to the investigated materials. In general, the incident angle α_i is chosen above the critical angle of the investigated materials so that the X-ray beam can certainly penetrate the whole polymer film.[81] The direct and specular beams are shielded by two beamstops to avoid oversaturation on the detector.

From GIWAXS scattering data shown in Figure 3.5(a), information about molecular orientation, polymer backbone spacing, and crystal size of the investigated materials is revealed. To access the crystallinity information, further quantitative evaluation is realized by the vertical and horizontal sector integrals of the 2D GIWAXS images as shown in Figure 3.5(a). Moreover, the obtained data curves are fitted with a Gaussian function and evaluated with Scherer equation. As for analyzing the GISAXS data, vertical

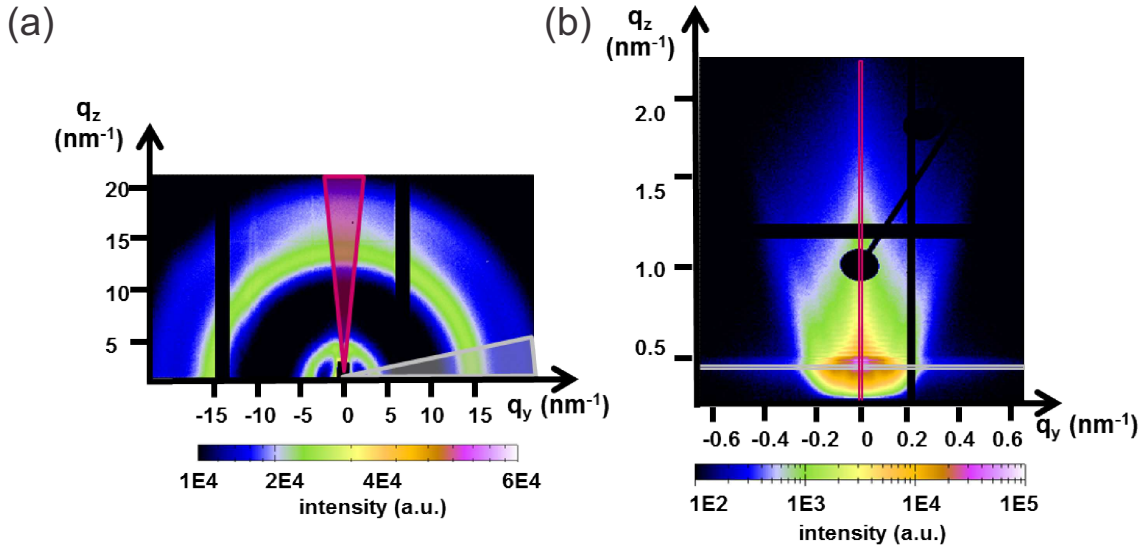

Figure 3.5: *(a) Exemplary GIWAXS sector integrals and (b) GISAXS line cuts. Scattering data are obtained from sample PTB7-F100:PC_{71}BM BHJ film (more details can be found in Chapter 5).*

line cut at $q_y = 0$ and horizontal line cut at Yoneda peak postion are performed as indicated in Figure 3.5(b). From the vertical line cuts, information like enrichment layer, correlated roughness can be obtained, whereas from the horizontal cuts, lateral structure, spatial correlation, and structure distribution can be extracted from the fit based on 1D paracrystal model within the frame of distorted wave Born approximation.

1D paracrystal model

For analyzing the GISAXS data, 1D paracrystal model is used to fit the horizontal line cuts at the Yoneda peak position. In this model as shown in Figure 3.6, two form factors (cylinder or sphere) and two structure factors with different polydispersity are considered. In addition, a resolution function fitted with a Lorentzian function at position zero ($q_y = 0$) and a constant background are also included. Despite of this model is based on a simplified mathematical approach and many other factors like the roughness effect and the population of each structure size are neglected, the extracted structure sizes are fairly

acceptable and in a good agreement with those obtained from real space characterization techniques.

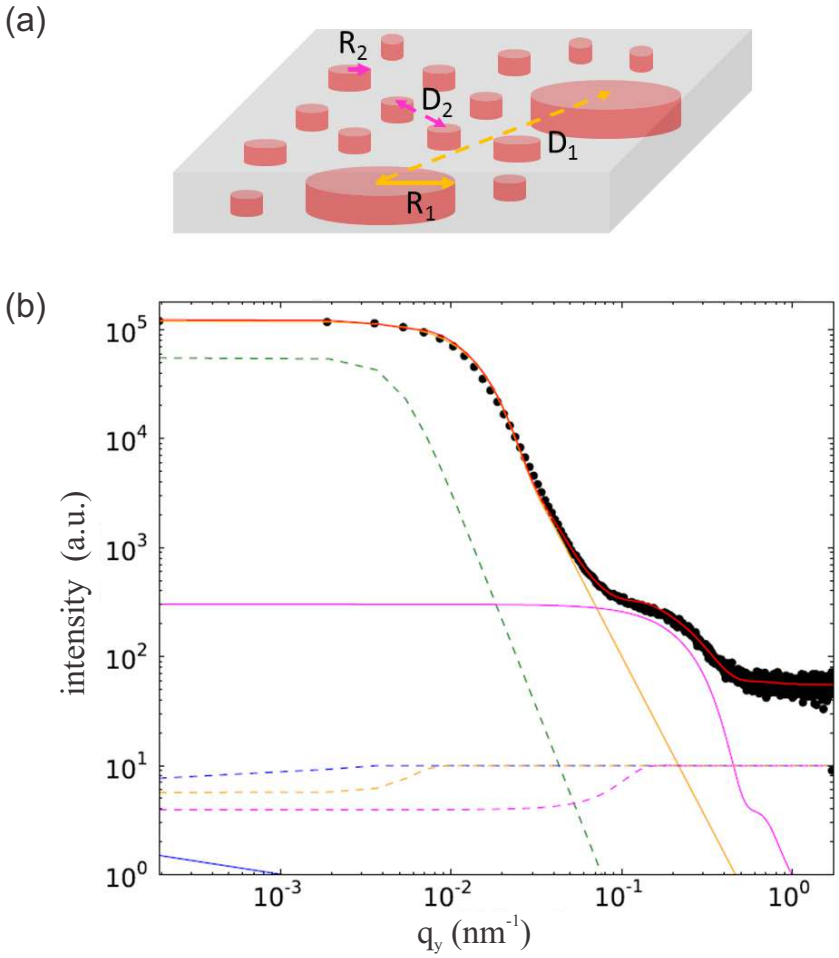

Figure 3.6: *1D paracrystal model fitted with (a) different size of cylinder structure within the film and (b) an exemplary fit of an horizontal cut at the Yenoda peak position. The bigger form and structure factor at low q_y values are indicated by the yellow solid and dash line, respectively. The smaller form and structure factor at high q_y values are shown by the pink solid and dash line, respectively. The resolution function (the green dash line) is fitted with a Lorentzian function at low q region.*

Time of flight - grazing incidence small angle neutron scattering (TOF-GISANS)

Neutron scattering is used with grazing incident mode to provide structural information of the films investigated in Chapter 7. Neutron scattering techniques are advantageous due to its high penetration depth compared with X-ray scattering techniques. Moreover, it has a low risk of damaging the sample compared with X-rays and is especially suitable

for measuring the air/water interface. Superior to X-ray, neutron scattering can be particularly used to distinguish the deuterated component from the protonated component for the bulk heterojunction film and provide a sharp contrast between the investigated materials. Time of flight (TOF) refers to the different speed of each neutron and therefore different arrival time to the sample. By recording the arrival time of each neutron and scattered position on the detector, TOF mode allows for rebinning of various data in order to obtain the best tradeoff between resolution and intensity. With the TOF-GISANS technique, both buried structure inside the film and the characteristic structure on the film surface can be simultaneously probed.

The TOF-GISANS experiments are performed at the REFSANS beamline at Forschungs-Neutronenquelle Heinz Maier-Leibnitz (FRM II) in Garching. The wavelengths of the neutron beam in use are variable from 2 to 20 Å, and it has a resolution of 10%. To record the scattered neutron signals, a multiwire 2D detector made of ^3He with an active area of 500 mm^2 is used. The ^3He detector contains 200 × 200 pixels with each pixel size of 2.92 × 2.92 mm^2. In addition, a double-chopper system with the required rotation speed is applied to define the neutron pulses. By varying the wavelength of the neutrons during one measurement instead of varying the incident angle, the TOF-GISANS data provide direct information covering a large q range with full penetration of the film from a single incident angle. For the TOF-GISANS experiments performed in this thesis, a wavelength range from 2 to 14 Å is selected. The SDD is set to be 10.5 m to obtain a reasonable q range. A fixed incident angle $\alpha_i = 0.45°$ is chosen to access the structural information of the bulk film at short wavelengths, and in addition only surface sensitive information at long neutron wavelengths. In one word, one can access both inner film and film surface morphology simultaneously with TOF-GISANS measurements. Due to relatively low neutron flux, a large silicon substrate of 60 × 60 mm^2 is needed, and 24 hours data acquisition time for each sample are necessary to obtain sufficient statistics.

The fitting procedure of the GISAXS profiles is used for fitting of the GISANS profiles as well, and the structure information is extracted from the fits. Besides, a precise determination of the SLD of the investigated material can be obtained from the evaluation of the wavelength-dependent critical angles. The determination of SLD is realized by identifying the critical angles from the vertical cuts at different wavelengths, and the extracted critical angles versus the wavelengths are fitted with a linear function, resulting into the SLD profiles along the normal to the sample surface, namely, the vertical material composition of the film.

Chapter 4

Sample preparation

The routine of preparing all investigated samples is described in this chapter. In the first part, all involved materials and solvents are introduced (section 4.1). Next, polymer film production on either glass or silicon substrates (section 4.2) for X-ray or neutron scattering investigations is described. Last, the fabrication procedure of solar cell devices (section 4.3) is presented as the device performance is essential for discussing the influence of the installed morphology in this thesis.

4.1 Materials and solvents

All involved materials can be classified into five categories: electron donors, electron acceptors, electron blocking polymers, solvents, and solvent additives. The low bandgap copolymer PTB7 based on the thieno[3,4-b]thiophene-alt-benzodithiophene unit were selected as electron donors while the fullerene derivatives [6,6]-phenyl-C71-butyric acid methyl ester ($PC_{71}BM$) were selected as electron acceptors. Moreover, poly(3,4-ethylenedioxythiophene): poly(styrenesulfonate) (PEDOT:PSS) was applied as electron blocking layer to enhance the power conversion efficiency by defining the current direction. In this thesis, halogenated solvents chlorobenzene, 1,2-dichlorobenzene and 1,2,4-trichlorobenzene as well as solvent additive 1,8-diiodooctane (DIO) were used to prepare the polymer solution. Halogen-free solvents methanol, ethanol, 2-propanol, 1-butanol were used as post treatment after the deposition of the organic photovoltaic layer. The parameters of all the involved polymers in this thesis such as the molecular weight (M_w), polydispersity (PDI), solubility and the source are listed in table 4.1.

material	source	M_n	M_w	PDI	purity
PTB7-F00	1-material Inc.	32380[a]	68000	2.1	n.a.
PTB7-F40	1-material Inc.	37083[a]	89000	2.4	n.a.
PTB7-F60	1-material Inc.	36800[a]	92000	2.5	n.a.
PTB7-F100	1-material Inc.	44760[a]	94000	2.1	99.99%
$PC_{71}BM$	1-material Inc.	1030.93	n.a.	-	98.5%
PEDOT:PSS-PH1000	Ossila	n.a.	n.a.	n.a.	99%

Table 4.1: *Information about all involved polymers such as the source, the molecular weights M_n and M_w, the polydispersity PDI and the purity of the organic compounds used in this thesis offered by the suppliers. The molecular weight is given in g/mol. [a] The molecular weight M_n of all polymers were determined via the formular $M_n = M_w/P_d$.*

Electron donor

Poly[[4,8-bis[(2-ethylhexyl)oxy]benzo[1,2-b:4,5-b']dithiophene-2,6-diyl][3-fluoro-2-[(2-ethylhexyl)carbonyl]-thieno[3,4-b]thiophenediyl]] commonly known as PTB7, has demonstrated the highest efficiency among all the reported polymers so far.[15, 82, 83] The chemical structure of PTB7 is shown in Figure 4.1. PTB7-Fxx represent slightly different types of PTB7 with varied ratio between fluorinated thienothiophene unit and non-fluorinated thienothiophene unit. The chemical structure of different PTB7-Fx still stays similar. Compared with well studied P3HT, the relatively lower band gap of PTB7 makes its absorption coefficient higher and blue shifted. Consequently, it shows a much broader absorption spectrum. Besides, a higher hole mobility of 5.8×10^{-4} $cm^2/V\cdot s$ is also observed for PTB7.[41]

Electron acceptor

The second component of the blend system is [6,6]-phenyl-C71-butyric acid methyl ester, denoted as $PC_{71}BM$, the derivatives of the C_{71} Buckminsterfullerenes.[84] The chemical structure of both are shown in Figure 4.1. It acts as efficient n-type semiconductor material well soluble in organic solvents. $PC_{71}BM$ is an electron-conducting organic compound and has an electron mobility of 1×10^{-3} $cm^2/V\cdot s$.[85] It absorbs visible light more efficiently than well studied $PC_{61}BM$ due to its upshifted LUMO level.[86]

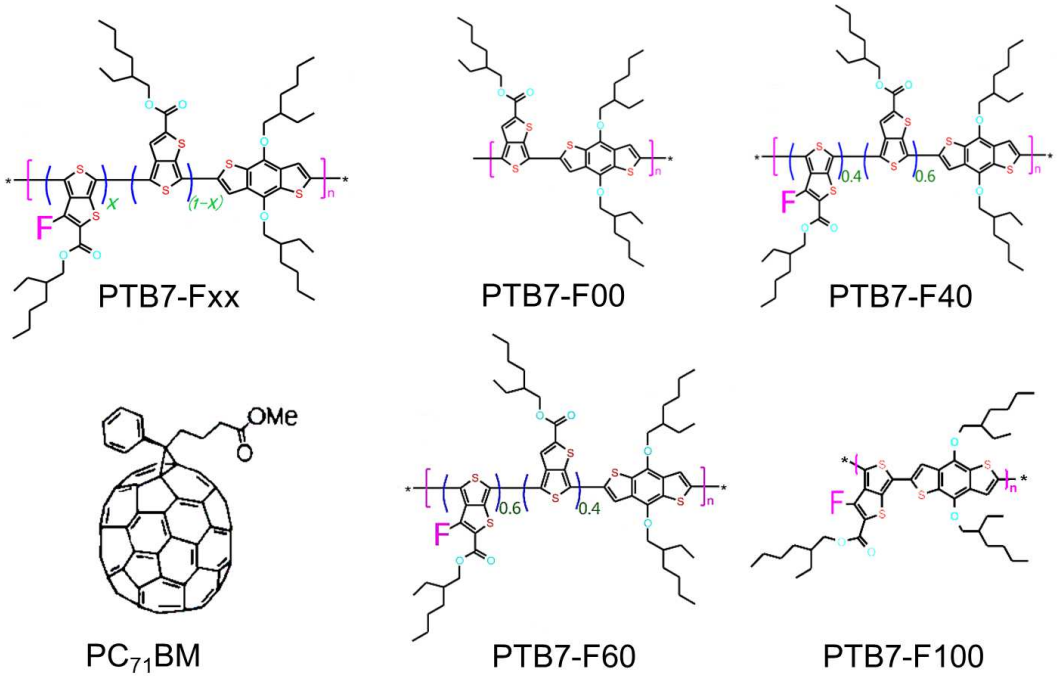

Figure 4.1: *The chemical structures of the investigated polymers and fullerenes.*

Electron blocking polymer

Poly(3,4-ethylenedioxythiophene):poly(styrenesulfonate) (PEDOT:PSS) is a semi-transparent mixture of two polymers: PEDOT (94%) and PSS (6%) (see figure 4.2), dispersed in H_2O at the ration of 1:2.5. The density is approximately 1 g/cm^3. PEDOT:PSS-PH1000 used in this thesis not only provides high conductivity up to 1000 S/cm (approx. 200 Ohm/sq), but also high transparency and stability. PEDOT:PSS is applied due to its electron-blocking property as well as its easy processability. It can define the current direction by allowing only holes going through to improve the power conversion efficiency.

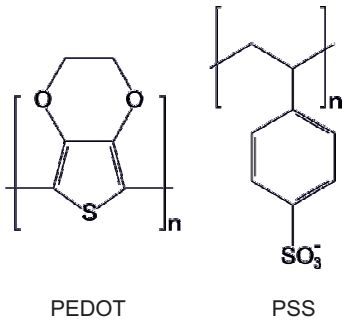

Figure 4.2: *Chemical structure of the electron blocking polymer PEDOT:PSS.*

Solvents

Chlorobenzene, is an aromatic organic compound with the molecular formula C_6H_5Cl. The colorless, flammable liquid is a common solvent and widely used as intermediate in the manufacture of other chemicals. The boiling point of chlorobenzene is 131°C, and its density is 1.11 g/cm^3 at 25°C.

1,2-dichlorobenzene, is a derivative of benzene, a common colorless organic compound with molecular formula $C_6H_4Cl_2$, which consists of two adjacent chloride substituents. Its boiling point is higher than chlorobenzene, that is, 180°C, and the density is 1.31 g/cm^3 at 25°C.

1,2,4-trichlorobenzene, is also a derivative of benzene with three chloride substituents, and the molecular formula $C_6H_3Cl_3$. It appears also as colorless liquid with a boiling point of 214°C and density of 1.46 g/cm^3 at 25°C.

Apart from the halogenated solvents mainly used as host solvents to dissolve polymers and fullerene, halogen free solvents methanol, ethanol, propanol, butanol are used as post solvent treatment after the deposition of the active layer, meaning that additional spin-coating procedure is applied at certain optimized spin-coating parameters with these alcohol solvents. The effect of the solvent treatment will be deliberately investigated and explained in chapter 7. The chemical structure of all involved solvents is presented in Figure 4.3.

Solvents additive

1,8-diiodooctane (DIO), has a relative density of 1.84 g/cm^3 at 25°C. The molecular weight is 366.02 g/mol, and its initial boiling point range is 332.49°C at 760 mmHg. It is purchased from Sigma-Aldrich and used as supplied. It was firstly reported by Peet et al. that processing additives could promote the performance of several high efficiency low bandgap polymers.[87] Followed soon by the discovery that with the introduction of additive DIO into the host solvent, the device performance of PTB7:$PC_{71}BM$ solar cells can be dramatically improved due to its selective solubility of fullerene molecules.[41, 88]

4.2 Polymer thin films

A polymer-based solar cell device has an architecture with several layers, which makes it difficult to probe the film morphology by e.g. X-ray scattering due to the scattering

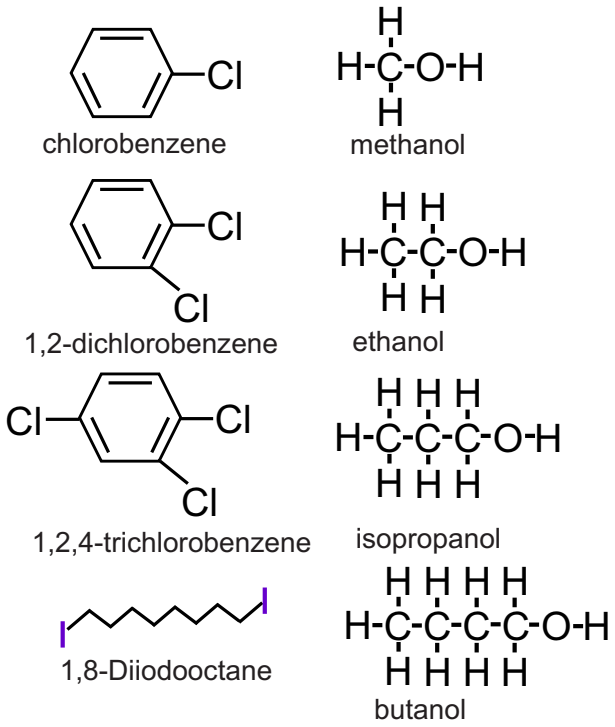

Figure 4.3: *The chemical structure of used solvents and processing additives.*

background from rough ITO substrates or other materials underneath the polymer blend layer. Also, the multi-layer device makes it impossible to focus on the absorption features arising from the most interesting active layer. In order to better concentrate on investigating the active layer properties, polymer thin films are prepared on alternative substrates such as glass or silicon instead of ITO substrates. With different techniques, the requirement for the sample size is different: generally silicon or glass substrate is cut with size 22×22 mm^2; For investigation with neutron scattering, however, large silicon substrate with size of 60×70 mm^2 is required to assure the statistics of the measurement due to the relatively low neutron flux. All substrates are cleaned with hot acid bath at 80°C for 15 mins with components as below:[89]

- 54 mL deionized water (H_2O)
- 84 mL 30 % hydrogen peroxide (H_2O_2)
- 198 mL 96 % sulfuric acid (H_2SO_4)

Afterwards, these acid-cleaned substrates are thoroughly rinsed with deionized water and dried with oil free nitrogen. To make the morphology of the active layer comparable on different substrates, PEDOT:PSS is applied on silicon substrate exactly as is used for

ITO substrates, referred as PEDOT:PSS modified silicon substrate, which is mostly used as X-ray scattering technique in this thesis. However, when glass substrates are used to compare the absorption behavior of the polymer blend films, PEDOT:PSS is excluded in order to rule out the possible influence introduced by the PEDOT:PSS layer.

Solution preparation

Both polymer PTB7 and the organic compound $PC_{71}BM$ are poorly soluble in the organic solvents at room temperature. In comparison, the solubility of $PC_{71}BM$ is higher than that of the high molecular weight polymer PTB7. To prepare the polymer blend film, the PCBM powder is firstly dissolved into the used solvent until complete dissolution, and then the required amount of pristine PCBM solution is added to the corresponding amount of polymer according to the required total solution concentration. To start the solution preparation, 400 μL selected solvent measured with a pipette is poured into a glass container with proper volume to remove all the possible dirts out of the glass. Afterwards, the glass container is dried with oil-free nitrogen, and labled with detailed information such as the material, solvent, and sample name. After mixing the polymer and fullerene solution, the sample bottle is sealed with parafilm to avoid evaporation of the solvent. Then the mixed solution is stirred overnight at 60°C in a sandbath to achieve better homogenity. After being fully dissolved, the mixture of the polymer blend (PTB7:$PC_{71}BM$) solutions are ready to fabricate solar cells on the next day. Note that it is extremely crucial to perform the whole solution preparation process in the glove box filled with nitrogen atmosphere.

Spin coating

All polymer films investigated in this thesis are prepared by the spin-coating method. 200 μL solution is applied on the top of the substrate with a size of 100-1000 μL pipette. The cap of the spin-coater is immediately closed to avoid splashing solution spots, and the "start" button is pressed immediately after solvent deposition. During this process, most of the solution is thrown off the substrate, and only a thin layer is formed. The polymer thin film gets thinner due to the evaporation of the solvent while spin-coating. There are three adjustable parameters for the spin coating equipment as shown in table 4.2. The relationship between film thickness and other factors is described with equation [90]:

$$d = A \left(\frac{1950\, rpm}{\omega} \right)^{1/2} \left(\frac{c_0}{20\, gL^{-1}} \right) \left(\frac{M_w}{100\, kg\ mol^{-1}} \right)^{1/4} \tag{4.1}$$

material	rotation speed ω (rpm)	acceleration time (s)	time (s)
PEDOT:PSS	3000	9	60
PTB7:$PC_{71}BM$	1000	9	60
alcohol solvents	2500	9	120

Table 4.2: *Spin-coating parameters for preparation of thin films.*

where d is the fabricated film thickness. A is a parameter of unit length describing the influence of the experimental setup and the ambient conditions. The film thickness is controlled by solution concentration c_0, the molecular weight M_w of the used material, and the rotation speed ω. In this thesis, all the detailed spin-coating parameters for different layer fabrications (PEDOT:PSS layer, PTB7:$PC_{71}BM$ layer, and post treatment with alcohol solvents) are listed in Table 4.2.

4.3 Solar cell fabrication

Solar cells are multiple layers devices, which contain basically a photovoltaic layer sandwiched between two electrodes with different work function. For the type of polymer based BHJ solar cell investigated in this thesis can be found in previous chapter in Figure 2.1, a thin transparent layer of indium tin oxide (ITO) serves as the anode whereas an ultra-thin aluminum layer functions as the cathode. In between, the PEDOT:PSS blocking layer and an active layer consisting of a mixture of polymer and fullerene derivative are spin-coated, respectively. A proper polymer blend film thickness is achieved by adjusting the solution concentration and other parameters of the spin-coater.
The standard solar cell fabrication procedure in a lab scale is presented in Figure 4.4. All the samples are prepared on glass-ITO substrates, purchased from *SOLEMS* with the size of 2.2×2.2 cm^2. Part of the ITO layer is chemically etched away by zinc paste and diluted hydrogen chloride solution and rinsed with deionized water in order to avoid possible short circuit in the solar cell. All patterned substrates (as shown in Figure 4.4 S_1) are then cleaned in an ultrasonic bath with alconox solution and three organic solvents (ethanol, acetone, and isopropanol for 10 minutes, respectively). After every wet cleaning step, the substrates are dried with oil free nitrogen gas. Oxygen-plasma treatment is performed on the cleaned ITO substrates for 10 minutes to increase the hydrophilicity of the surface. Before spin-coating the PEDOT:PSS layer, the PEDOT:PSS solution is dissolved in an ultrasonic bath for 10 minutes to untangle the polymer chains and immediately filtered through PVDF filters (0.45 μm), then spin-coated for 60 s at 3000 rpm rotation speed

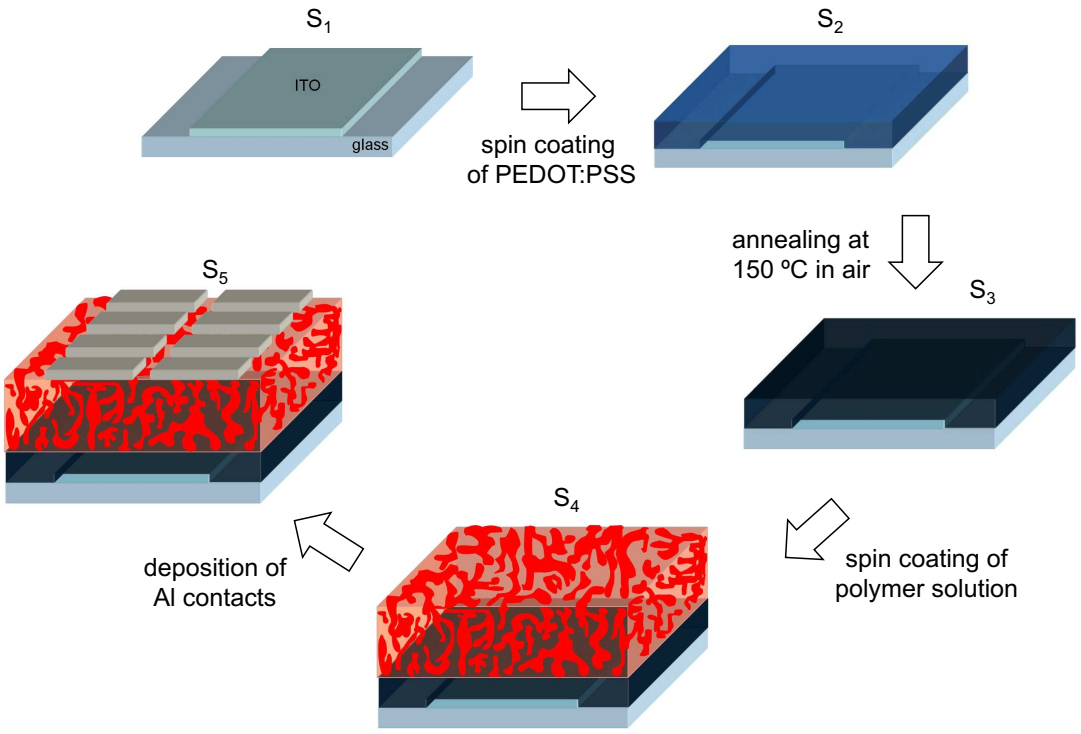

Figure 4.4: *The schematic representation of the individual steps of the functional stack build-up for standard polymer-based solar cells used in the present investigation.*

(Süss MicroTec Delta 80 spin-coater) under ambient conditions, corresponding to step S_2 in Figure 4.4. The obtained PEDOT:PSS layer is annealed at 150 °C for 10 minutes on a copper plate in air to remove the residual water, depicted as S_3.

A homogeneous active layer is achieved by spin-coating, seen as S_4 in Figure 4.4. The parameters of acceleration and rotation time are listed in table 4.2. For the effect of solvent treatment on PTB7:PC_{71}BM BHJ blend films investigated in chapter 7, additional solvent treatment of the active layer in a nitrogen atmosphere is applied before the evaporation of the aluminum electrode. Solvent treatment is newly discovered to effectively enhance efficiency of polymer solar cells by removing the residual processing additives.[91, 92] The devices are completed with a thermal deposition of an aluminum layer under vacuum conditions (3.8×10^{-5} mbar), depicted as S_5. The deposition process is monitored by a quartz crystal ratemeter purchased from *Inficon*. The deposition rate starts from 0.1 Å/sec and speeds up to 20 Å/sec, and it is manually stopped when the film thickness reaches 100 nm. The effective area of the devices as determined by the overlap of aluminum and ITO electrodes is about 15 mm^2. For each piece of ITO substrate, eight pieces of mini solar cells are fabricated.

Chapter 5

Fluorination induced morphology of PTB7:$PC_{71}BM$ BHJ system

The number of articles in the field of conducting polymers has risen exponentially in the past few decades. Considerable efforts have been devoted to developing low bandgap polymers in order to promote the efficiency of the electronic devices, e.g. OPV and OLED.[93, 94, 95] In this aspect the fluorination of conducting polymer is particularly attractive due to its unique resulting features: (1) It has a strong influence on inter- and intramolecular interactions; (2) The incorporation of fluorine could tune the energy levels of the polymers; and (3) It has elevated resistance to degradation (e.g. the enhanced hydrophobicity, great distinguished thermal and anti-oxidative stability), all of which enable fluorinated polymers hold exceptional promise in enhancing the efficiency as well as lifetime for polymer-based solar cells.[96, 97, 98]

To date, polymer-based solar cells made of highly efficient copolymer PTB series, based on thieno[3,4-b]thiophene-alt-benzodithiophene unit and $PC_{71}BM$ in a bulk heterojunction geometry have been developed and recieved high attentions. In this chapter, a branch of these polymers, PTB7-Fx with incorporation of different amount of fluorine atoms at the same position of submonomer thieno[3,4-b]thiophene blended with $PC_{71}BM$, is thoroughly investigated to address the relation between the film morphology and device performance. The main aim of this work is to study the effect of varied degree of fluorination on the resulting device performance. The film surface structure is investigated by direct imaging techniques such as optical microscopy and AFM. The inner film structures, crystal orientation as well as the crystal behaviour are probed by advanced scattering techniques such as GISAXS and GIWAXS. By combining all the probed information, a representative length scale model of the active layer is obtained and the reason for the efficiency variance as a function of the degree of fluorination is identified. The

work in this chapter has been published as an article in the journal Advanced Energy Materials.[99].

The chemical structures of investigated polymers and fullerene can be found in Figure 4.1. PTB7 with varied degree of fluorination, denoted as PTB7-Fx, is synthesized by the substitution of hydrogen atoms at the thieno[3,4-b]thiophene unit along PTB7 chain with fluorine atoms. The ratio between fluorinated thieno[3,4-b]thiophene unit and non-fluorinated one defines the X in PTB7-Fx.

5.1 Solar cell performance

In Figure 5.1, the device performance of PTB7-Fx:$PC_{71}BM$ (1:1.5 by weight) solar cells with 3 vol% DIO as solvent additive is presented. In order to elucidate the potential influences induced by additional interlayers, the simplest device configuration with identical processing procedure is adapted for all the samples, which consists of only one ative layer, one electron blocking PEDOT:PSS layer and two electrodes. Most significantly, as mentioned above, the main focus of this work is to address the fluoriantion induced morphology-efficiency relationship instead of fabricating the best performed polymer solar cells, easier device configuration is thus preferred in present work. It should be noticed that only the IV curves of solar cell devices with solvent additive DIO are presented as it is already well-known that only DIO containing devices give rise to decent device performances for particularly PTB7:$PC_{71}BM$ BHJ system.[41, 100]

The characteristic parameters of the corresponding solar cells are listed in Table 5.1. In general, PCE increases from 2.69% to 3.86% with increasing fluorine content. For each parameter, J_{sc} remains rather similar (about 14 mA/cm^2) for PTB7-F00, F40, and F60, and it gets improved up to 17.44 mA/cm^2 for solar cells made of PTB7-F100. The FF, stays almost constant (45±1.5%) for devices made of all four polymers. V_{oc}, however, is observed to increase continuously, which is therefore mainly responsible for the enhanced PCE as a function of fluorination content. Particularly for solar cell made of PTB7-F100: $PC_{71}BM$, the improvement of PCE is ascribed to a simultaneous enhancement of both V_{oc} and J_{sc}.

Although the values of V_{oc} and FF in our devices are relatively low as compared to the highest efficient solar cell published for the same material, a comparable or even higher values of J_{sc} is obtained especially for those devices made of PTB7-F100:$PC_{71}BM$ (17.2 mA/cm^2). The reason for the relatively low V_{oc} and FF may possibly arise from the trace impurities in organic solar cells, the absent hole blocking layer or optical spacing layer (TiO_x layer), as well as the negative influence of normal ambient air conditions.[30, 82, 101]

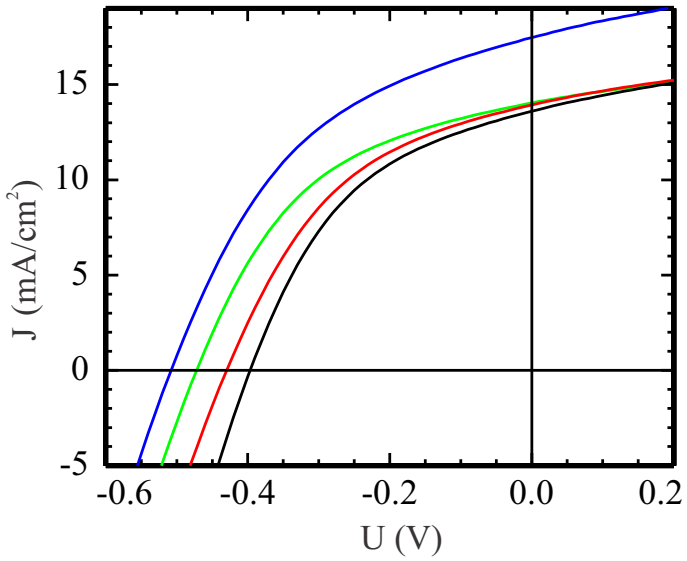

Figure 5.1: *IV curves of PTB7-Fx:$PC_{71}BM$ solar cells made from polymers with different degree of fluorination: PTB7-F00 (black), PTB7-F40 (red), PTB7-F60 (green), and PTB7-F100 (blue) with 3 vol% DIO. The measurements are performed under standard spectrum AM 1.5 with the illumination intensity 1000 W/m^2.*

Among all, the ambient air condition is assumed to be the key issue limiting the device performance, as it is widely recognized that the low bandgap polymer PTB7 has much lower air stability as compared to other commonly used semiconducting polymers, e.g. P3HT. Further improvements of FF and V_{oc} are feasible by controlling the above mentioned negative factors, however, the optimization of the final device performance will not cause a change in the morphology of the active layers and the trend of V_{oc} with increasing fluorine content. Therefore, the obtained results are sufficient to provide a comprehensive understanding on a more fundamental level about the effect of material property on the device performance.[102, 82]

sample	$\mathbf{J_{sc}}$ **(mA/cm^2)**	$\mathbf{V_{oc}}$ **(V)**	**FF (%)**	η **(%)**
PTB7-F00:PC_{71}BM:DIO	13.94	0.42	46.2	2.69
PTB7-F40:PC_{71}BM:DIO	13.93	0.43	43.6	2.61
PTB7-F60:PC_{71}BM:DIO	14.03	0.47	45.6	3.02
PTB7-F100:PC_{71}BM:DIO	17.73	0.51	43.6	3.86

Table 5.1: *Characteristic parameters of solar cells prepared from PTB7-Fx:$PC_{71}BM$ dissolved in chlorobenzene with the 3 vol% additive DIO.*

5.2 Optical properties

The UV/Vis absorption spectra of neat PTB7-Fx films and PTB7-Fx:$PC_{71}BM$ blend films spin-coated from solvent mixture CB:DIO are normalized and plotted in Figure 5.2 (a) and (b), respectively. For neat PTB7-Fx films in Figure 5.2(a), all films show similar shape of absorption spectrum, indicating that the introduction of fluorine along the polymer backbone has no significant impact on the absorption properties. A dominant absorption peak with a shoulder between the wavelength range of 600 nm and 750 nm is assigned to polymer PTB7. Moreover, a relatively weak absorption peak arising from PTB7 as well is visible at about 410 nm, and it appears as a shoulder in blend films in Figure 5.2(b). Furthermore, a blue-shift effect is observed from PTB7-F00 to PTB7-F100 with introducing more electron-withdrawing fluorine atoms.[103] The blue-shift is caused by a decreased conjugation length of the polymers as a result of a reduced electron density out of the thiophene ring with increasing the amount of electron withdrawing fluorine atoms.[103] However, the blue-shift effect is relatively weak for low degrees of fluorination as compared with that of the fully fluorinated PTB7-F100.

In Figure 5.2(b), for PTB7-Fx:$PC_{71}BM$ films spin-coated from solvent mixture CB:DIO multiple absorption peaks are observed. The absorption peaks at about 370 nm and 460 nm occurring in the blend film are identified as the contribution from $PC_{71}BM$, which absorbs mainly in the lower wavelength range of the measured spectra. The overall absorption spectrum of PTB7-Fx:$PC_{71}BM$ BHJ film follow a linear superposition of the absorption spectrum of individual material $PC_{71}BM$ and PTB7. As a consequence, PTB7-Fx:$PC_{71}BM$ BHJ films exhibit broader absorption spectra, which directly promote the exciton generation rate and consequently an enhanced device performance. Similar blue-shift phenomenon is observed again for PTB7-Fx:$PC_{71}BM$ BHJ films with an increasing fluorine content as seen in Figure 5.2(b) due to the decreased conjugation length of polymer mentioned for neat PTB7-Fx films.

In summary, for both neat fluorinated PTB7-Fx films and PTB7-Fx:fullerene BHJ films, PTB7 with higher degrees of fluorination shows slightly lower degree of ordering and decreased π-conjugation length, which leads to the blue-shift effect of the absorption spectrum with increasing fluorine content. As no distinct differences regarding the optical property of the four polymers with different degrees of fluorination can be observed, further investigations about film surface morphology and inner morphology are subsequently carried out.

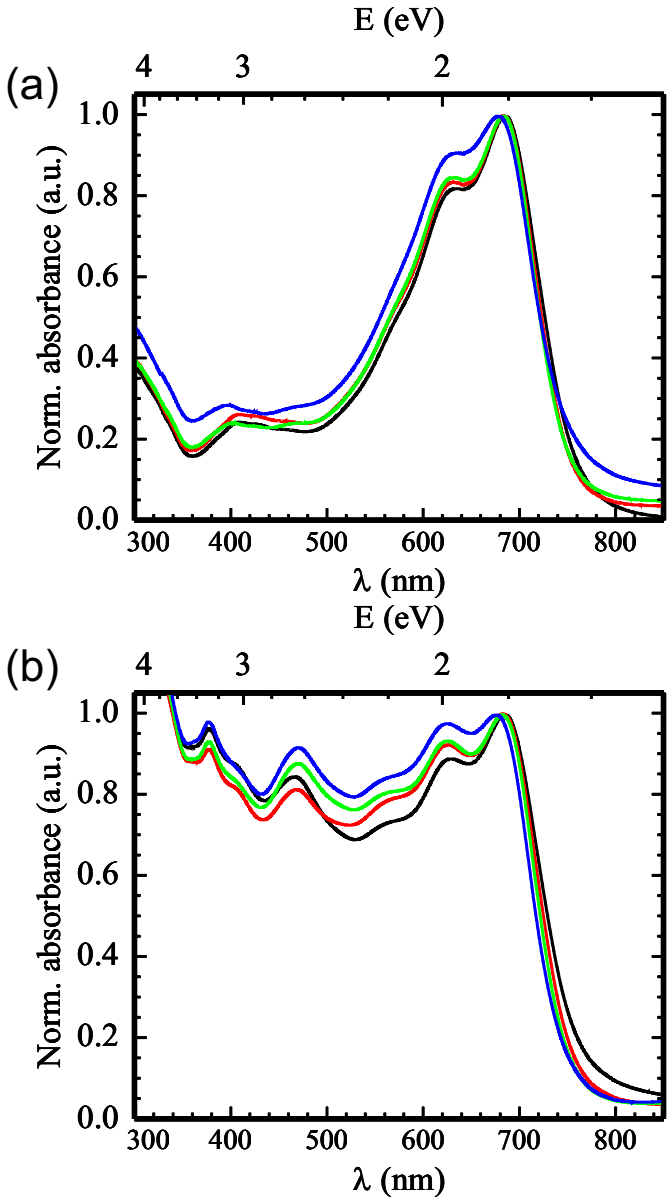

Figure 5.2: *Absorption spectra of (a) PTB7-Fx and (b) PTB7-Fx:$PC_{71}BM$ BHJ films made from solvent mixture CB:DIO (97:3 in volume). PTB7-F00, PTB7-F40, PTB7-F60, PTB7-F100 are indicated by the color black, red, green, and blue, respectively.*

5.3 Mesoscopic structure

5.3.1 Mesoscopic surface structure

In Figure 5.3, the optical microscopy of films spin-coated from PTB7-Fx:$PC_{71}BM$ solutions without and with DIO are presented. The bright dots observed in the upper row for PTB7-Fx:$PC_{71}BM$ films without DIO is suggested to be aggregated fullerene clus-

ters, which is also observed for other polymer:fullerene BHJ systems as it is known that the fullerenes tend to aggregate.[104, 105] The occasional red clusters appear in the first two images are identified as undissolved polymers PTB7 as it has very large molecular weight. Clearly, for as-spun PTB7-Fx:$PC_{71}BM$ films the amount of $PC_{71}BM$ clusters increases with increasing fluorine content. In contrast, for all the DIO containing PTB7-Fx:$PC_{71}BM$ films in the bottow row no obvious $PC_{71}BM$ clusters can be observed for the reason that DIO can selectively dissolve $PC_{71}BM$ and thus improve the miscibility between PTB7 and $PC_{71}BM$. Due to the limited resolution of optical microscopy, all DIO containing films are viewed as rather homogeneous ones and no clear structure can be observed.

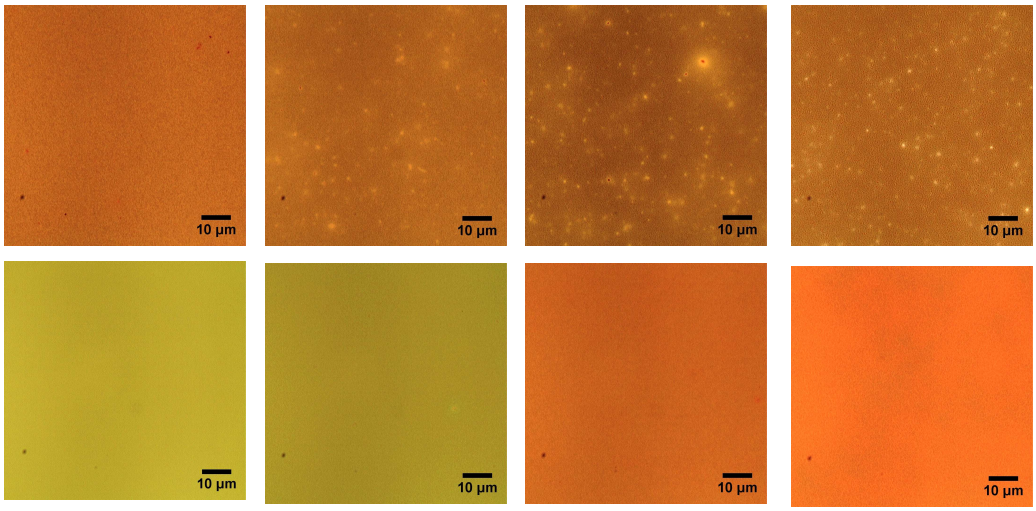

Figure 5.3: *Optical microscopy images of PTB7-Fx:$PC_{71}BM$ BHJ blend films prepared from chlorobenzene without (upper row) and with (bottom row) 3 vol% solvent additive DIO. From left to right, optical images are obtained from PTB7-F00:$PC_{71}BM$, PTB7-F40:$PC_{71}BM$, PTB7-F60:$PC_{71}BM$, and PTB7-F100:$PC_{71}BM$, respectively.*

To overcome the issue of limited resolution, AFM is applied to resolve structure size at nanometer length scale. In Figure 5.4, AFM topography images of PTB7-Fx:$PC_{71}BM$ BHJ films spin-coated from CB and solvent mixture CB:DIO are shown, and the different colors represent the height variance on the film surface. In the upper row, large bright clusters are observed, which are identified as large $PC_{71}BM$ rich domains. The dark region in the images corresponds to the polymer PTB7 matrix, agreeing with many other researches on polymer:fullerene BHJ system.[41, 106] Again, the obvious $PC_{71}BM$ clusters for the blend films without solvent additive DIO in upper row of Figure 5.4 confirms the tendency of fullerene agglomeration. Moreover, from the top view of the films relatively irregularly packed $PC_{71}BM$ clusters with a large size distribution from 50 nm to 200

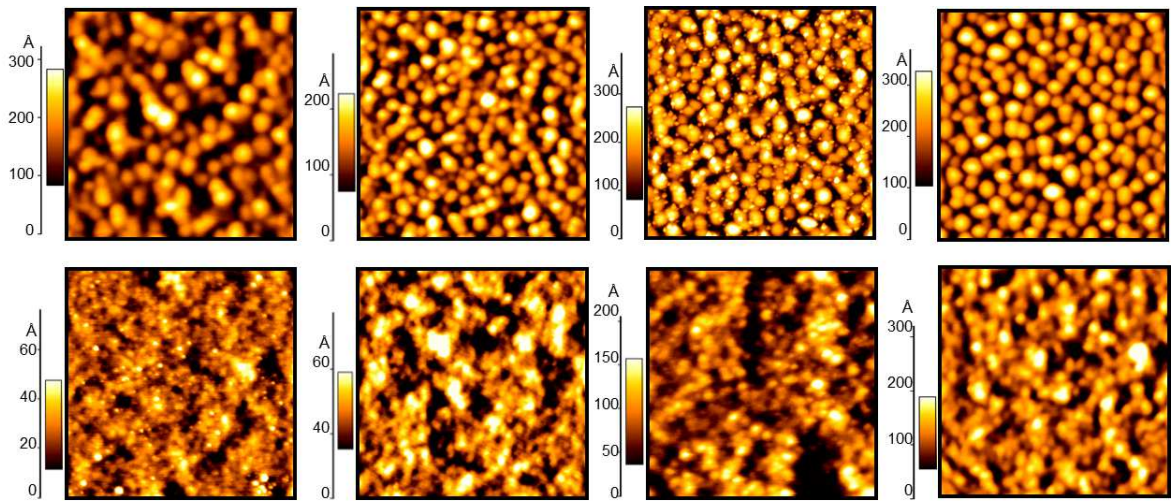

Figure 5.4: *AFM topography images of PTB7-Fx:$PC_{71}BM$ BHJ blend films prepared from chlorobenzene without (upper row) and with (bottom row) 3 vol% solvent additive DIO. The scan size for all images is 4×4 μm^2. From left to right, topography images are obtained from PTB7-F00:$PC_{71}BM$, PTB7-F40:$PC_{71}BM$, PTB7-F60:$PC_{71}BM$, and PTB7-F100:$PC_{71}BM$, respectively. Different color bars indicate the height variance among different samples.*

nm are randomly distributed in the polymer network for non-fluorinated PTB7:$PC_{71}BM$ blend film, whereas more densely packed $PC_{71}BM$ clusters with smaller size distribution are formed with increasing fluorine content. It is also observed that the order of the self-assembled $PC_{71}BM$ clusters gets strongly improved with introducing more fluorine atoms along the polymer backbone. The mechanism is suggested to be that with increasing fluorine content the volume of the each polymer chain decreases due to its less bulky side chains, which spare more space for fullerene to agglomerate for reaching the lowest thermal dynamic equilibrium of the whole film.[103]

After adding DIO, fullerenes clusters appear interrupted from the top view. Smaller $PC_{71}BM$ cluster diameters are thus seen in the bottom row of Figure 5.4, which is favourable for efficient charge separation. As $PC_{71}BM$ clusters are still vaguely visible in films including PTB7-F60 and PTB7-F100 in the last two images of Figure 5.4, it is concluded that the intermixing effect induced by DIO is much more pronounced for non-fluorinated blend films than for highly fluorinated films. Thus, it is questionable that the well accepted addition of 3 vol% DIO as solvent additive is the optimal amount for all PTB7-Fx:$PC_{71}BM$ solar cells without taking material properties such as molecular weight, polydispersity, and regioregularity into account. Moreover, for DIO containing samples, especially for films consisting of PTB7-F00 and PTB7-F40 the film roughness decreases dramatically as indicated by the height variance of each color bar.

In addition, power spectral density (PSD) spectra are extracted by applying radial average and Fourier transform over all topography images with different scan sizes and shown in Figure 5.6(b). Clearly, for as-spun blend films without DIO (four bottom curves) prominent peaks corresponding to a domain size of about 250 nm are observed. These peaks shift towards higher q region with increasing fluorine content, indicating that smaller domain sizes are formed on the film surface. The more and more sharp peaks imply the corresponding size distribution also decreases. For DIO containing blend films, the disappearance of these pronounced peaks is an indication of a better interpenetrating network with smaller domain sizes formed on the film surface. However, due to the limited statistics and the geometry of AFM measurements potential smaller structural sizes and the buried inner film structures cannot be accessed by PSD profiles.

In conclusion, optical microscopy reveals miscibility-driven $PC_{71}BM$ cluster formation, which is corroborated further by AFM measurements with much better resolution. For as-spun blend films without DIO, better ordered self-assembly $PC_{71}BM$ clusters with smaller size distribution is observed as a function of fluorine content; For DIO containing films, the big $PC_{71}BM$ clusters smear out generally due to better solubility of fullerene in DIO. But different degree of intermixing effect introduced by DIO is observed for PTB7-Fx with different amount of fluorine content.

5.3.2 Mesoscopic lateral structure

To access the nanomorphology of the inner films, GISAXS measurements are employed to resolve inner film structure size down to nanometer length scale with excellent statistics. [107, 108] Two dominant features including the prominent side maxima at the Yoneda peak area and inclined intensity stripes under different angles for the as-spun blend films as marked inside the red outlines are observed from the two dimendional scattering data shown in Figure 5.5.[70] Similar inclined stripes scattering patterns are observed from channel structured P3HT by Meier et al., thus the inclined stripes are suggested to be caused by the well-ordered self-assembly $PC_{71}BM$ clusters in the film.[109] With increasing fluorine content, the inclined stripes get more pronounced, indicating the long-range cluster correlation inside the film get better ordered, agreeing with previous AFM topography images shown in Figure 5.4. For those films made of solvent mixture CB:DIO these well-ordered structures get suppressed, evident by the disappearance of those stripes as expected.

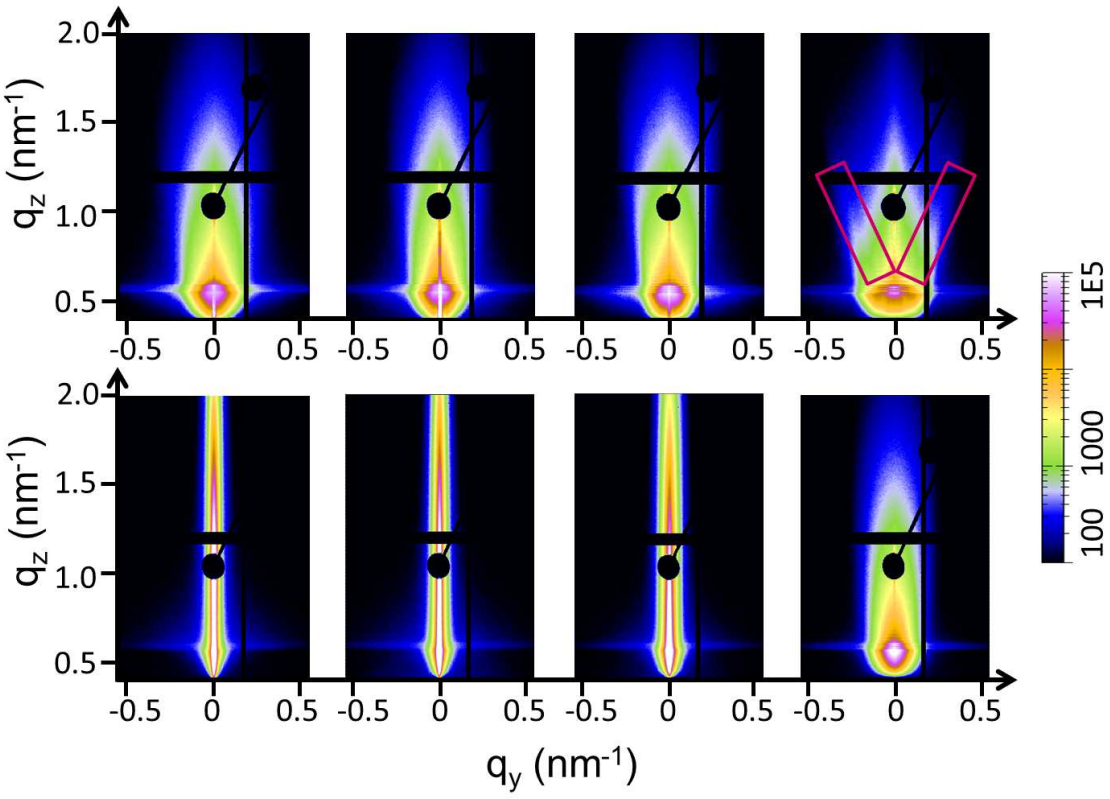

Figure 5.5: *2D GISAXS scattering data of PTB7-Fx:$PC_{71}BM$ BHJ blend films prepared from chlorobenzene without (upper row) and with (bottom row) 3 vol% solvent additive DIO. From left to right, GISAXS images are obtained from PTB7-F00:$PC_{71}BM$, PTB7-F40:$PC_{71}BM$, PTB7-F60:$PC_{71}BM$, and PTB7-F100:$PC_{71}BM$, respectively. Inside the red rectangle box, the scattering feature of inclined stripes explained in the text are particulary pointed out.*

To further obtain a quantitative evaluation of the 2D scattering data, horizontal line cuts at Yoneda peak position of PCBM are performed for all the samples. The corresponding cuts are plotted as a function of the scattering vector $\vec{q}$ as presented in Figure 5.6(a). As introduced in section 3.2.4, to model the obtained horizontal line cuts, the local monodisperse approximation (1D paracrystal model) with multi-length scale spheres as the basic form within the frame of DWBA is in use. As a result, the most prominent domain sizes in the film are extracted. For as-spun samples (bottom four curves in Figure 5.6(a)), the presence of multiple shoulders at different q_y positions is indicative of multiple length scales of the inner film.

Basically, two items form factors and structure factors are included for modelling the horizontal line cuts. Form factor describes the domain size and structure factor repre-

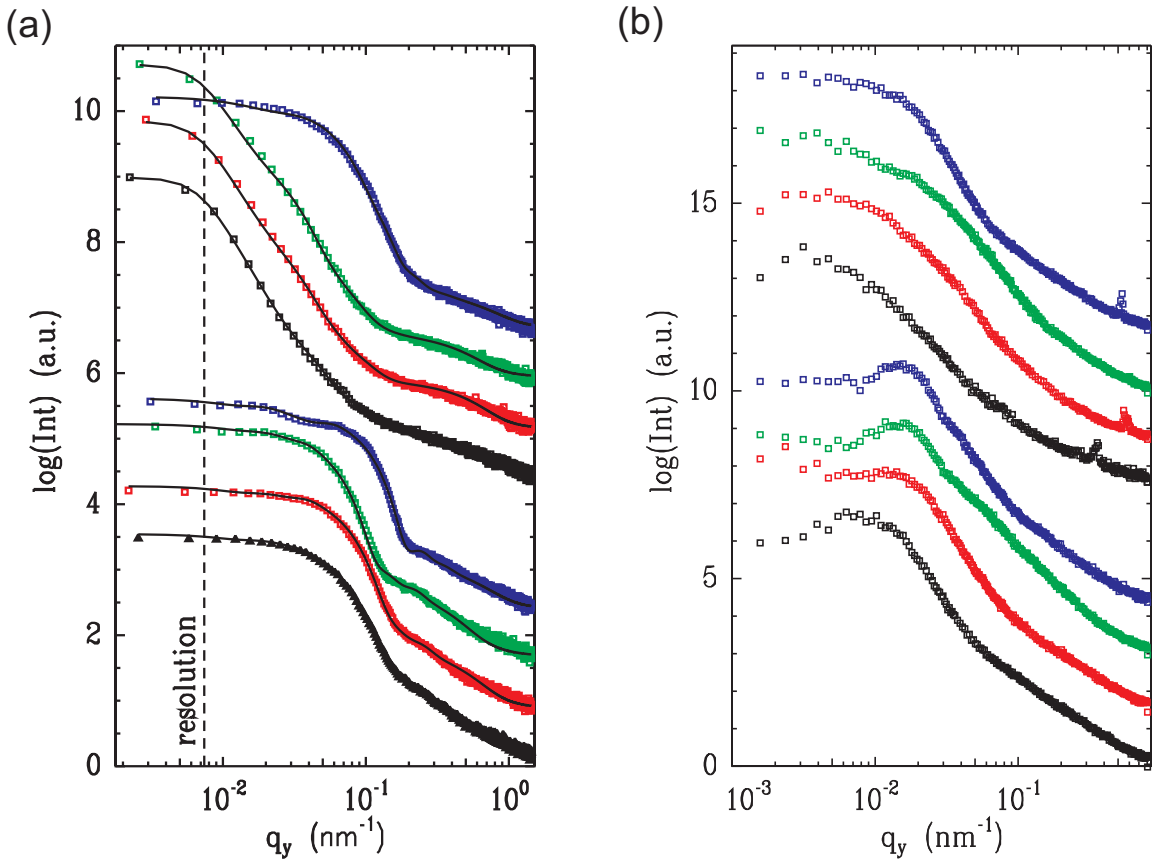

Figure 5.6: *(a) The horizontal cuts of 2D GISAXS data (open square) and corresponding modelling (solid lines) and (b) power spectrum density function extracted from AFM are presented. The intensity is plotted as a function of the vector $\vec{q_y}$ in reciprocal space. The bottom four curves are obtained from PTB7-Fx:$PC_{71}BM$ without solvent additive DIO, and the top four are obtained from PTB7-Fx:$PC_{71}BM$ with DIO.*

sents for the domain distance. However, only form factor dominate the overall modelling process, hence, the change of form factor is mostly correlated with the altered efficiency of the corresponding solar cells.

The extracted domain sizes of PTB7-Fx:$PC_{71}BM$ BHJ films without and with DIO are summarized in Table 5.2. As mentioned shortly before, multiple length scales is expected inside the blend films. Three extracted dominate domain sizes of around 650 nm, 250 nm, and 25 nm confirm the existence of the multiple length scales. The intermediate domain size R_2 is associated with aggregated $PC_{71}BM$ clusters, which is comparable with the film surface structure extracted from the PSD spectra of AFM measurements at around 250 nm. Among three prominent domain sizes, despite of the fact that domain sizes R_1 and R_2 are observed to change dramatically as a function of fluorine content as shown in Table 5.2, only the smallest domain size R_3 is expected to account for the efficiency variance as

sample	domain 1 [nm]		domain 2 [nm]		domain 3 [nm]	
	R_1	D_1	R_2	D_2	R_3	D_3
PTB7-F00:$PC_{71}BM$	650	1450	230	1080	35	220
PTB7-F40:$PC_{71}BM$	650	1450	245	1080	25	220
PTB7-F60:$PC_{71}BM$	650	1450	330	1100	30	250
PTB7-F100:$PC_{71}BM$	570	1500	215	760	20	160
PTB7-F00:$PC_{71}BM$:DIO	400	800	150	580	25	120
PTB7-F40:$PC_{71}BM$:DIO	575	800	180	450	24	100
PTB7-F60:$PC_{71}BM$:DIO	525	800	180	550	20	150
PTB7-F100:$PC_{71}BM$:DIO	430	750	225	550	15	120

Table 5.2: *Most prominent domain radius of PTB7-Fx:$PC_{71}BM$ films prepared from chlorobenzene without and with 3 vol% solvent additive DIO extracted from GISAXS measurements.*

it coincides with the length scale of the exciton diffusion length of organic photovoltaics. It is observed that for all the PTB7-Fx:$PC_{71}BM$ films spin-coated from CB R_3 decreases in size from 35 nm down to 20 nm with increasing the fluorination degree from 0 to 100. Similar decreasing trend is also observed for PTB7-Fx:$PC_{71}BM$ films spin-coated from the solvent mixture CB:DIO. Such shrink in domain size R_3 can partially explain the improved efficiency of the corresponding solar cells, that is, smaller domain sizes give rise to more interfaces between PTB7 and $PC_{71}BM$, and thus higher charge dissociation and higher efficiency are achieved via this better intermixed morphology.

In summary, for both as-spun and DIO containing blend films, three prominent structures are extracted from the 1D paracrystal model. A shrink in the most influential domain size R_3 as a function of fluorine content is observed. Moreover, it is noticed that the inner film morphology is not necessarily the same as the film surface morphology. As is shown in present work, a rather intermixed morphology inside the film is detected by scattering technique, whereas a phase separated morphology with large domain sizes is observed on the sample surface from AFM images.

5.3.3 Molecular order and crystallinity

For polymer:fullerene BHJ system, besides that the fullerene tends to agglomerate and crystallize as observed from previous optical microscopy and AFM images, the polymer

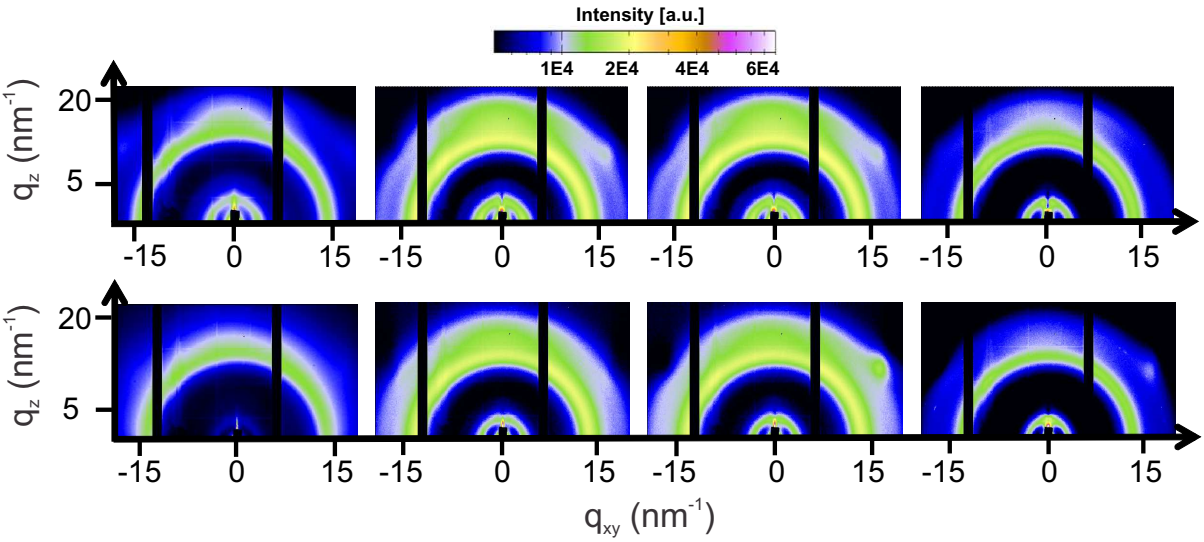

Figure 5.7: *2D GIWAXS scattering data of PTB7-Fx:$PC_{71}BM$ BHJ blend films prepared from chlorobenzene without (upper row) and with (bottom row) 3 vol% solvent additive DIO. From left to right, GIWAXS data are obtained from PTB7-F00:$PC_{71}BM$, PTB7-F40:$PC_{71}BM$, PTB7-F60:$PC_{71}BM$, and PTB7-F100:$PC_{71}BM$, respectively.*

also has the potential to form crystalline domains. To access information on crystallinity of PTB7, GIWAXS measurements are performed since the information about molecular orientation, intermolecular spacing and crystal size of the polymer within BHJ system are of utmost importance for the properties of organic photovoltaics. All the 2D GIWAXS data of PTB7-Fx:$PC_{71}BM$ films made of CB without (top row) and with (bottom row) 3 vol% solvent additive DIO recorded directly by the 2D detectors are presented in Figure 5.7.

A further quantitative evaluation of the GIWAXS data is realized by performing both horizontal and vertical sector integrals from the 2D GIWAXS images as shown in Figure 5.8(a) and (b) (scattering data obtained from blend films PTB7-F100:$PC_{71}BM$ with DIO). All the peaks are consequently fitted with Gaussian function to extract lattice constant and crystal sizes with the influence of fluorine as well as DIO. In total, for all samples three separated Bragg peaks are observed from horizontal cuts (Figure 5.8(c)), and a convoluted one attributed by several Bragg peaks from the higher q range of vertical cuts (Figure 5.8(d)).

For better comparison the corresponding horizontal and vertical cuts from both as-spun and DIO containing samples are normalized and plotted in Figure 5.9. For horizontal cuts in Figure 5.9(a), the prominent peaks at low q region (0.34 Å) for all four polymers correspond to the periodic backbone spacing along (100) direction. The lowest peak intensity of (100) Bragg diffraction peak is observed for PTB7-F00, implying the lowest

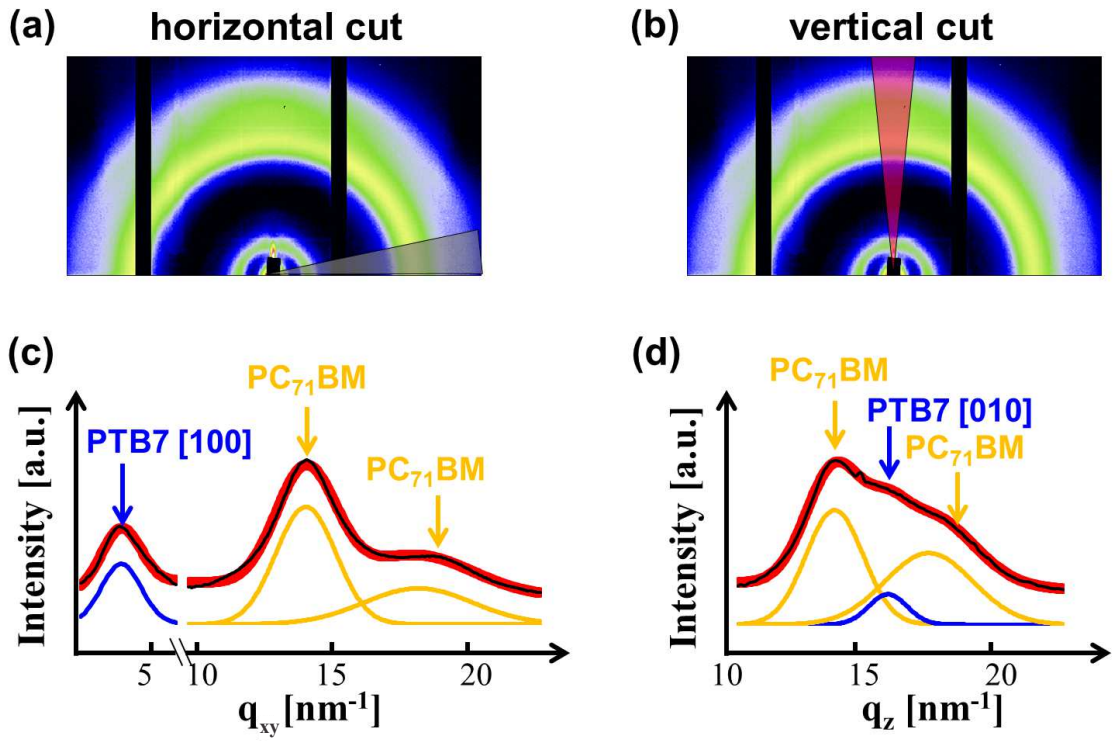

Figure 5.8: *Schematic presentation of 2D GIWAXS images obtained from PTB7-F100:$PC_{71}BM$ films (a) without and (b) with 3 vol% solvent additive DIO. A representative fit with Gaussian function used for (c) horizontal and (d) vertical cuts in the present investigation, respectively.*

crystallinity is found for non-fluorinated polymer PTB7-F00 compared with other polymers PTB7-Fx. Interesting changes occur to the backbone spacing: it increases 8 Å for all four polymers simultaneously after adding DIO. The possible scenario is that with the assist of DIO, $PC_{71}BM$ molecules have better mobility and diffuse into the polymer backbone, resulting in an expansion of the lattice constant by a level of its own diameter.[74] Although moderate shift of the (100) peak position is observed for polymers with varied fluorine content, the change along the (010) $\pi - \pi$ stacking direction is considered to be mainly responsible for the different device performances due to much higher charge transport rate along this $\pi - \pi$ stacking direction.

For both horizontal and vertical cuts, Bragg peaks arising from $PC_{71}BM$ seen as isotropic rings in 2D images (in Figure 5.7) locate at q_{xy} = 0.65, 1.30, 1.95 $Å^{-1}$. Each Bragg peak corresponds to (100) and correlated higher order d-spacing of 9.66 Å, 4.8 Å, and 3.22 Å, respectively.[74] Through a careful comparison of horizontal and vertical cuts at high q region, it is easily concluded that not only PCBM but also PTB7 contributes

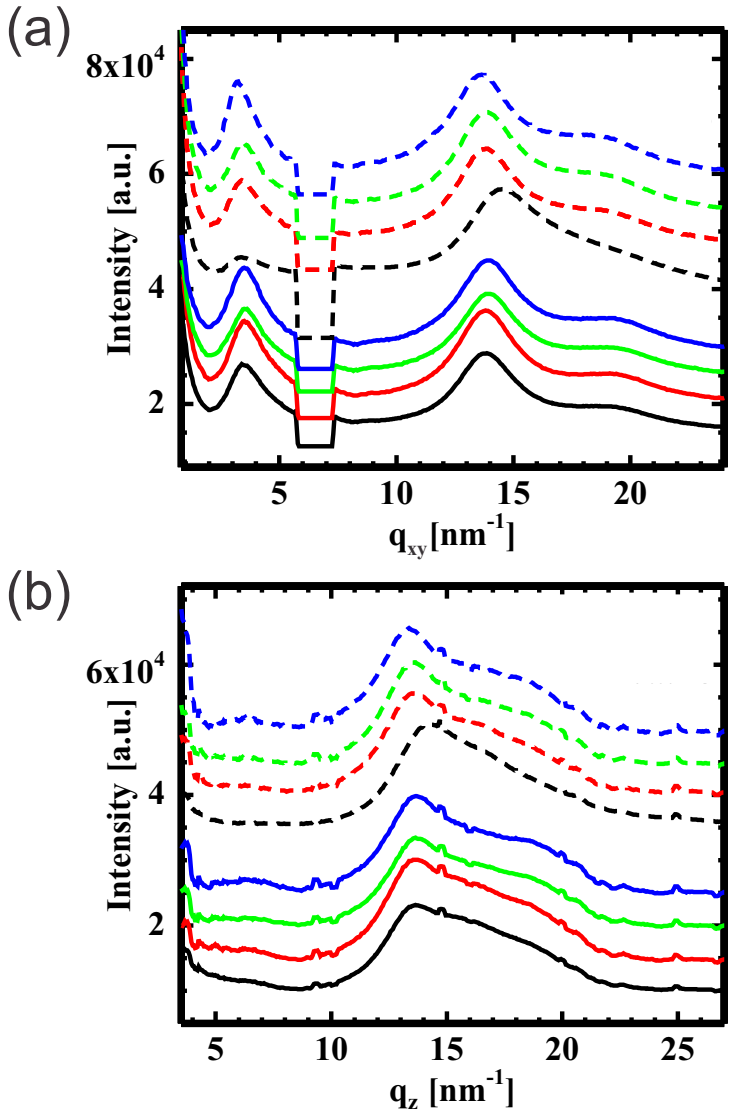

Figure 5.9: *(a) Horizontal and (b) vertical sector integrals of the 2D GIWAXS data of PTB7-Fx:$PC_{71}BM$ films made of chlorobenzene without (solid lines) and with (dash lines) 3 vol% solvent additive DIO. PTB7-F00, PTB7-F40, PTB7-F60, PTB7-F100 are indicated by black, red, green, and blue color, respectively.*

to the convoluted multiple peak in vertical cuts. The scattering signal at about 1.7 $Å^{-1}$ from vertical cuts for all four polymers is associated with the typical $\pi - \pi$ stacking distance of conjugated polymer backbones (3.7-3.9 Å). This feature particularly verifies that PTB7 tends to form face-on orientation, which agrees with other previous results on the copolymer PTB series.[74, 95] As compared with the PCBM diffusion into (100) direction, no PCBM is supposed to diffuse into the (010) $\pi - \pi$ stacking direction due to the diameter of $PC_{71}BM$ (10 Å) is much bigger than this typical $\pi - \pi$ stacking spacing of 3.8 Å.[74, 110, 111] For the prototypical P3HT:PCBM BHJ system, Treat et al. and Kohn

sample	lattice constant [nm]		crystal size [nm]	
	(100) h	(010) v	(100) h	(010) v
PTB7-F00:$PC_{71}BM$	1.82	0.39	n.a.	3.18
PTB7-F40:$PC_{71}BM$	1.80	0.39	n.a.	3.25
PTB7-F60:$PC_{71}BM$	1.78	0.39	n.a.	3.57
PTB7-F100:$PC_{71}BM$	1.80	0.38	n.a.	3.59
PTB7-F00:$PC_{71}BM$:DIO	1.89	0.37	n.a.	3.28
PTB7-F40:$PC_{71}BM$:DIO	1.88	0.39	n.a.	3.43
PTB7-F60:$PC_{71}BM$:DIO	1.85	0.39	n.a.	3.81
PTB7-F100:$PC_{71}BM$:DIO	1.93	0.39	n.a.	3.85

Table 5.3: *Lattice constant and crystal size of PTB7-Fx:$PC_{71}BM$ films prepared from chlorobenzene without and with 3 vol% solvent additive DIO extracted from GIWAXS measurements.*

et al. reported that PCBM molecules only tend to diffuse into the amorphous region of P3HT.[112, 113]

As explained above, one diffraction peak from PTB7 and two diffraction peaks from PCBM are identified to form the multiple peaks at high q region in the vertical cuts. GIWAXS measurement on neat PTB7 films (see section 6.1.2) can also provide solid proof for this conclusion. As a consequence, three distinct Gaussian functions as depicted in Figure 5.8(d) are used to fit the multiple peaks and further resolve the crystal size of each material, especially for PTB7. In contrast, a previous investiagtion done by Chen et al. on PTB7:$PC_{61}BM$ system only assumed one (311) Bragg diffraction of $PC_{61}BM$ and $\pi - \pi$ stacking of PTB7.[75]

Since the crystal behaviour along $\pi - \pi$ stacking dominates the charge transport of the whole film, information of the nanocrystal size along (010) direction is evaluated via scherrer equation and summarized in Table 5.3. For all four polymers without and with DIO, a general increase in crystal size is observed as a function of fluorine content. More specifically, roughly 8 $\pi-\pi$ stacked copolymer chains for PTB7-F00 increases up to 9 $\pi-\pi$ stacking chains for PTB7-F100 for as-spun blend films, whereas a change from 9 to 10 $\pi-\pi$ stacked copolymer chains is observed for DIO containing blend films. The slight increase in nanocrystal size with increasing fluorine content could, partially help to improve the solar cell efficiency. However, it cannot be the main reason for the significant difference observed for the device performances, especially considering the low level of crystallinity

for PTB7:$PC_{71}BM$ system. This is in agreement with the previous investigation that high crystallinity is not compulsory for high efficiency solar cell.[74]

In summary, regardless of the fluorination condition and use of DIO, no obvious changes occur to the molecular stacking distances, including both backbone and $\pi - \pi$ stacking distance for all the films. But the extracted crystal size increases with increasing fluorine content for both as-spun and DIO contaning samples.

5.3.4 Results

The effect of fluorination in manipulating the morphology of PTB7:$PC_{71}BM$ BHJ system is thoroughly investigated by a combination of imaging methods like optical microscopy, AFM and scattering techniques such as GISAXS and GIWAXS. Optical microscopy reveals miscibility-driven cluster formation of $PC_{71}BM$, which is further proved by AFM measurement with higher resolution. The order of $PC_{71}BM$ clusters depends on the degree of fluorination. Also it is observed that DIO help improve the miscibility between two components PTB7 and $PC_{71}BM$, and a better interpenetrating network is formed on the film surface from the comparison between the as-spun and DIO containing blend films. In addition, for DIO containing films smaller domain sizes is also formed inside the film, as probed by GISAXS measurements with excellent statistics. Moreover, higher amount of fluorine substitution on the polymer backbone alters the interaction with the fullerene in a beneficial way, resulting in smaller domain sizes as well in general. The crystal behaviours are accessed by GIWAXS measurement: neither the amount of fluorine nor solvent additive DIO leads to an obvious change in lattice constants, and only slightly bigger crystals are probed from higher fluorinated PTB7. Nevertheless, all the observed morplogical changes, including the smaller domain sizes, slightly bigger PTB7 crystal size as a function of fluorine content are only supposed to affect the J_{sc}, which is observed rather stable except for the devices made of PTB7-F100:$PC_{71}BM$. Hence, these differences do not fully justify the significant variance in the photovoltaic performance of the corresponding devices.

As for the device performance of PTB7-Fx:$PC_{71}BM$ solar cells prepared from solvent mixture chlorobenzene:DIO, the PCEs increase with introducing more electron-withdrawing fluorine atoms along the polymer backbone. The FF observed is similar for all the devices. J_{sc} remains rather similar (about 14 mA/cm^2) for PTB7-F00, F40, and F60, but it gets improved 25% (up to 17.44 mA/cm^2) for PTB7-F100. By correlating with the obtained morphological information, this improvement of J_{sc} could be associated with a comprehensive effect of more interface arising from smaller domain size inside the film, higher conductivity as a result of relatively bigger crystals for highly fluorinated

polymers. Eventually, V_{oc} is found to be the most influential parameter in determining the final device performance, which increases dramatically from PTB7-F00:$PC_{71}BM$ system to PTB7-F100:$PC_{71}BM$ system. In the present case, highest device performance is obtained from the film made of fully fluorinated polymer PTB7-F100 blended with $PC_{71}BM$, which is a result of the optimal energy level matching between two components, smallest domain sizes, and highest conductivity caused by the full flouination of polymer PTB7.

5.4 Summary

In general, the device performance is considered to be sensitive to the morphology of the active layer for polymer:fullerene BHJ systems. However, the systematic work on the PTB7-Fx:$PC_{71}BM$ system demonstrates that the film morphology and crystallinity do not change dramatically by incorporating different amount of fluorine along the polymer backbone. Only minor variances in domain size and molecular ordering were observed from sample to sample. Nevertheless, these variances do not effectively influence the charge absorption, dissociation, transport, as well as extraction, evident by rather similar J_{sc} and FF values for partially fluorinated polymers PTB7-Fx. An enhancement of J_{sc} is only observed for fully fluorinated polymer PTB7-F100. Therefore, it is concluded that the improved efficiency of the solar cells as a function of fluorination content is mainly ascribed to the enhanced V_{oc}, which is actually determined by the the intrinsic property of the used materials, that is, the difference between the HOMO level of the donor and the LUMO level of the acceptor material. This work provides a good example that one can adjust the HOMO and LUMO levels of the polymers by simply adjusting the incorporated amount of fluorine along the polymer backbone to optimize the device performance. Similar results are also demonstrated by other groups that introduction of fluorine atom into the thienothiophene submonomer could efficiently increase the V_{oc} or simultaneously improve the V_{oc} and morphology.[97, 98, 103, 114, 115, 116]

In conclusion, maximizing the V_{oc} in a low bandgap polymer is one constructive strategy towards high efficiency solar cells. It has been realized by applying strong electron-withdrawing atoms or groups to the backbone of the polymers to lower the HOMO level of polymers as evident by our work. Considering the LUMO level of the acceptor $PC_{71}BM$, it is still feasible to increase the V_{oc} by tuning the HOMO level of the polymers without sacrificing the J_{sc}.

Chapter 6

Solvent influence on neat PTB7 and PTB7:$PC_{71}BM$ BHJ system

Polymer:fullerene BHJ systems have made impressive progress in the past decades regarding the improvement on the solar cell efficiency. In this chapter, the solvent induced film morphology made of semi-conducting pure polymer PTB7 with 40% fluorinated thienothiophene units, namely PTB7-F40, and PTB7-F40:$PC_{71}BM$ BHJ system are investigated in section 6.1 and 6.2, respectively. The effect of using three different organic solvents chlorobenzene (CB), 1,2-dichlorobenzene (DB) and 1,2,4-trichlorobenzene (TB) as well as the processing additive 1,8-diiodooctane (DIO) on both systems is investigated. In particular, the efficiency/morphology relationship of the PTB7-F40:$PC_{71}BM$ BHJ system is addressed in section 6.2. Parts of the chapter have been published as an article in the Journal of Physical Chemistry B.[117]

6.1 Influence of solvent and additive on the morphology of PTB7 films

In spite of the great progress in promoting the efficiency of polymer BHJ solar cells, fundamental knowledge of the polymer domain formation, molecular orientation and crystal size in pure polymer films is yet to be understood. As one crucial component of organic solar cells, such basic insights can assist to improve the BHJ morphology. In this section, the influence on the film structure of the three commonly used organic solvents (CB, DB, TB) and the processing additive DIO is probed with grazing incidence small and wide angle X-ray scattering (GISAXS and GIWAXS). The molecular structure of the investigated polymer PTB7-F40 is shown in section 4.1.

6.1.1 Inner film structure probed by GISAXS

GISAXS measurements are applied on pure PTB7-F40 polymer thin films spin coated from the solvents CB, DB, and TB to gain morphology information of the whole film in the nanometer range. In Figure 6.1, the 2D GISAXS data of pure PTB7-F40 films made from different solvents without and with the additive DIO are presented.

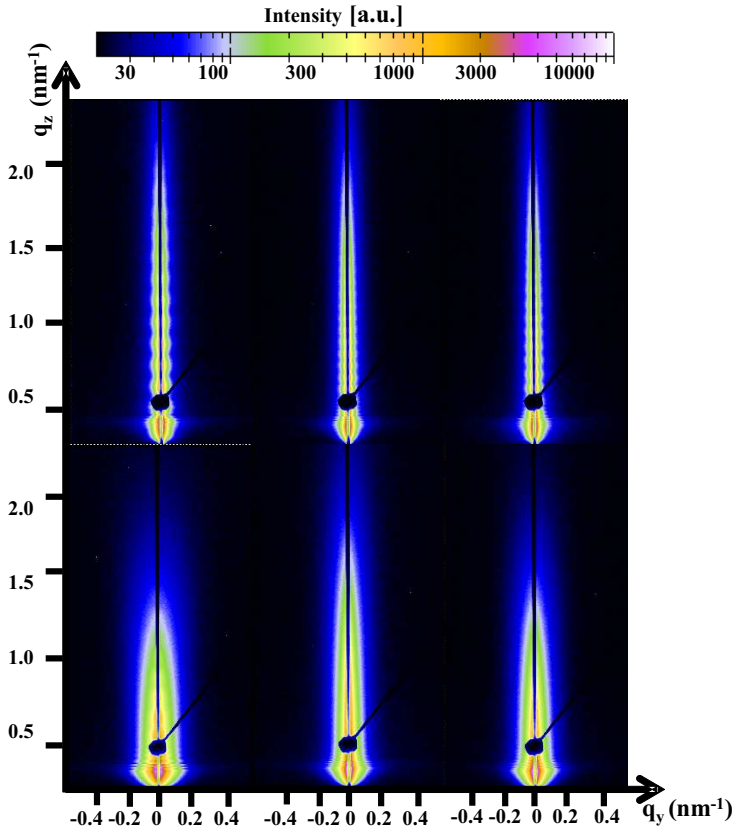

Figure 6.1: *2D GISAXS data of PTB7-F40 films prepared without (top row) and with (bottom row) 3 vol% solvent additive DIO. The used solvents are CB, DB, and TB (from left to right).*

For the data without additive DIO in the upper row of Figure 6.1, an oscillation of the scattered intensity in q_z direction is observed, regardless of the solvent being used. It originates from so called correlated roughness, that is a locally constant film thickness between two adjacent interfaces. This phenomenon was also observed for other polymer films as well as for whole organic solar cells.[66, 118] In this section, PTB7-F40 films follow the roughness of the underlying PEDOT:PSS film surface, which transmits part of roughness spectrum existing on the PEDOT:PSS film surface. To identify the threshold of the size of which can be replicated, namely, smallest replicated structure, off-centered

vertical cuts towards larger q_y values are performed. The intensity modulation of the off-centered vertical cuts gradually disappears towards larger q_y values. The smallest replicated structure is extracted by identifying the corresponding q_y value of the off-centered vertical cut, which does not show any intensity modulation. The calculated smallest replicated structure for the sample made from CB is 470 nm, and 555 nm for those made of DB and TB. Consequently, the roughness spectrum of the pure PTB7-F40 film is almost independent of the used solvent.

For the scattering data with the additive DIO in the bottom row of Figure 6.1, no pronounced intensity oscillations are observable. Thus the addition of DIO clearly changes the 2D GISAXS data, and therefore the vertical structure. To verify this, vertical cuts at $q_y = 0$ are performed and shown in Figure 6.2(a). The smallest replicated structures for DIO containing films made from CB, DB, and TB increase up to 758 nm, 1300 nm, and 825 nm, respectively. It is clear that the additive DIO affects the film formation and the intensity modulation arising from correlated roughness becomes less pronounced but is still observable. In the present investigation, DIO acts as a plasticizer, which still remains inside the polymer films after spin-coating due to its high boiling point (see section 4.1). The polymer films smoothens to reduce its free energy and therefore loses the roughness correlation because it is an energetically unfavorable correlation state. By comparison, it is concluded that the intensity oscillations arising from correlated roughness reduce due to adding the additive DIO, and these oscillations are independent of the used solvent.

Further insights regarding the inner film structure such as the lateral correlation, the structure and form size as well as the size distribution are obtained from the analysis of the horizontal line cuts of the 2D GISAXS data as shown in Figure 6.2(b). The horizontal line cuts of the 2D scattering data are taken at the critical angle of PTB7-F40, and fitted with a 1D paracrystal model within the frame of DWBA as explained in chapter 3.2.4. As seen in Figure 6.2(b), no prominent peaks in the nanometer regime are probed for all PTB7-F40 films made from solutions without DIO, implying no well defined structures are formed in these films. However, for the films made with the additive DIO, a prominent shoulder like feature is observed, indicating the formation of lateral defined structures. As extracted by a quantitative evaluation from the fits with a 1D paracrystal model, structures of 50 nm, 70 nm, and 75 nm are formed for DIO included films made from CB, DB and TB solutions. The polymer aggregation caused by the additive DIO can be explained by the low volatility of DIO compared with the host solvent. The formation of different inner film structure size agrees with the decreasing volatilities of the host solvents, as the boiling point of three solvents increases from CB (131°C) to DB (181°C) and TB (215°C), allowing more time for polymer chain aggregation. Similar result has also been reported by Lou et al. that the radius of PTB7 aggregates increased slightly from 34 Å to 37

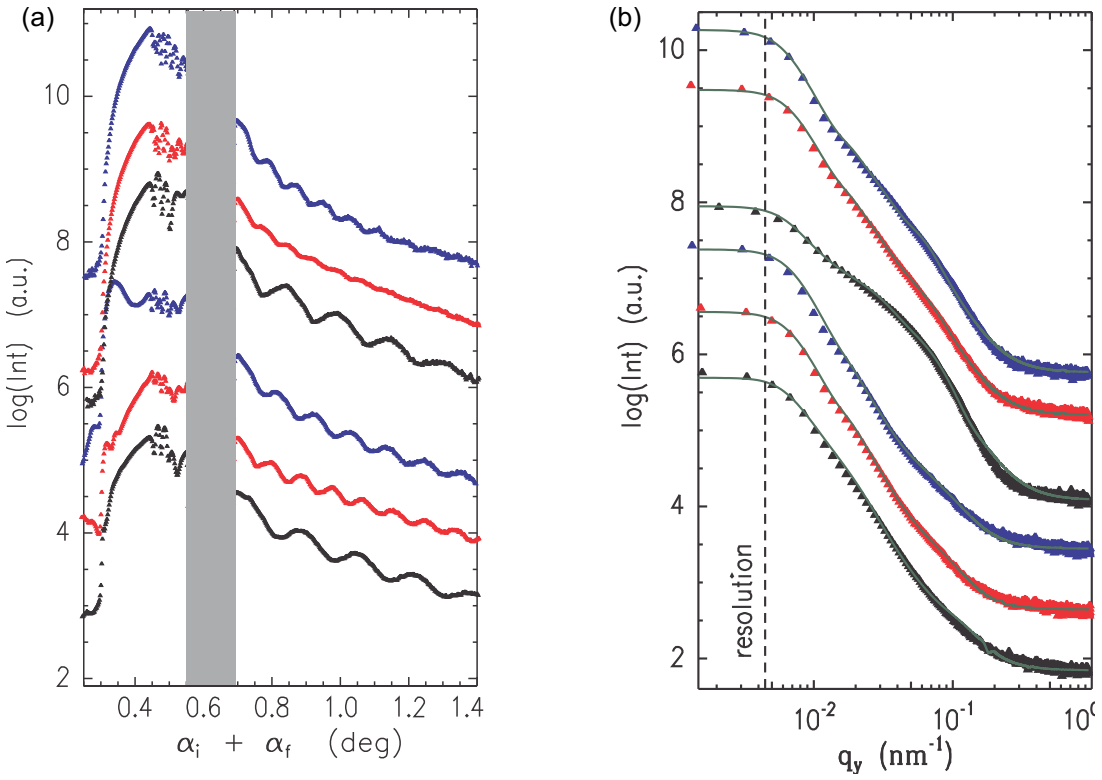

Figure 6.2: *(a) Vertical and (b) horizontal line cuts of 2D GISAXS data of PTB7-F40 films made of CB (black), DB (red), and TB (blue) without (bottom three curves) and with additive DIO (top three curves). The intensity is recorded as a function of the detector angle $\alpha_i + \alpha_f$ and the y component of the scattering vector q_y, respectively. The position of the specular beamstop is indicated by the grey box. The fits are shown by solid lines. All the curves are shifted in y direction for clarity.*

Å with the addition of DIO probed by SAXS measurments.[88]

6.1.2 Molecular order and crystallinity probed by GIWAXS

Followed by the inner film structural characterization, GIWAXS measurements are applied to obtain the film crystallinity information like molecular orientation, lattice constants, and the crystal size, which is related to the conductivity of the active layer and thereby the corresponding solar cell performance.

The 2D GIWAXS data of CB, DB and TB without and with the additive DIO are shown in Figure 6.3. Two features are clearly observed: the pronounced scattering intensity at high q values in vertical direction and at low q values in horizontal direction. In the vertical direction, the pronounced scattering intensity is ascribed to (010) Bragg peak

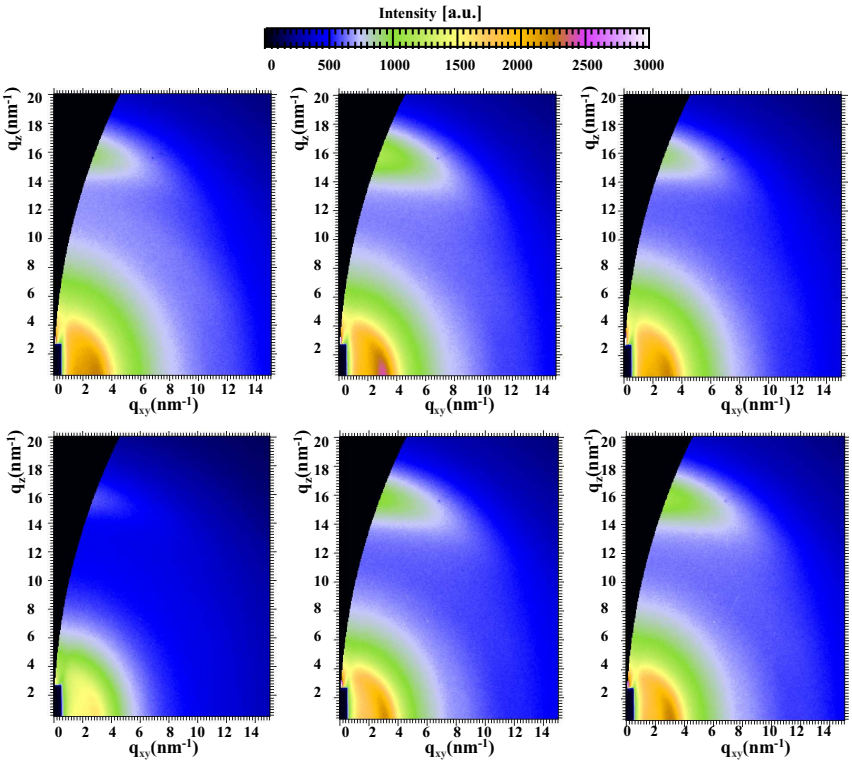

Figure 6.3: *2D GIWAXS data of PTB7-F40 films made of CB, DB, and TB (from left to right). In the upper row, data are obtained from samples without solvent additive DIO, and with the addition of DIO in the bottom row.*

originating from the polymer backbone $\pi - \pi$ stacking direction, in agreement with previous investigations on neat PTB7 polymer films made of DB by Hammond et al.[74] In the horizontal direction, polymer PTB7 backbone spacing in the alkyl side chain direction giving rise to a (100) Bragg peak. As detailed in section 2.3.4, GIWAXS measurements cannot access the full q-range due to the short SDD and fixed incident angle α_i as presented in Figure 6.3. However, based on the fact that neat PTB7 films have a very low gross crystallinity, as proved also by Hammond et al., we assume that a missing crystal population from the inaccessible region in Figure 6.3 is unlikely.[74, 76] Consequently, further quantitative evaluation is realized by the vertical and horizontal sector integrals of the original 2D GIWAXS data as shown in Figure 6.4.

From the horizontal cuts presented in figure 6.4(a), the (100) Bragg peak at a lower q_y value 3.3 nm^{-1} corresponds to the PTB7 backbone spacing as mentioned above, which is around 1.9 nm. The weak peak at q = 16 nm^{-1} originates from the $\pi - \pi$ stacking distance in the (010) direction. Compared with the horizontal cuts, the vertical cuts show less pronounced features at low q, which are caused by the beamstop instead of

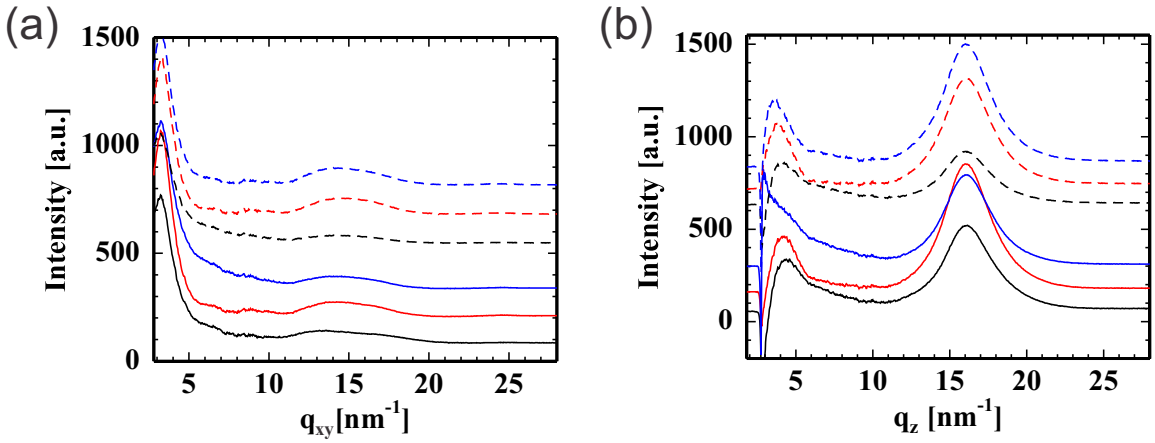

Figure 6.4: *(a) Horizontal and (b) vertical sector integrals of the 2D GIWAXS data of PTB7-F40 films prepared from CB (black), DB (red), and TB (blue) without (solid lines) or with (dashed lines) DIO. All the curves are shifted along the intensity axis for clarity.*

assigned (100) reflection like the horizontal cuts. The very strong (010) Bragg peaks at 16.5 nm^{-1} in vertical direction associating with the $\pi-\pi$ stacking alignment indicate that the prevailing crystallite orientation for PTB7-F40 films is the face-on orientation. This is in agreement with several other investigations on PTBx films.[74, 103]

From the peak intensity, for all the horizontal cuts it is also concluded that film crystallinity remains rather constant, regardless of the used solvent or the additive. In contrast, interesting changes are observed for the vertical cuts. Films made of different solvents consist of different crystallinity, and the amount of crystallinity changes with the effect of the additive DIO as seen by the modulated peak intensity.

By fitting all intensity peaks in the cuts with Gaussian functions as presented in

solvent	**lattice spacing [nm]**		**crystal size [nm]**	
	(100) h	(010) v	(100) h	(010) v
CB	1.97	0.39	4.84	2.04
DB	1.92	0.39	4,45	1.97
TB	1.96	0.39	5.12	2.05
CB:DIO	1.99	0.39	4.83	1.97
DB:DIO	1.89	0.39	4.48	1.82
TB:DIO	1.92	0.39	4.48	2.08

Table 6.1: *Lattice constant and crystal size of PTB7-F40 films prepared from CB, DB, and TB without and with DIO extracted from GIWAXS measurements.*

Figure 5.8 in chapter 5 and applying the Scherrer equation, changes in the crystal size are extracted as listed in Table 6.1. This method reveals only the lower limit of the crystal size due to the resoltuion of the setup, deviation of lattice constants and varied crystal size. Nevertheless, it is a reliable method for a qualitative comparison. For the investigated system, it is summerized that neither different solvents or the additive DIO affects the crystal size for all films. This observation is in agreement with Lou's investigation that the addition of DIO has a negligible influence on the PTB7 crystal size.[88]

6.1.3 Results

The morphology and crystallinity of PTB7-F40 films made of three common organic solvents CB, DB, and TB without and with the additive DIO are probed by grazing incidence scattering techniques. Regardless of the used solvent, roughness correlation with the underlying PEDOT:PSS film surface is observed. However, the inclusion of DIO reduces the signal of roughness correlation due to its low volatility, resulting in defined polymer aggregation, which is not observed for non-DIO containing samples. In addition, the smallest inner film strucure is extracted for films made of CB, which may explain the best device performance of the corresponding PTB7:PC_{71}BM solar cells shown in section 6.2. Moreover, the individual crystal sizes probed with GIWAXS measurements are not affected by either the selection of solvent or the additive. Nevertheless, the overall structure order in the films is solvent dependent, and the film made of CB exhibits surprisingly small overall crystallinity after the addition of DIO.

6.2 Influence of solvent and additive on the morphology of PTB7:PC_{71}BM films

For solution-processed solar cell devices, the significance of selecting the host solvent has been evident by many investigations.[119, 56, 120, 121] Our previous study on the P3HT:PC_{61}BM BHJ system also shows that using different organic solvents results into remarkably different film morphology, which is directly linked to the corresponding device performance.[52] Despite of several other studies on PTB7 system have been reported recently,[75] most of these investigations only focused on PTB7:PC_{61}BM BHJ system, thus higher efficient PTB7:PC_{71}BM BHJ system remains to be studied. In this study, the solvent-induced structure/property relationships of PTB7-F40:PC_{71}BM BHJ films are investigated. Moreover, the effect of the processing additive DIO on the morphology control for the same series of samples is also probed. Since the first successful application

of the processing additive in low-bandgap polymer solar cells by Peet et al., more attention has been put on this field, which appears to be another effective method to control film morphology.[87, 122, 123, 124] The photovoltaic performance of solar cells made of three different solvents CB, DB, and TB was firstly characterized. Then the influence of these three common organic solvents and solvent additive DIO on the morphology of PTB7-F40:$PC_{71}BM$ BHJ films was deliberately explored by the combination of direct imaging techniques like AFM, and sophisticated scattering methods such as GISAXS and GIWAXS, which allows for probing the representative length scales of the blend films. As a consequence, the efficiency variance introduced by the usage of different solvents is addressed. The molecular structures of the studied materials can be found in Figure 4.1.

6.2.1 Optical properties

To enable a comparison between the solar cell devices made of different solvents comparable, the initial solution concentration of each solvent is adjusted to obtain the same film thickness for all films made of different solvents, which can be quickly checked by absorption measurements. According to the Beer-Lambert law, one could easily control the film thickness by comparing the absorption spectrum of each film as explained in section 3.1.1. As shown in Figure 6.5, PTB7-F40:$PC_{71}BM$ BHJ films made from different solvents present similar absorption spectrum, indicating that a similar film thickness is achieved. Therefore, the difference of the solar cell efficiency must arise from the different film morphology. It is noticed that a deviation in absorption of the film made from CB:DIO occured in the high wavelength range between 750 nm and 1000 nm. With repetitive measurements for all the samples, it is ruled out that the absorption deviation is caused by misalignment of the sample. It is possibly ascribed to the special droplet morphology of the blend film made of CB:DIO formed on particular glass substrate as inserted in Figure 6.5, which is not observed for other films.

6.2.2 Solar cell performance

Based on similar film thickness of the active layers, the IV curves of PTB7-F40:$PC_{71}BM$ solar cells prepared from CB, DB, and TB without and with additive DIO are recorded and shown in Figure 6.6. The corresponding parameters, J_{sc}, V_{oc}, FF and power conversion efficiency η of the solar cell devices are listed in Table 6.2.

Obvious different device performance is obtained by using different solvents. It is observed that the introduction of the additive DIO clearly promotes the device efficiency for solar cells made of CB and DB. In addition, CB appears to be the best solvent for

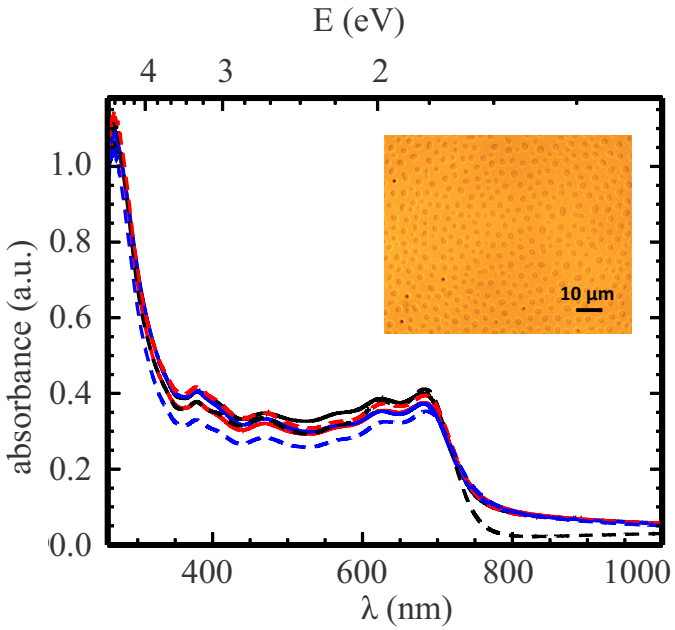

Figure 6.5: *Absorption spectrum of PTB7-F40:$PC_{71}BM$ solar cells prepared from CB (black), DB (red), and TB (blue) without (solid lines) or with (dashed lines) DIO. The absorption deviation for the black dashed line caused possibly by the special droplet morphology of the corresponding film as shown in the inserted optical image.*

PTB7:$PC_{71}BM$ solar cells, presenting a PCE of 4.32% when the additive DIO is used, which is in agreement with the efficiency characterization of PTB7 systems by Liang et al.[41] In contrast, Chen et al. reported relatively higher efficiency device is made from solvent DB.[75] The difference possibly arises from the different electron acceptor, as the former group uses $PC_{71}BM$ whereas Chen et al. selects $PC_{61}BM$. Based on the results proved by Troshin et al. that minor modification of the fullerenes would give dramatic

solvent	$\mathbf{J_{sc}}$ **(mA/cm^2)**	$\mathbf{V_{oc}}$ **(V)**	**FF (%)**	η **(%)**
CB	9.65	0.52	41.01	2.07
DB	6.75	0.44	44.58	1.32
TB	5.10	0.45	49.47	1.14
CB:DIO	16.06	0.53	50.95	4.32
DB:DIO	13.98	0.52	50.97	3.71
TB:DIO	4.18	0.47	39.28	0.77

Table 6.2: *Parameters of PTB7-F40:$PC_{71}BM$ solar cells prepared from CB, DB, and TB without and with DIO.*

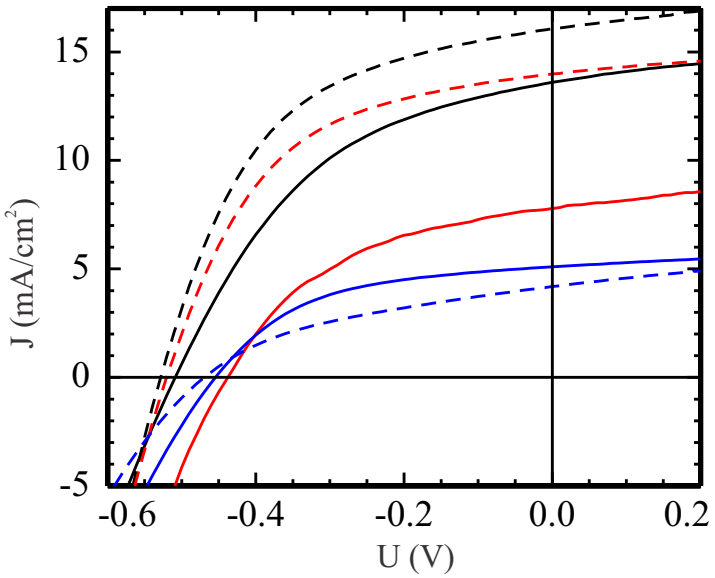

Figure 6.6: *Current-voltage characteristics of PTB7-F40:$PC_{71}BM$ solar cells prepared from CB (black), DB (red), and TB (blue) without (solid lines) and with (dashed lines) DIO. The measurements are performed under standard AM 1.5 spectrum with the illumination intensity 1000 W/m^2.*

change on the device efficiency due to the different solubility (e.g. the solubility of $PC_{61}BM$ and $PC_{71}BM$ are 50 mg/mL and 80 mg/mL in solvent chlorobenzene, respectively), it certainly demonstrates the urgency to thoroughly study PTB7-F40:$PC_{71}BM$ BHJ system. [125, 126] The different PCE induced by the selection of the solvents mainly lies in the different J_{sc}. In comparison, V_{oc} and FF remain relatively stable for different solar cell devices.

6.2.3 Film morphology

(a) Mesoscopic surface structure

In Figure 6.7 the optical microscopy images of PTB7:$PC_{71}BM$ BHJ films on PEDOT:PSS modified silicon substrates are presented. Homogeneous films are obtained for all films made from different solvents. Thus the high molecular weight polymer PTB7 is completely dissovled in all solvents with the assistance of heating as mentioned in chapter 4, which is one of the most crucial factors affecting the final device performance for particularly the PTB7-F40:$PC_{71}BM$ BHJ solar cells. For the film made from CB:DIO, the droplet structure (observed on the glass substrate) mentioned above is not observed in the presented optical microscopy image due to the usage of different substrates. No mor-

phological difference is visible with the resolution limit of optical microscopy. Thus, AFM measurements are applied to obtain topography images of the polymer thin films surface on the nanometer scale.

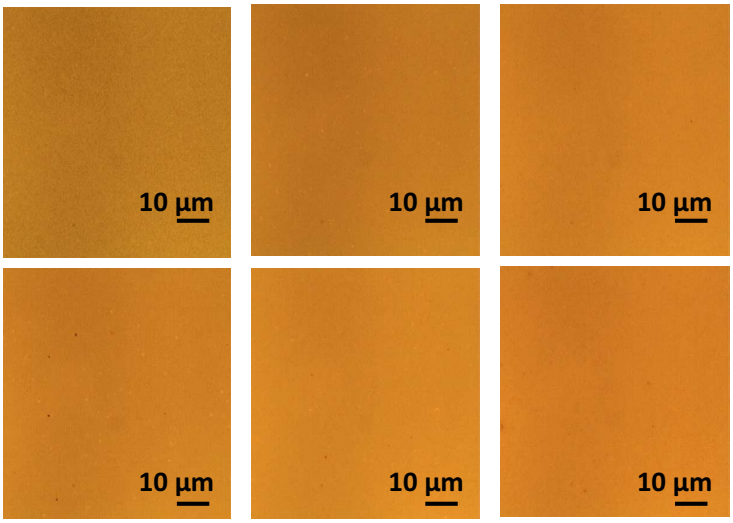

Figure 6.7: *Optical microscopy images of PTB7-F40:$PC_{71}BM$ films prepared from CB, DB, and TB (from left to right) without (in the upper row) and with DIO (in the bottom row).*

In Figure 6.8, AFM topography images of CB, DB, and TB without and with the additive DIO are shown. It has been reported from many studies on polymer:fullerene BHJ system that fullerene molecules tend to form clusters due to agglomeration and diffusion.[52, 121, 127] It is clearly observed that $PC_{71}BM$ tends to aggregate when the additive DIO is not included, agreeing with the results from other groups.[100, 128] Furthermore, the cluster size is solvent dependent. The size of $PC_{71}BM$ cluster decreases from around 250 nm to 100 nm as the boiling point of the host solvent increases. For those samples with solvent additive DIO, $PC_{71}BM$ clusters are not obviously visible as compared with those films without the DIO.

It is suggested that the formation of these fullerene clusters already takes place in the solution stage with different sizes in different host solvents, which is determined by the solubility of the fullerene in each solvent. As a result, TB shows the highest solubility for $PC_{71}BM$, whereas CB the lowest solubility, and therefore, biggest $PC_{71}BM$ clusters observed in case of CB. After the spin-coating step, the size of the fullerene cluster in the film stage preserves as that of the solution stage. However, when the additive DIO is included, as it can selectively dissolve $PC_{71}BM$, smaller $PC_{71}BM$ domains are created with the aid of DIO. $PC_{71}BM$ gets better distributed in PTB7 polymer network, leading to the formation of optimized domain size and more interfacial area between these two

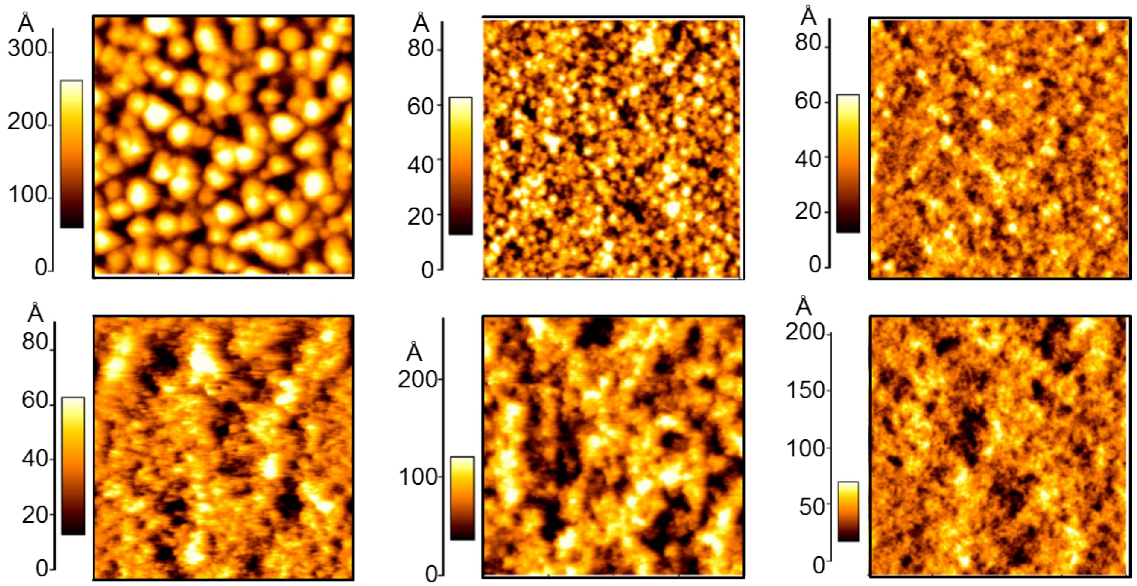

Figure 6.8: *AFM topography images of PTB7-F40:$PC_{71}BM$ films prepared from CB, DB, and TB (from left to right) without (in the upper row) and with DIO (in the bottom row). The scan size for all images is 2×2 μm^2. Different color bars indicate the height variance among different samples.*

components.[41, 95, 88] Accordingly, the charge separation probability and the final device efficiency get enhanced. Especially for the sample made from TB:DIO, the best intermixing surface morphology is observed. However, lowest efficiency is obtained as presented in table 6.2. The contradiction illustrates that one cannot purely correlate the surface morphology with the whole device property, and reliable statistical structure evaluations regarding the inner film morphology need to be further carried out. Moreover, although obvious PCBM clusters are observed for samples without DIO from topography images, it is risky to conclude that higher concentration of $PC_{71}BM$ on top of the film. To further confirm the existence of an enriched $PC_{71}BM$ layer, XRR measurements are performed.

In summary, the formation of the film surface morphology is a solubility and miscibility-driven process: for those films without DIO, the highest volatility of the solvent TB functions together with its best solubility for fullerene molecules, resulting in the smallest fullerene cluster size. Same mechanism also holds for the DIO included films, and DIO further assists to dissolve the fullerene clusters, therefore, better interpenetrating network of two components with even smaller length scales are observed. So far, only film surface morphology is probed. To access the inner film structure, e.g. the film lateral structure and vertical composition, X-ray scattering and X-ray reflectivity are applied.

(b) Mesoscopic lateral structure

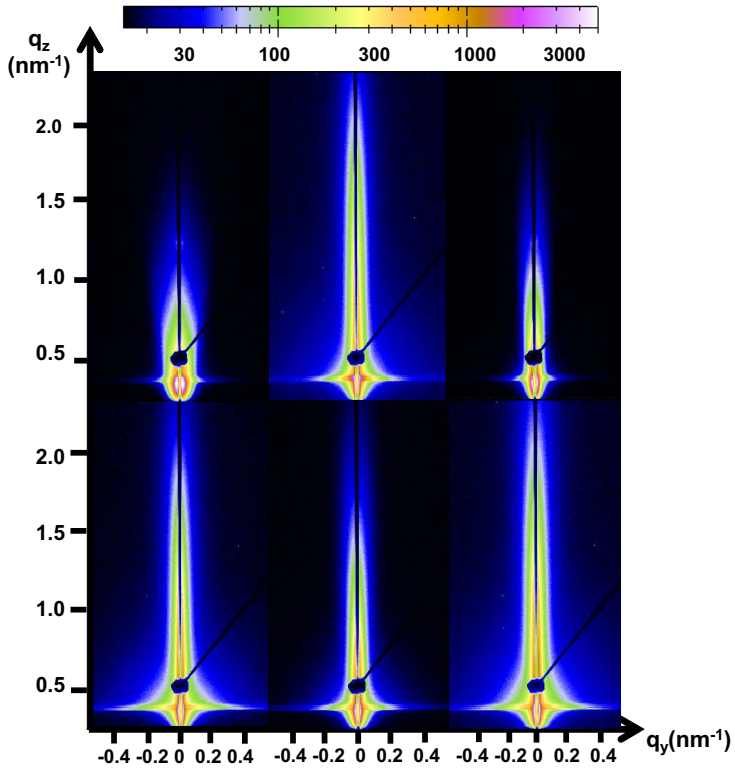

Figure 6.9: *2D GISAXS scattering data of PTB7-F40:$PC_{71}BM$ BHJ blend films prepared without (top row) and with solvent additive DIO (bottom row). The used solvents are CB, DB, and TB from left to right.*

In Figure 6.9, GISAXS scattering data of PTB7-F40:$PC_{71}BM$ BHJ blend films made of different solvents are displayed. As compared with the scattering data from pure PTB7-F40 films shown in Figure 6.1, no roughness correlation phenomenon can be observed due to the inclusion of $PC_{71}BM$ component. Furthermore, a much broader scattering signal towards higher q range along q_y direction is observed for all samples, especially for the three DIO added films, implying smaller domains are formed. In order to gain a reliable quantitative evaluation, precise analysis of horizontal horizontal line cuts are performed and fitted with 1D paracrystal model within the frame of DWBA.

The corresponding horizontal line cuts of GISAXS datas probing the inner film structure information are presented in Figure 6.10(a). For those samples containing solvent additive DIO, modulate peaks shift from low q_y to high q_y range as compared with non-additive films indicate that relatively larger $PC_{71}BM$ clusters disappear while smaller structures are formed. In order to gain a quantitative evaluation, all the horizontal line

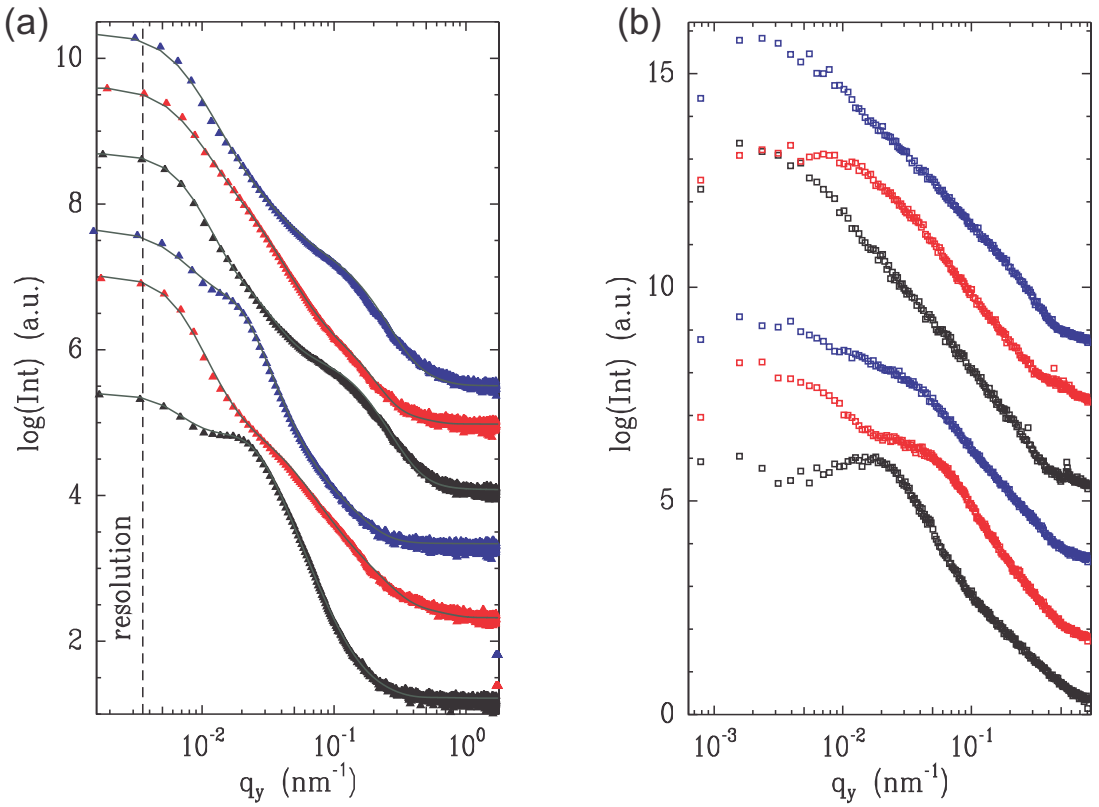

Figure 6.10: *(a) Horizontal line cuts of the 2D GISAXS data and (b) power spectrum density function calculated from AFM data. The intensity is plotted as a function of the scattering vector q_y in reciprocal space. Solid lines represent the fits with the 1D paracrystal model. The bottom three curves are PTB7-F40:$PC_{71}BM$ BHJ films made of CB (black), DB (red), and TB (blue) without the additive DIO, and the top three are with the additive DIO.*

cuts are fitted with 1D paracrystal model as described in section 3.2.4. The fitting parameters are summarized in Table 6.3 using three different form factors and structure factors. For the films made without DIO, average domain size R_1 in the range of few hundred nanometers decreases with increasing the boiling point of the host solvent. These results agree well with the trend revealed by AFM measurements which have shown that the aggregated $PC_{71}BM$ clusters form on the film surface. The solvent-dependent size formation is again attributed to the different solubility of $PC_{71}BM$ for each host solvent as explained above. The second domain size R_2 of several tens nanometers remains rather stable for all the films regardlesss of the used host solvent and additive. The smallest domain R_3 is fitted with domain size around 10 nm, which matches the exciton diffusion length as mentioned in the theory chapter. Hence, the evolvement of domain size R_3 is expected to strongly influence the device performance. By correlating the device performance with the extracted lateral structure sizes, the effect of DIO on the film morphology is clearly evident by the overall shrinked domain sizes (R_1, R_2, R_3). Moreover, the best solar cell

solvent	domain 1 [nm]		domain 2 [nm]		domain 3 [nm]	
	R_1	D_1	R_2	D_2	R_3	D_3
CB	320	650	60	180	30	120
DB	250	650	50	180	14	80
TB	230	600	75	150	13	50
CB:DIO	160	490	50	170	8	60
DB:DIO	170	500	65	200	8	100
TB:DIO	220	600	70	450	10	100

Table 6.3: *Extracted representative domain size information of PTB7-F40:$PC_{71}BM$ solar cells prepared from CB, DB, and TB without and with DIO.*

efficiency given by CB:DIO can be explained by the smallest inner domain structures as seen in Table 6.3. In addition, the inner film structure from horizontal line cuts of the 2D GISAXS data are compared with the film surface structure deduced from the power spectrum density function of AFM data (see Figure 6.10(b)). It is observed that the inner film structure for all the films (400 to 600 nm) is bigger than that of film surface (100 to 250 nm) by the identification of the corresponding q value of the peak center.

(c) Mesoscopic vertical structure

As introduced in section 3.2.3, XRR measurement is routinely used for the measurement of thickness, vertical material composition and roughness of thin films. The vertical profile is crucial for the performance of organic photovoltaic cells. Depending on the geometry of the whole solar cell, the possible formation of an enrichment layer in a wrong position, e.g. at the wrong electrode can act as an undesired blocking layer, which directly affects the charge transport and therefore the device performance. From XRR data shown in Figure 6.11, it is proved that thickness control by absorption is an effective method and the thickness of all films made of different solvents is about 115 nm. Film roughness decreases after adding the DIO except for the sample made from DB. In addition, enrichment layers can be observed for all the samples, which is presented in an alternative way as chemical composition profile converted from the refractive index profile. The chemical composition profiles for all the samples depicted with a gray scale model as shown in Figure 6.12.[129]

For the extensively studied model system P3HT:PCBM solar cells, Kumar et al. have demonstrated that an enhancement of the P3HT:PCBM device performance can be realized by the vertically modulated nanomorphology.[29] In analogy, the ideal vertical material composition for PTB7:$PC_{71}BM$ solar cells is suggested to be an ultra thin PTB7 layer

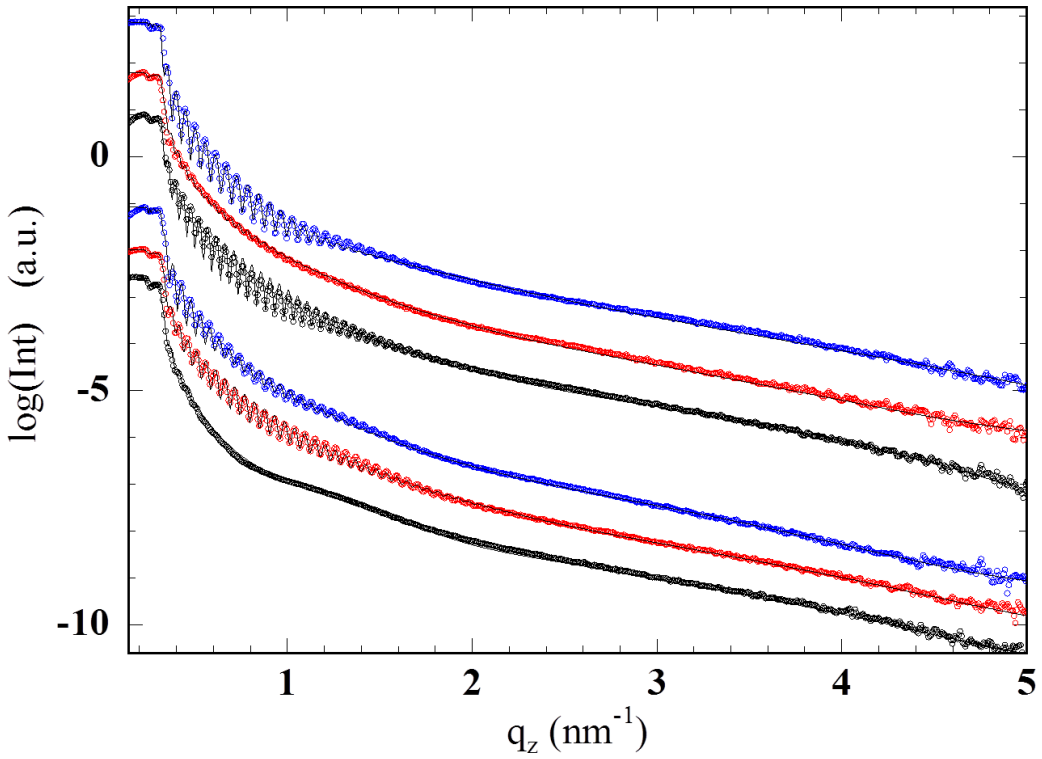

Figure 6.11: *Measured XRR data points with fits (solid line) of PTB7-F40:$PC_{71}BM$ films prepared from CB (black), DB (red), and TB (blue). For the bottom three curves, data are obtained from samples without solvent additive DIO, and top three ones are with the addition of DIO.*

at the bottom of the film, while a $PC_{71}BM$ layer close to the aluminum contact.[29, 130] However, it is reported by Hedley et al. that a thin PTB7-rich skin layer on top of the blend film is probed by the combination of several techniques (SEM, AFM and time-resolved photoluminescence).[128] In contrast, in the present investigation an enriched $PC_{71}BM$ layer is observed on top of the blend films. Additionally an enriched PTB7 layer at the bottom of all films is formed. The formation of such vertical material composition is caused by the different solubility of polymer PTB7 and $PC_{71}BM$ in the host solvent. For example, in case of CB it is 80 mg/mL for $PC_{71}BM$ and less than 10 mg/mL for PTB7.[125] As the solubility of $PC_{71}BM$ in CB, DB and TB is higher than that of PTB7, during the solvent evaporation process (spin-coating process), $PC_{71}BM$ with better solubility tends to form an enrichment layer at the film surface, while PTB7 slightly enriches at the bottom of the blend film. Such vertical composition with enrichment layers observed in this study are beneficial for the whole solar cells device: (1) The PTB7 enrichment layer can serve as a hole-transporting layer and PCBM enrichment layer as an electron-transporting layer to assist charge transport. (2) These enrichment layers are able to reduce the energy barrier by forming ohmic contacts, resulting in effective charge

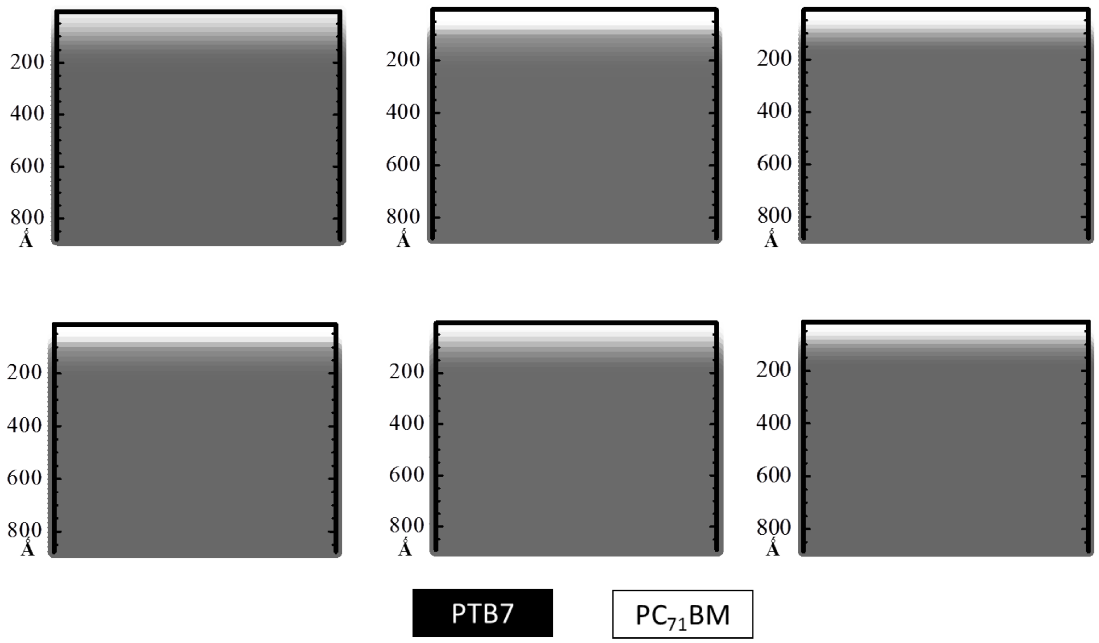

Figure 6.12: *The scattering length density profile of polymer blend PTB7-F40:$PC_{71}BM$ films prepared from CB, DB, and TB without (in the upper row) or with DIO (in the bottom row) extracted from fitting data of the XRR measurements. The pure black region indicates the pure PTB7 enrichment layer, pure white region indicates the pure $PC_{71}BM$ enrichment layer, and the gray region is the mixture of both materials. Note that the scale of the film thickness is the same for all the samples (around 115 nm).*

extraction. Nevertheless, the vertical profiles from the different solvents are rather similar, which cannot address the efficiency difference of different devices. To further assess details about the film crystallinity, GIWAXS measurements are employed.

(d) Molecular order and crystallinity

Charge transport as one important process is governed by the conductivity and crystallinity of the polymer. From the investigation of the pure PTB7-F40 films in section 6.1, it is summarized that neither solvent or solvent additive affects the film crystallinity. In this study, the crystallinity investigation on the PTB7-F40:$PC_{71}BM$ blend films is also performed by GIWAXS measurement. The corresponding GIWAXS data are presented in Figure 6.13. Several prominent scattering features are observed: arc-like signals arising from the random orientation of PCBM molecules, pronounced scattering intensity at low q_y (about 3.5 nm^{-1}) and high q_z (about 15 nm^{-1}) values. As shown in Figure 6.14, for both horizontal and vertical sector integrals, Bragg peaks from $PC_{71}BM$ are present at q

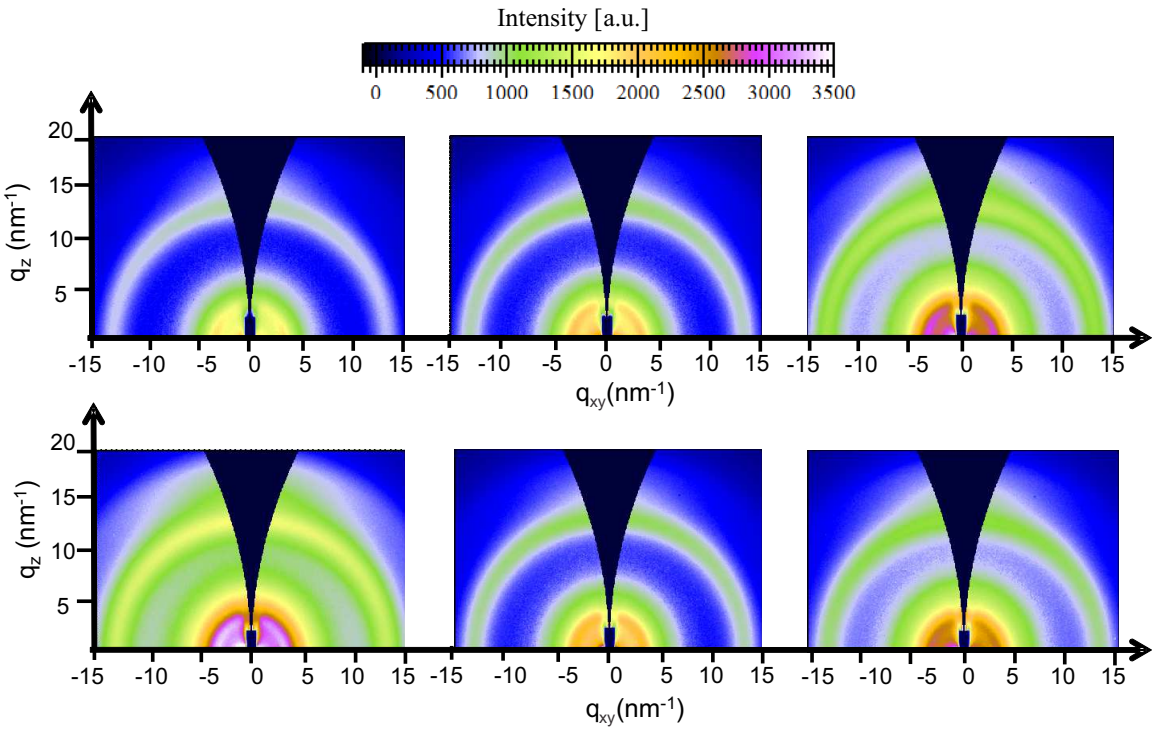

Figure 6.13: *2D GIWAXS data of PTB7-F40:$PC_{71}BM$ BHJ films made of CB, DB, and TB (from left to right). In the upper row, data are obtained from samples without solvent additive DIO, and with the addition of DIO in the bottom row.*

= 6.5 nm^{-1}, 13.3 nm^{-1}, 19 nm^{-1}. The Bragg peaks at a q value 3.3 nm^{-1} appearing in all the horizontal cuts in Figure 6.14(a) correspond to the (100) PTB7 backbone spacing, which has already been probed for pure PTB7-F40 films.[117] With careful comparison of the Bragg peaks in the higher q range between the horizontal and vertical cuts, it is easy to assign the multiple peaks in the q range of 12 nm^{-1} to 19 nm^{-1} in Figure 6.14(b), that is, two Bragg peaks from $PC_{71}BM$ at q values of 13.3 nm^{-1}, 19 nm^{-1}, and one Bragg peak arising from (010) PTB7 $\pi-\pi$ stacking distance. The details are explained in the previous chapter in Figure 5.8.

With a quantitative evaluation by fitting all the Bragg peaks with Gaussian functions as explained in the previous chapter in section 5.3.3, molecular stacking information is obtained by identifying the corresponding q value for each Bragg peak. However, both backbone spacing and $\pi-\pi$ stacking distance remain rather constant as shown in Table 6.4: The extracted backbone spacing along the (100) direction for all samples is 1.8±0.5 nm, whereas the $\pi-\pi$ stacking distance along (010) is 0.40±0.01 nm. Additionally, the crystal size is estimated with the Scherrer equation. It is observed that for samples made of CB and DB, crystal sizes along (010) direction slightly increase after introducing DIO, which

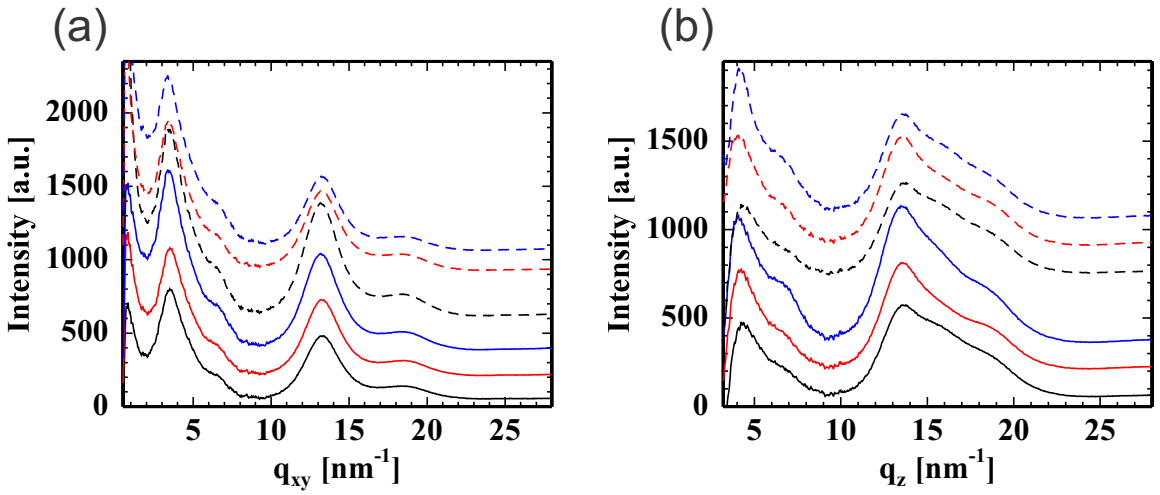

Figure 6.14: *(a) Horizontal and (b) vertical sector integrals of the 2D GIWAXS data of PTB7-F40:$PC_{71}BM$ BHJ films prepared from CB (black), DB (red), and TB (blue) without (solid lines) or with (dashed lines) DIO.*

can moderately assist charge transport within the blend films. For the samples made of TB, crystallinity even decreases for the additive DIO added film. The change in the crystallinity in (010) direction coincides with the corresponding solar cell performance listed in Table 6.2, which demonstrates the influence of the crystallinity on the overall device performance. However, this minor change in film crystallinity cannot be the main reason for the obvious efficiency variation. In conclusion, similar to the results obtained from pure PTB7-F40 films, the selection of solvents neither significantly changes the organization of PTB7 chains at a molecular level nor the nanocrystallite size of PTB7 or $PC_{71}BM$. This observation is in agreement with previous research on the same system by Chen et al.[75]

6.2.4 Results

As one of the newest low bandgap polymers PTB7, the influence of different solvents and the additive DIO on the molecular arrangement, mesoscopic and crystalline structure of BHJ PTB7-F40:$PC_{71}BM$ films is thoroughly studied. Based on a solution-processed technique, the selection of host solvent and the addition of an appropriate solvent additive have an impact on manipulating the nano-morphology of the PTB7-F40:$PC_{71}BM$ films. From this investigation, it shows that film thickness control via the simple comparison of absorption curves is an effective method, which is further confirmed by the XRR measurements. In addition, it is observed that the vertical composition of all films

solvent	lattice spacing [nm]		crystal size [nm]	
	(100) h	(010) v	(100) h	(010) v
CB	1.77	0.40	1.24	4.18
DB	1.76	0.41	1.18	4.23
TB	1.81	0.41	1.27	4.15
CB:DIO	1.80	0.41	1.26	4.31
DB:DIO	1.81	0.41	1.18	5.14
TB:DIO	1.85	0.39	1.17	3.27

Table 6.4: *Lattice constant and crystal size of PTB7-F40:$PC_{71}BM$ solar cells prepared from CB, DB, and TB without and with DIO extracted from GIWAXS measurements.*

are rather similar whereas film roughness decreases upon the addition of DIO. Moreover, much smaller domain sizes and better interpenetrating networks are formed for films with 3 vol% solvent additive DIO, which can greatly enhance the charge separation rate, and therefore improve the device performance. With wide angle X-ray scattering, it is observed that crystallinity within each film is correlated with the device performance. However, as the difference of the vertical film composition and crystallinity caused by different solvents and the additive are nearly neglectable, thus we ascribe the variation of corresponding device performance mainly into the difference of the lateral structure size probed by GISAXS measurement.

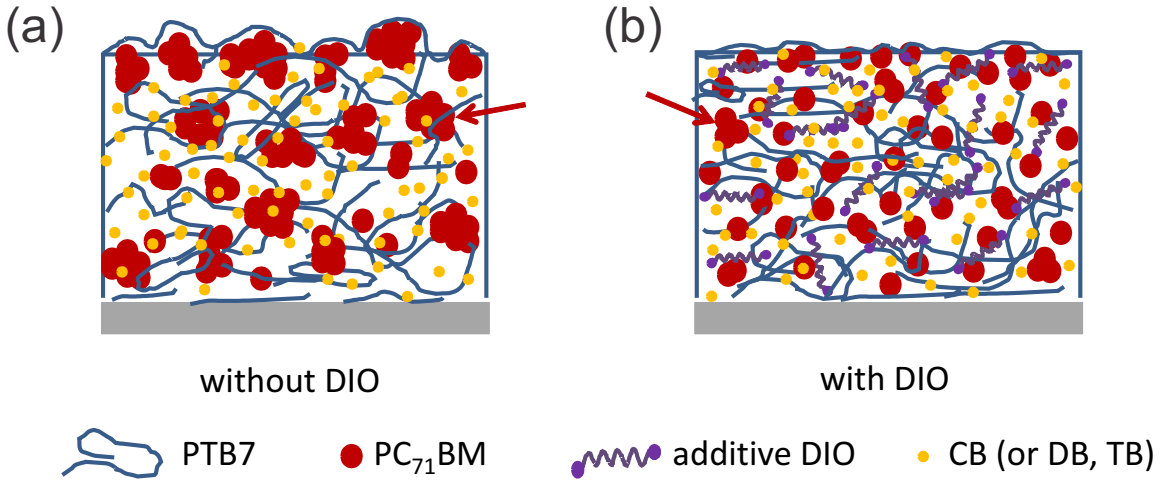

Figure 6.15: *Proposed morphology model of PTB7-F40:$PC_{71}BM$ BHJ films prepared from CB (DB, TB) (a) without and (b) with the processing additive DIO during spin-coating process. Blue wire: PTB7 polymer chain; Big red dots: $PC_{71}BM$; Purple chain with two dots: additive DIO molecules; Small orange dots: host solvent molecules.*

The corresponding film morphology for all the investigated films during spin-coating process is summarized in Figure 6.15. For the PTB7-F40:$PC_{71}BM$ BHJ films without the processing additive DIO, $PC_{71}BM$ clusters are formed and the size of the clusters is solvent dependent due to the different volatility of the host solvent. Films with relatively higher roughness are quantified. Upon the addition of DIO, big $PC_{71}BM$ clusters are selectively dissolved by DIO and diffuse into PTB7 network, forming a better interpenetrating morphology. In addition, a $PC_{71}BM$ enrichment layer is observed on the film surface for all the samples during the evaporation of DIO. Although moderate changes occur to the lattice constants and crystal size, the effect on photovoltaics performance becomes less influential or cancelled out by other factors in this case. Moreover, as proved by this investigation as well as that of others,[74] PTB7-F40:$PC_{71}BM$ is a typical low crystallinity system, therefore, information related to crystallinity is not included in the proposed model. The influence of different solvents on the film morphology mainly lies in the average domain size (PTB7 or $PC_{71}BM$ domains) as marked with red arrow in the proposed model.

6.3 Summary

By a simple switch of the host solvent, the morphology and crystallinity of pure PTB7 films and BHJ PTB7-F40:$PC_{71}BM$ films are affected, which leads to drastic change of the corresponding BHJ solar cell performance. It is suggested that the different morphologies introduced by different host solvents is mainly attributed to the miscibility and solubility difference between the polymer PTB7 and fullerene $PC_{71}BM$. According to the conclusion achieved by Troshin et al., the highest device performance is given by those material combinations where donor and acceptor components are of similar and sufficiently high solubility in the host solvent. CB is the solvent that allows PTB7 and $PC_{71}BM$ have similar high solubility in this study.[125] Consequently, for the solar cells made from CB, DB and TB, CB-based PTB7-F40:$PC_{71}BM$ films demonstrates the best PCE of 2.07%. For the solar cells made from CB:DIO, DB:DIO and TB:DIO, additional competition between the processing additive DIO with each host solvent (due to different volatility and solubility for $PC_{71}BM$) results in the proved enriched PCBM layer near the aluminum contact as well as better intermixed morphology with smaller length scales during the film drying process. With consideration of all effects, CB:DIO is proved to be the best host solvent mixture for PTB7-F40:$PC_{71}BM$ BHJ system mainly due to the smallest length scale through the whole active layer as probed by GISAXS measurement. This conclusion perfectly explains our first observation that the different PCE induced by the selection of the solvents mainly lies in the different J_{sc}.

In summary, as a solution-based new technology, a careful selection of solvent and the processing additive is of utmost importance. As a result, to further push up the PCE of organic photovoltaics, not only one could synthesize new polymers and fullerenes derivatives with balanced higher conductivity and lower bandgap, but also manipulate the nanomorphology formation by the smart selection of the solvent and possible additives.

Chapter 7

Solvent treatment enhanced efficiency for PTB7:$PC_{71}BM$ BHJ system

In order to obtain high efficiency polymer solar cells (PSCs), many approaches, such as the synthesis of new polymers, the judicious selection of host solvent, the introduction of solvent additives, post-production treatments, the optimization of device geometry and so on have been examined. In chapter 5, it is shown that synthesis of new low bandgap polymer is a promising method torwards higher efficient PSCs. In chapter 6, the impact of choosing the most suitable host solvent together with the solvent additive is clearly evident. In this chapter, taking the best performed polymer PTB7-F100 and most suitable host solvent chlorobenzene, a simple, environmentally friendly, and low cost method, namely, post treatment with green solvent (methanol) is introduced additionally and shown to be an effective post-treatment method to further improve the efficiency of polymer:fullerene BHJ solar cells.[102, 131, 132] The positive effect induced by methanol treatment for PTB7:$PC_{71}BM$ BHJ system is attributed to an increase in built-in voltage, decreased series resistance and reduced charge recombination reported by Zhou et al. recently.[102] Moreover, Ye et al. claimed that methanol treatment of the photoactive layer leaded to a shift of the vacuum level on the metal side of the device, thereby reducing the electron injection barrier at the organic/metal interface and resulting in an enhanced device performance.[92] However, so far all investigations regarding the influence of solvent treatment have only reported on the change of film surface, therefore, a potential change of the inner film morphology induced by the solvent treatment is mostly neglected. Moreover, all related researches only focused on the well-working solvent methanol for enhancing device efficiency in PTB7:PCBM polymer solar cells.[102, 131, 132] Investigations on the

impact of other alcohol solvents, such as ethanol, 2-propanol, and 1-butanol are still very limited.

In this chapter, a variety of alcohols for post-solvent treatment of the active layer of polymer solar cells, consisting of PTB7:PC_{71}BM in a BHJ geometry is employed to further optimize the final device efficiency. The effect of solvent treatment on the electronic properties of the solar cell devices and on the modification of the active layer morphology by comparing four alcohols (methanol, ethanol, 2-propanol, and 1-butanol treatment) are mainly examined. To date, this work for the first time systematically reports the effect of solvent treatment using these four alcohols. The main aim of the study is to track the trend of device efficiencies of the solar cells obtained after different solvent treatments rather than fabricating novel record PSCs by fully optimizing the devices. The film surface morphology of the pristine and solvent-treated polymer blend films is probed by atomic force microscopy (AFM), and inner film morphology is revealed by time of flight-grazing incidence small angle neutron scattering (TOF-GISANS). Using neutrons instead of X-rays has the particular advantage, that contrast condition can be better in systems relevant for PSCs.[133] As a consequence, the reason for the positive impact of solvent treatment on PTB7 based PSCs is presented, and the efficiency-morphology relationship is suggested. The results presented in this chapter have been submitted as an article to the journal Advanced Energy Materials.[134].

7.1 Solar cell performance

In total, more than 200 individual devices were fabricated and the corresponding IV curves were collected and analysed. It should be noticed that in present investigation the most simple device configuration consisting of indium tin oxide (ITO)/ poly(3,4-ethylenedioxythiophene): polystyrene sulfonate (PEDOT:PSS)/ PTB7:PC_{71}BM/ aluminum (Al) is selected to gain fundamental insights in the efficiency-morphology relationship. In other words, solar cells without a second hole-blocking layer or without optical spacer layers are fabricated and examined like those in previous chapters. Moreover, a relatively larger solar cell pixel size of 13 mm^2 is in use in this work as compared with 4.5 mm^2 in the investigation by Zhou et al.[102] Hence, it is reasonable to obtain slightly lower values of the device efficiency as compared to the reported results.

It is concluded that besides the recently published methanol treatment route, the use of other alcohols (like ethanol, 2-propanol, and 1-butanol treatment after the deposition of the photoactive layer) is also found to be able to improve the efficiency of PTB7:PC_{71}BM BHJ solar cells to certain extent. In Figure 7.1, the current-voltage characteristics (IV

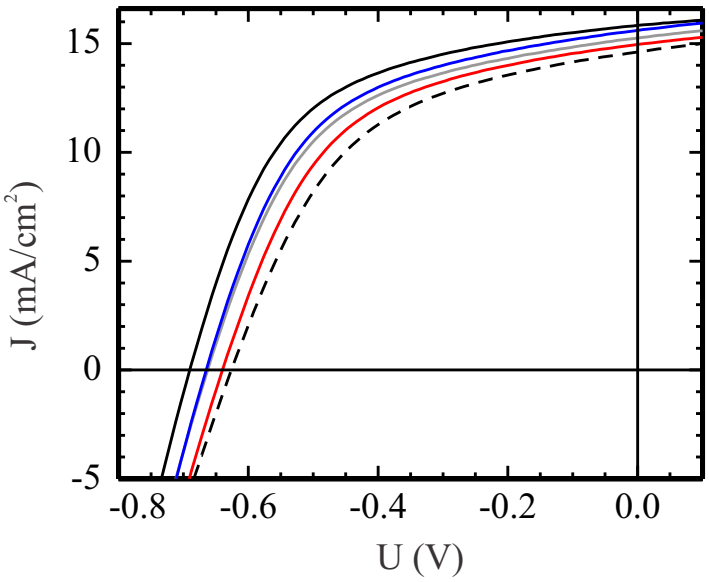

Figure 7.1: *IV curves of PTB7:$PC_{71}BM$ solar cells with different solvent treatments: reference solar cell (black dash line), with methanol treatment (black solid line), with ethanol treatment (red solid line), with 2-propanol treatment (gray solid line), and with 1-butanol treatment (blue solid line). The measurements are performed under standard spectrum AM 1.5 with the illumination intensity 1000 W/m^2.*

curves) of pristine PTB7:$PC_{71}BM$ BHJ solar cells and solvent treated solar cells using four different alcohols are shown. It can be observed that a simultaneous improvement of the short-circuit current J_{sc}, the open-circuit voltage V_{oc}, and the fill factor FF are obtained by these alcohol solvent treatments. However, the efficiency improvement does not exhibit a simple relationship with the used alcohols' properties, such as the number of carbon atoms or the vapor pressure of the alcohol solvents. In general, the highest efficiency is obtained from samples after methanol treatment, whereas the ethanol treatment gives rise to the most moderate enhancement of the device performance.

In order to have a quantitative comparison, the corresponding cell parameters J_{sc}, V_{oc}, and FF are evaluated and listed in Table 7.1. Considering only the device performance, the PCE of the pristine polymer solar cells is 4.6%, and it increases up to a maximum 6% for methanol treated devices. As for solar cell devices with 2-propanol and 1-butanol treatment, the PCE improves up to 5.32% and 5.52%, respectively. The efficiency enhancement for ethanol treated devices is lowest, and the resulting efficiency only achieves 5%. Regarding the characteristics parameters, a simultaneous improvement of J_{sc}, V_{oc}, and FF as mentioned above is observed for alcohol solvent treated devices. The improvement of the final device performance is predominately determined by the increased V_{oc}

sample	J_{sc} (mA/cm^2)	V_{oc} (V)	FF (%)	η (%)
reference	14.61	0.62	50.1	4.55
methanol	15.83	0.68	55.5	6.01
ethanol	14.96	0.63	52.2	4.96
2-propanol	15.24	0.66	53.1	5.33
1-butanol	15.61	0.66	51.6	5.35

Table 7.1: *Characteristic parameters of reference and alcohol solvents treated polymer solar cells prepared from PTB7:PC_{71}BM dissolved in chlorobenzene with 3 vol% additive DIO.*

and FF induced by the solvent treatment: For methanol treated devices, a significant increase of V_{oc} from 0.62 V to 0.68 V is achieved, and FF also shows a decent enhancement from 50.1% up to 55.5%. A similar but a relatively lower increase of V_{oc} (up to 0.66 V) and FF (to about 53.5%) is observed for 2-propanol and 1-butanol treated devices. In comparison, the increase of V_{oc} (0.63 V) and FF (52.2%) for ethanol treated device is the lowest. Overall, J_{sc} remains rather stable, irrespective of the used alcohol, which indicates that the mobility and the extraction of charge carriers are not significantly affected by the solvent treatment.

Although it is feasible to further optimize the device performance for instance by an incorporation of spacer layers between the photoactive layer and the Al electrode or by operating the whole device fabrication and measurement procedures under nitrogen atmosphere,[102, 30] the implementation of spacer layers is very time-consuming and challenging due to the complexity of multi-layer devices. Consequently, an unnecessary degree of complexity to the investigation of the film structure is included. As for commonly used interlayer for enhancing the device performance, additional requirements such as perfect match between the HOMO of the donor material and the LUMO of the acceptor material is needed. In comparison, solvent treatment appears to be the easiest method in improving the efficiency of PSCs without time-consuming and laborious fabrication procedures of interlayer materials. Since morphological study is the main focus of this work instead of achieving the highest efficiency, thus the corresponding architecture of the solar cells is maintained as similar as possible to those investigated pure photoactive layers without the influence of additional interlayers. Therefore, our results are sufficient to provide first insight to address the efficiency/morphology relationship.

7.2 Optical properties

To start with, optical properties of the pristine PTB7:$PC_{71}BM$ BHJ blend film and solvent treated films are studied with UV/Vis measurements as shown in Figure 7.2. A linear superposition of the spectra of the individual materials, the fullerene $PC_{71}BM$ and the polymer PTB7, is observed. For pristine (dashed curve) and alcohol solvent treated PTB7:$PC_{71}BM$ BHJ films (solid curves), the absorption spectra are identical. According to the Beer-Lambert law the absorption is proportional to the film thickness, if the same material composition is used. Therefore, it is concluded that the solvent treatment with the four different alcohols causes no evident change in the film thickness, agreeing with Zhou's findings as verified by profilometry.[102] This observation shows that the optical properties of the components of the blend are not altered by the alcohol treatments. Hence, it rules out the possibility that the resulting efficiency variance among the pristine and the solvent-treated PTB7:$PC_{71}BM$ BHJ solar cell is caused by a change in the light absorption of each film. Due to similar thickness of the active layers seen in Figure 7.2, the enhancement of solar cell performance must arise from either the reconstructed morphologies of the PTB7:$PC_{71}BM$ active layers or the modified interface energy levels introduced by the solvent treatment discussed as follows.

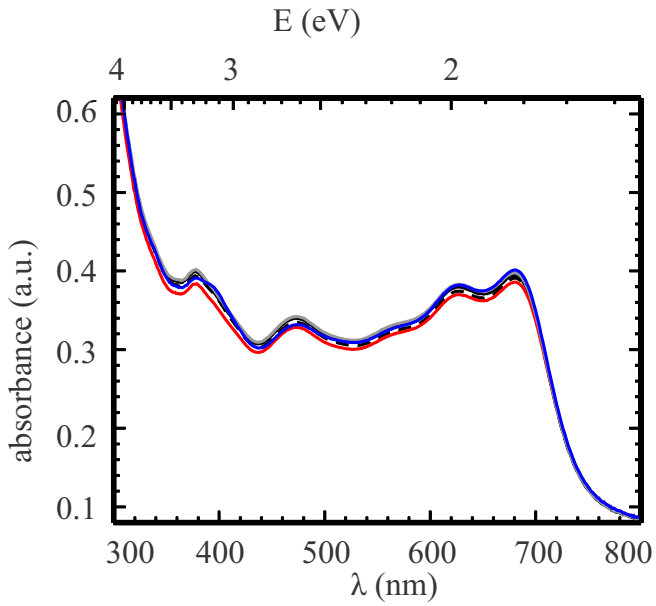

Figure 7.2: *Absorption spectra of PTB7:$PC_{71}BM$ solar cells with different solvent treatments: reference solar cell (black dash line), with methanol treatment (black solid line), with ethanol treatment (red solid line), with 2-propanol treatment (gray solid line), and with 1-butanol treatment (blue solid line).*

7.3 Mesoscopic structure

7.3.1 Mesoscopic surface structure

Since the photovoltaic performance of PSCs is closely correlated with the morphology of the photoactive layer,[135, 52] the surface morphology of the PTB7:PC_{71}BM films without and with solvent treatment is studied using an optical microscopy and AFM. Optical micrographs show homogeneous film surfaces for all investigated samples and no additional structural variance can be extracted due to limited resolution as seen in Figure 7.3. The occasional black dots are suggested to be undissolved large molecule weigh polymer PTB7. In order to further resolve smaller surface structures and determine the surface roughness of the films down to nanometer length scale, AFM measurements are performed in tapping mode.

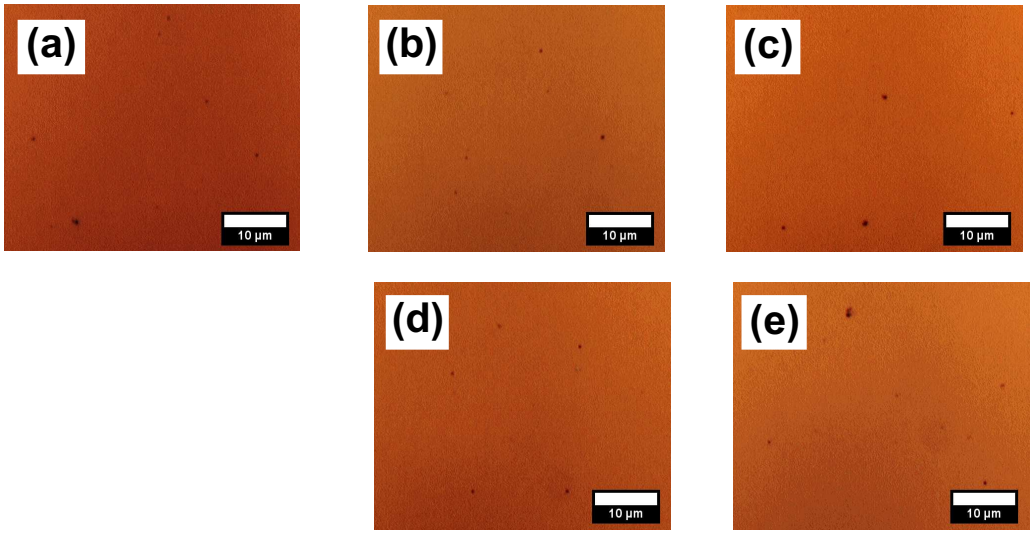

Figure 7.3: *Optical microscopy images of PTB7:PC_{71}BM solar cells with different solvent treatments: (a) reference solar cell , (b) with methanol treatment), (c) with ethanol treatment, (d) with 2-propanol treatment, and (e) with 1-butanol treatment, respectively.*

In Figure 7.4, the topography images of the pristine and solvent-treated PTB7:PC_{71}BM films are shown. Both, the pristine and solvent treated PTB7:PC_{71}BM films exhibit similar surface topographies, irrespective of the used alcohol solvents. It is thus suggested that no significant impact of the used alcohol treatment is obtained for the film surface topography, and only homogeneous films are observed down to nanometer level. The surface roughness values measured from the topography images are 12 Å for pristine blend films as well as for methanol and ethanol treated films. The roughness of the active layers

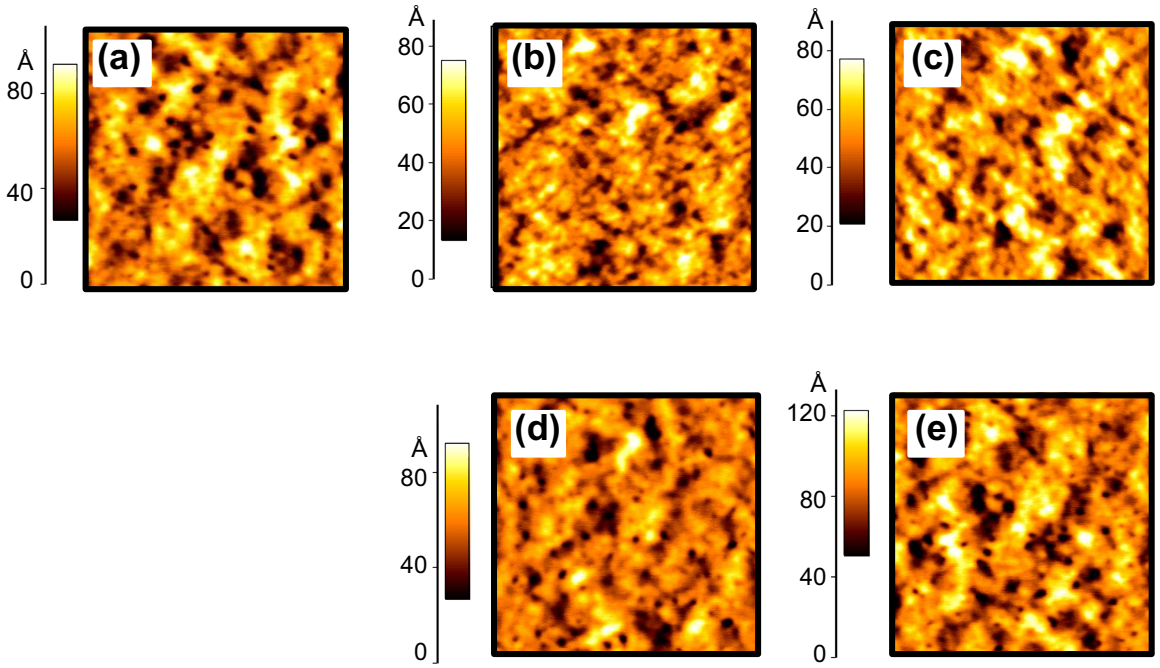

Figure 7.4: *AFM topography images of PTB7:$PC_{71}BM$ solar cells with different solvent treatments: (a) reference solar cell , (b) with methanol treatment), (c) with ethanol treatment, (d) with 2-propanol treatment, and (e) with 1-butanol treatment, respectively. The scan size for all images are 2×2 μm^2. Different color bars indicate the height variance among different samples.*

slightly increases up to 14 Å for 2-propanol and 1-butanol treated films. In sum, the PTB7:$PC_{71}BM$ film roughness stays rather constant before and after solvent treatment.

In contrast, as shown in Figure 7.5, AFM phase images of pristine and solvent-treated PTB7:$PC_{71}BM$ films reveal differences in the surface structures. A phase-separated morphology is observed for all sample with different preparation procedures, but clear differences in phase images with different sample treatment: A phase separation structure with coarsened domains is formed for pristine PTB7:$PC_{71}BM$ films, whereas fibrillar features with smaller structures are generally observed for all films after alcohol treatment. Amongst all, the smallest structure sizes are obtained from methanol treated films, which is in good agreement with previous investigations by Wang et al..[136] Such smallest structure sizes could possibly explain the highest solar cell efficiency found for the methanol treatment from the surface structure point of view. As a real space imaging technique, AFM provides a direct image of the film surface morphology. However, no quantitative results regarding the modification of the inner film morphology can be obtained from such technique. In order to explore the morphological evolution induced by solvent treatment inside the films, advanced scattering techniques are applied to gain statistically relevant

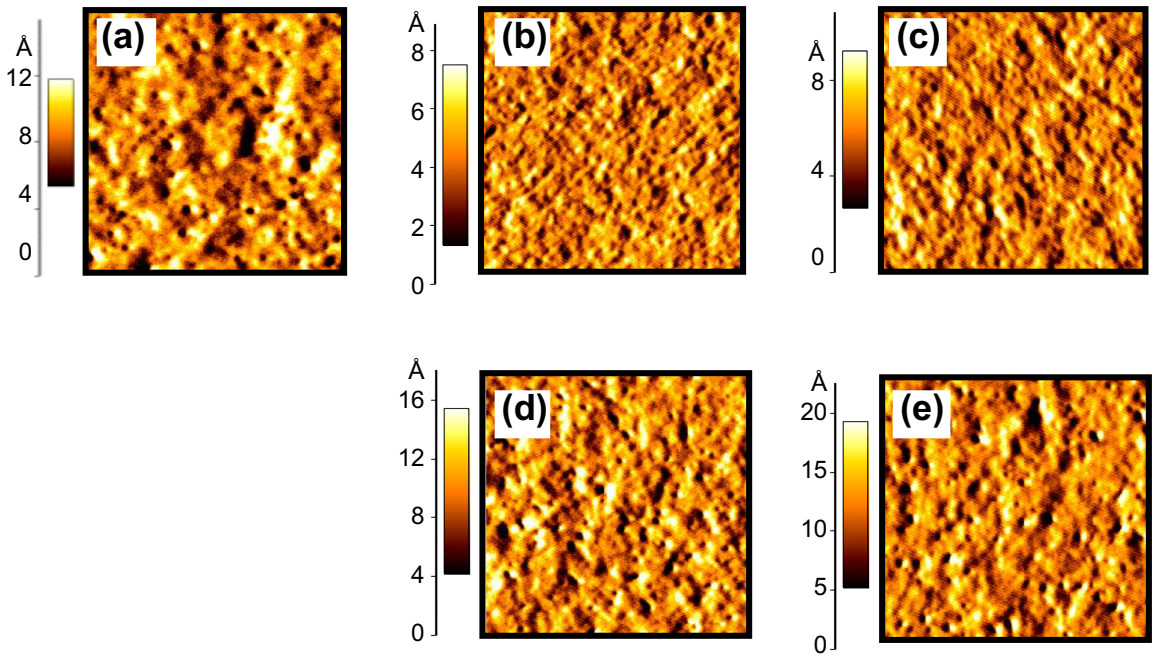

Figure 7.5: *AFM phase images of PTB7:PC_{71}BM solar cells with different solvent treatments: (a) reference solar cell , (b) with methanol treatment, (c) with ethanol treatment, (d) with 2-propanol treatment, and (e) with 1-butanol treatment, respectively. The scan size for all images are* $2 \times 2\ \mu m^2$.

structure information.

7.3.2 Mesoscopic lateral structure

In this work, diffuse scattering in grazing incidence geometry is used to probe the most prominent lateral structures of the active layers.[137] GISANS is applied to obtain information about the inner nanoscale structures, such as the characteristic lateral length scales, domain geometries and size distributions. Furthermore, neutron scattering technique causes no radiation damage as compared with high intensity X-ray technique. The GISANS experiments in present work are performed in combination with a time of flight (TOF) mode, meaning that a broad neutron wavelength range instead of a fixed neutron wavelength is in use. TOF-GISANS provides the feasibility to probe the depth-sensitive information from the film volume using different neutron wavelengths, i.e., the structural information of bulk film is probed at short neutron wavelengths, whereas surface sensitive information is obtained using long neutron wavelengths.[137, 138]

In Figure 7.6, several representative two dimensional (2D) GISANS data obtained from

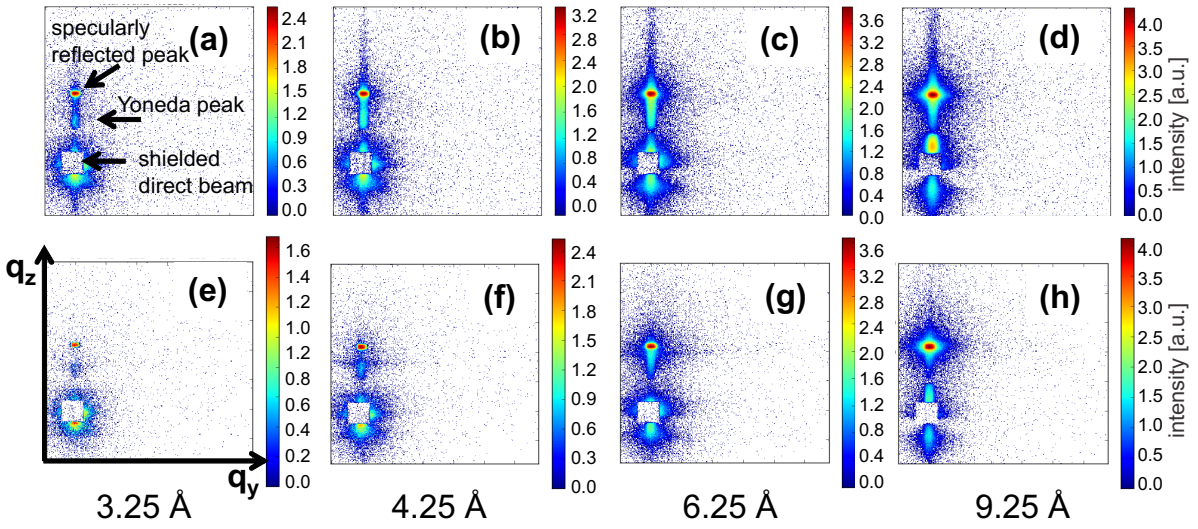

Figure 7.6: *An exemplary presentation of 2D GISANS data of (a-d) the pristine PTB7:PC_{71}BM film and (e-f) 1-butanol treated PTB7:PC_{71}BM film with increasing wavelength obtained simultaneously in the TOF-GISANS measurement for each sample. From left to right, the corresponding mean wavelengths are 3.25 Å, 4.25 Å, 6.25 Å, and 9.25 Å, respectively. The intensity color was selected individually for every frame to illustrate the scattering features.*

the pristine PTB7:PC_{71}BM film (Figure 7.6(a-d)) and the butanol-treated PTB7:PC_{71}BM film (Figure 7.6(e-h)) with increasing wavelengths are presented. Four wavelengths (3.25 Å, 4.25 Å, 6.25 Å, and 9.25 Å) all measured simultaneously in the TOF-GISANS measurement are selected from the broad wavelength band. There are three main features observable in these 2D GISANS data: The specularly reflected peak, the intensity side maxima at the Yoneda peak position and the transmitted signal centered around the shielded direct beam.

For the 2D GISANS data obtained from the pristine PTB7:PC_{71}BM film shown in Figure 7.6(a-d), only the variation of the intensity originated from the wavelength distribution of the incoming neutron flux is observed with increasing wavelength. From the GISANS data of the butanol treated PTB7:PC_{71}BM film shown in Figure 7.6(e-h), more pronounced intensity side maxima at the Yoneda peak position are observed as compared to those of untreated PTB7:PC_{71}BM film. Furthermore, these side maxima expand to higher q_y values, demonstrating a shrinking prominent length scales after butanol treatment. In addition, the intensity side maxima in Figure 7.6(e-h) firstly expand to a high q_y range at low neutron wavelengths (range from 3.25 Å to 6.25 Å) and then diminish at long neutron wavelengths (above 9.25 Å). It is a further hint that the average domain size on the film surface is bigger than that of the inner film.

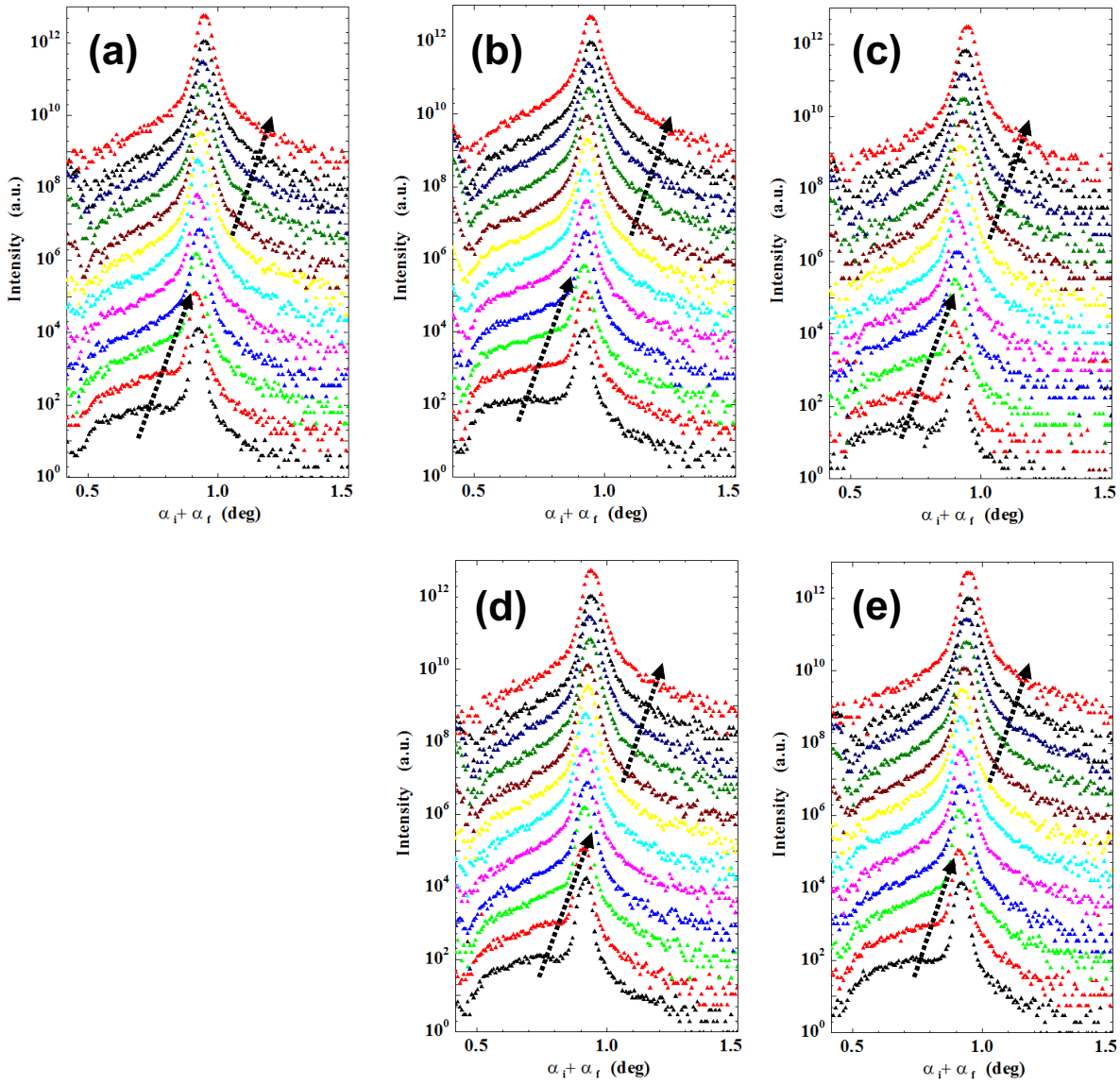

Figure 7.7: *Logarithmic plots of the vertical line cuts of the 2D TOF-GISANS data performed at $q_y = 0$ for PTB7:PC_{71}BM films: (a) pristine film without any solvent treatment, (b) with methanol treatment, (c) with ethanol treatment, (d) with 2-propanol treatment, and (e) with 1-butanol treatment. The intensity is shown as a function of the detector angle $\alpha_i + \alpha_f$ from 0.5° to 1.5°. The wavelength increases from 5.25 Å (bottom red data points) to 10.75 Å (top green data points) gradually with an increment of 0.5 Å. The shift of Yoneda peak towards larger exit angles is indicated by the arrow. The curves are shifted along intensity axis for clarity of the presentation.*

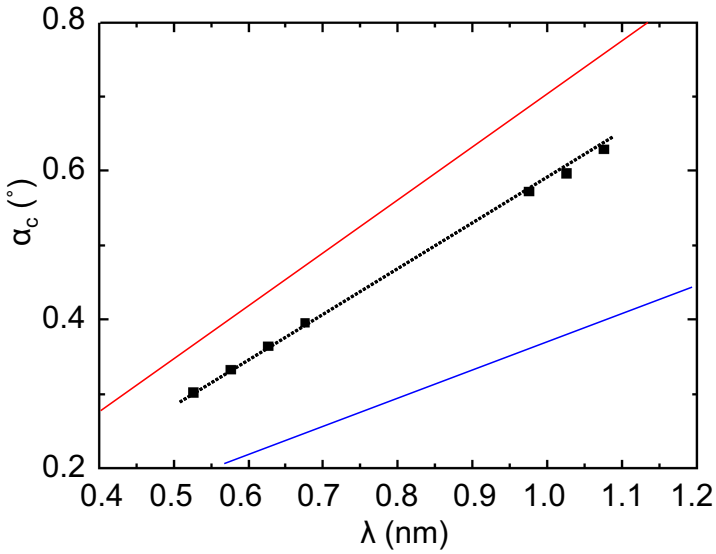

Figure 7.8: *Wavelength dependence of the position of the critical angle (Yoneda peak position): The experimentally determined positions (black dots) match the calculated theoretical behavior of the PTB7:$PC_{71}BM$ blend (dashed line). The solid lines indicate the Yoneda peak position of the individual component PTB7 (blue) and $PC_{71}BM$ (red).*

A further quantitative evaluation of the structure information is realized by performing vertical and horizontal line cuts of the 2D TOF-GISANS data (referring to the sample surface). The corresponding vertical line cuts of the pristine and solvent treated PTB7:PC_{71}BM films are plotted in Figure 7.7. Usually the structural information perpendicular to the sample surface is accessed from the analysis of such vertical line cuts, and the characteristic lateral structural information is obtained from the modelling of the horicaontal line cuts. From the vertical line cuts shown in Figure 7.7, pronounced specular peaks and a shift of the Yoneda peak towards larger exit angles (as indicated by the arrow in Figure 7.7) are observed. According to the relation between the critical angle (determines the position of the Yoneda peak) and the neutron wavelengths described by the equation $\alpha_i = \lambda\sqrt{SLD/\pi}$, the shift of the Yoneda peak position can be explained as a result of increasing wavelengths.[139] It should be noted that the shift of the Yoneda peak observed in the vertical line cuts does not contradict with the inconspicuous shift in the 2D GISANS data shown in Figure 7.6, as each 2D GISANS image covers a different q_{yz} range. Moreover, the detected angle α_f exhibits a linear dependence on the wavelength, as summarized in Figure 7.8.

As mentioned before, information about the lateral structures is revealed by the horizontal line cuts at the critical angle of each material. Therefore, the analysis of the horizontal line cuts is the main aim in order to determine the domains sizes and the size

distribution. The horizontal line cuts with their corresponding errorbars are plotted in Figure 7.9 for all 2D GISANS data obtained from the pristine and the solvent-treated PTB7:PC_{71}BM BHJ films. As seen from the horizontal line cuts in Figure 7.9, the neutron wavelength increases from 5.25 Å to 10.75 Å from bottom to top with an increment of 0.5 Å.

In present investigation, the morphology of the bulk film is revealed at short wavelengths smaller than 8 Å and the surface sensitive information at long neutron wavelengths larger than 8 Å. A simplified model is applied to model the intensity distribution of all horizontal line cuts obtained from the pristine and solvent-treated PTB7:PC_{71}BM films. This model assumes spherical-shaped scattering objects distributed over a one dimensional paracrystal lattice within the frame of the DWBA. By fitting all the data points, the most prominent in-plane length scales are therefore determined as introduced in section 2.3.3.[81, 72] More specifically, form factors, structure factors, as well as the size distributions can be extracted from the model. The form factor is used for resolving the scattering objects and the structure factor is associated with the spatial distribution of different scattering objects. Depending volume film or surface sensitive structure information is to be extracted, different amount of form and structure factors are considered. In this work, two objects (R1, D1 and R2, D2) are required to describe the volume information (horizontal line cuts probed with short neutron wavelengths), whereas only one object (R3, D3) is needed to model the surface information (horizontal line cuts probed with long neutron wavelengths). The extracted modelling results are subsequently summarized in Figure 7.10, which shows the most prominent structural features of the PTB7:PC_{71}BM BHJ active layers, without and with alcohol solvent treatment (methanol, ethanol, 2-propanol, and 1-butanol). It includes two inner film domain sizes R1, R2, and the one surface domain size R3, as extracted from the fitting results.

For both pristine and solvent-treated PTB7:PC_{71}BM BHJ films, no obvious change occurs to the large inner domain sizes R2 (about 250 nm) and the distances between two adjacent domains D2 (not shown in the graph). The surface domain sizes R3 and the corresponding distance D3 are in a similar lengthscale. It is observed that a certain size decrease is found for all solvent-treated films, and the smallest domain size is obtained from the methanol-treated films, which is in agreement with those features of AFM phase images in Figure 7.5. Amongst all three domain sizes, most pronounced changes are observed for the small inner domain size R1, which evolves from (70±6 nm) for the pristine PTB7:PC_{71}BM BHJ films to overall smaller sizes for solvent treated PTB7:PC_{71}BM BHJ films.

As for all films treated with different solvents, the smallest inner lateral structures

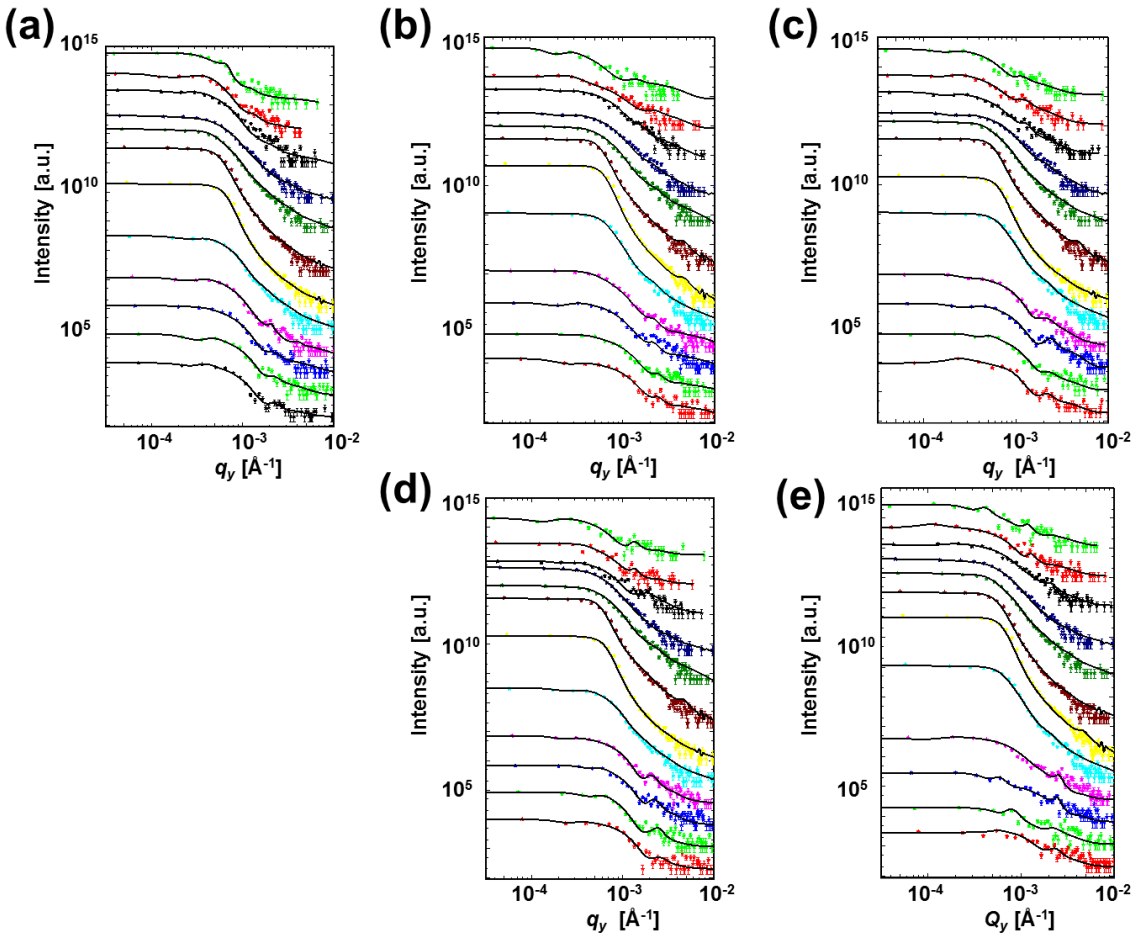

Figure 7.9: *Logarithmic plots of the horizontal line cuts at the critical angles of the 2D TOF-GISANS data and the corresponding fits for PTB7:$PC_{71}BM$ films: (a) pristine film without any solvent treatment, (b) with methanol treatment, (c) with ethanol treatment, (d) with 2-propanol treatment, and (e) with 1-butanol treatment. The wavelength increases from 5.25 Å (bottom red data points) to 10.75 Å (top green data points) with an increment of 0.5 Å. The curves are shifted along the intensity axis for clarity of the presentation.*

(35±3 nm) is extracted from the one after methanol treatment. This smallest inner lateral structures together with the smallest fibrillar feature of film surface from AFM phase images can well explain the improved J_{sc} and FF values since exciton splitting can be most efficient in this case. Wang et al. reported similar structural rearrangements introduced by solvent treatment on a different low bandgap polymer PBDTF-DFBO:$PC_{71}BM$ BHJ system. They suggested the formation of fiber-like interpenetrating morphologies and more balanced charge transport is mainly responsible for the final improvement of the device performance.[136]

In present work, it is postulated that solvent treatment improves the blend solubility

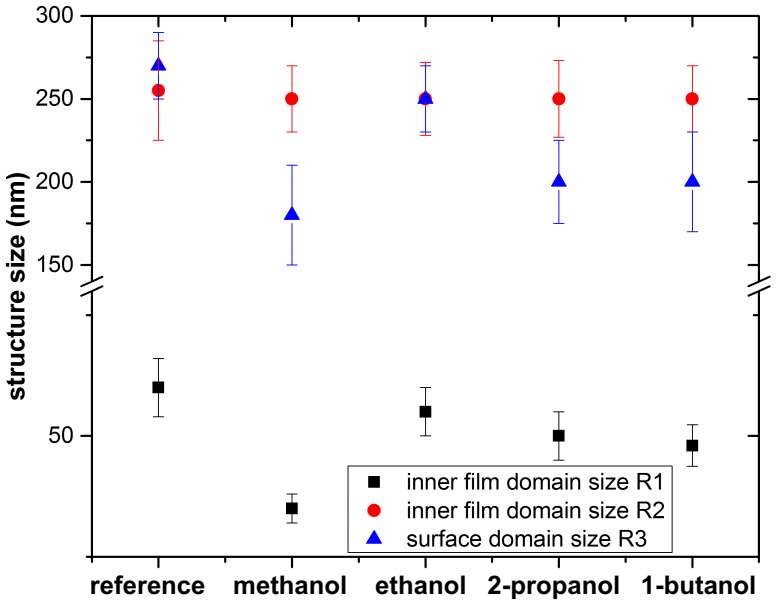

Figure 7.10: *Most prominent structural features of PTB7:$PC_{71}BM$ BHJ active layers without and with post-solvent treatment (methanol, ethanol, 2-propanol, and 1-butanol) as extracted from TOF-GISANS: Two inner film domain sizes R1 (black squares), R2 (red circles), and one surface domain size R3 (blue triangle).*

and miscibility between PTB7 and $PC_{71}BM$, leading to the formation of finer interpenetrating morphology of the blend films. More importantly, the alcohol solvent with high volatility can take away residual DIO in the blend layer during evaporation,[92] hindering further diffusion of PCBM molecules into polymer network. As a result, overmixed morphology between PTB7 and $PC_{71}BM$ is avoided,[140] and consequently an optimal interpenetrating structures for maximum PCE is produced. Among the four alcohol solvents, methanol appears to be the best so far, possibly due to its highest volatility, resulting in minimum amount of residual solvent in the blend film.

Nevertheless, the modification of the inner film morphology of the active layers cannot fully address the enhanced PCE for the solvent-treated solar cells, as evident by the moderate increase of J_{sc}. As mentioned in the section of solar cell performance, the significantly improved V_{oc} as well contributes to the enhanced device performance.

7.3.3 Results

It is demonstrated from this work that facile post treatment methods like alcohol solvent treatment could become an efficient, economic strategy toward higher efficient polymer

solar cells superior to the laborious interlayer implementation. A systematic study of the effect of solvent treatment with a series of four different alcohol solvents on the polymer solar cell efficiency is reported for the first time. It is concluded that alcohol solvent treatment with methanol, ethanol, 2-propanol, and 1-butanol all have a clear positive influence on the corresponding device performances. The reason for this efficiency enhancement is mainly studied in this chapter. Among four solvent treatments, devices with methanol treatment give rise to the highest efficiency and up to 25% enhancement of the PCE is obtained accordingly. No obvious change can be observed from the absorption and optical characterization, as only homogenous films with identical film thickness are obtained for both pristine and solvent treated PTB7:$PC_{71}BM$ films. The morphological rearrangement is presumably accounted for the performance enhancement. The structural modification on film surface is revealed by AFM phase images that phase separation with smaller domains are formed generally for all solvent-treatmented blend films, and the smallest fibrillar features is observed with the one treated with methanol treatment. In addition, a shrinking domain and structure sizes for all the alcohol treated samples is further examined by TOF-GISANS measurement. Similar to the evolvement of the film surface features, methanol treatment helps to produce the smallest domain sizes of the volume film as compared with those treated with other three tested alcohols. The minimized domain sizes is benificial for more efficient charge splitting, and enventually a higher J_{sc} and PCE.

7.4 Summary

In conclusion, the improvement of device performance induced by alcohol solvent treatment is ascribed to a simultaneous increase of J_{sc}, FF, and especially the V_{oc}. It is proposed that post solvent treatment leads to the optimized film morphology as examined by AFM and TOF-GISANS measurements and the reduced electron injection barrier at the organic/metal interface. As a consequence, the charge separation, transportation, and extraction are improved effectively. From this investigation, it is firstly proved that not only the widely used methanol could play a significant role, but also ethanol, 2-propanol, and 1-butanol all could improve the device performance to certain extent. Among the four alcohol solvents, methanol appears to be the best solvent used during post solvent treatment procedure so far. The possible explanation is that methanol with the highest volatility facilites to remove the low volatile residual solvent additive DIO existing in the solid blend films, leading to the formation of the optimal domain sizes. It is demonstrated by this work that facile interface modification method like alcohol solvent treatment is an efficient, economic strategy toward higher efficient low-cost polymer solar cells. Giving

the successful application of solvent treatment on other material combinations such as well-studied P3HT: PC_{61}BM BHJ system,[131, 132] it is positively suggested that alcohol treatment after the depositon of the photoactive layer can be widely used to other polymer:fullerene systems as an environmental friendly, efficient, simple method to greatly improve the device performances.

Chapter 8

Conclusion and outlook

The main focus of this thesis is to elucidate the morphology/efficiency relationship of the OPV technology by selectively changing the internal or external parameters such as the used polymer, the used host solvent, or additional post alcohol solvent treatment. The highly efficient polymer:fullerene PTB7:$PC_{71}BM$ BHJ system is investigated by tuning the fluorination content of the polymer, changing of the host solvent and the post solvent treatment with four common alcohols.

Firstly, novel fluorinated polymers PTB7-Fx (fluorine units coupled with submonomer thieno[3,4-b]thiophene) with varied degree of fluorination blended with $PC_{71}BM$ in a BHJ geometry are deeply investigated. Full fluorination at the third C-atom of thienothiophene gives rise to the highest power conversion efficiency. As the absorption properties, film morphology and crystalline behaviour stay rather similar for different degrees of fluorination, the main influence of the photovoltaic performance is ascribed to the different LUMO of each polymer instead of the film morphology. Thus the device performance can be efficiently improved by tuning the energy level of the polymer without necessarily changing either the film nanomorphology or crystalline behaviour dramatically.

Subsequently, as one of the highest efficient low bandgap polymers PTB7, the influence of different solvents and the additive DIO on the molecular arrangement, mesoscopic and crystalline structure of BHJ PTB7-F40:$PC_{71}BM$ films is thoroughly studied. Chlorobenzene turns out to be the best solvent for particular PTB7:$PC_{71}BM$ BHJ solar cells. The solvent-induced variation in device performance is mainly ascribed to the changes in lateral structure sizes, whereas the highest device performance is a result of smallest average multi-lengthscale lateral structure sizes with one size fitting to the exciton diffusion length.

Finally, taking the best performed material combination PTB7-F100:$PC_{71}BM$ and the most suitable solvent chlorobenzene, an environmentally friendly alcohol treatment is

additionally applied as a post treatment method to further improve the device efficiency of PTB7:PC_{71}BM BHJ system. It is demonstrated that besides the most commonly used methanol treatment, other alcohol solvents such as ethanol, 2-propanol, and 1-butanol can also improve the device performance to certain extent as compared to the untreated solar cells. The enhanced device performance induced by alcohol treatment is correlated to the reconstruction of the inner film structure and the modified energy level at the interfaces between the BHJ layer and the aluminium electrode, evident by the enhanced short-circuit current and open-circuit voltage of all devices. More generally, it is positively suggested that alcohol treatment can be widely applied to other polymer:fullerene systems as an facile efficient method to greatly improve the device performance.

In summary, throughout a systematic investigation on the polymer:fullerene BHJ system, all the questions rising in the introduction section can be thereby addressed. It is observed that by fine-tuning the p-type polymer structure with varied degree of fluorination, judicious selection of the host solvent together with solvent additive, as well as facile post solvent treatment method with environmentally friendly alcohol solvents, the final device performance is consequently affected. Each of the mentioned parameters can exerts certain influence on the formation of film morphology and therefore the device performance. However, it is difficult to quantify the influential level of each parameter. The highest solar cell efficiency is generally a dominant or combinational effect of the following factors: the optimal matching of the energy levels, small average lateral domain sizes, highest crystallinity of the polymer, favorable vertical segregation, depending on the investigated system. For the PTB7:PC_{71}BM BHJ system investigated in this thesis, the golden rule for fabricating the best PCE of the polymer:fullerene PTB7:PC_{71}BM BHJ solar cells (6%) is using the fully fluorinated polymer PTB7-F100 together with chlorobenzene:DIO as the host solvent mixture, and additionally the post solvent (methanol) treatment. As a consequence, our comprehensive approach to understand device performance represents significant progress in understanding what limits these high-efficiency PTB7:PC_{71}BM systems.

To further unlock the great potential of OPV and realize its market launch in large scale, future investigations concerning OPV technology from the device efficiency, the cost and lifetime aspects are essential. It has been shown that device efficiency can be further improved by the implementation of interlayers (such as doped conjugated microporous polymer layer between PEDOT:PSS and the active layer, or PFN layer underneath the aluminium electrode).[30] The cost of the device could be possibly reduced by producing the polymers and fullerene in a large amount and using the promising Roll-to-Roll fabrication technique, and the lifetime of the device could be expanded by using air-stable materials and inverted solar cell geometry.

Moreover, it should be noticed that chlorinated solvents are commonly used for processing in laboratories in general, which have restricted application in industrial operation due to safety risks and processing costs. Environment-friendly inks are therefore one decisive criterion for mass production that should provide full functionality. Hence, researches on environmentally friendly solvent for fabrication of OPV devices become imperative in the future work. Nevertheless, the striking potentials of OPV have been clearly evident and hopefully this newly emerged technology will bring substantial benefits and great conveniences to our society.

Bibliography

[1] R. Perez and M. Perez, "A fundamental look at energy reserves for the planet," 2009.

[2] N. Armaroli and V. Balzani, "The future of energy supply: Challenges and opportunities," *Angew. Chem. Int. Ed.*, vol. 46, pp. 52–66, 2007.

[3] E. Bundgaard and F. C. Krebs, "Low band gap polymers for organic photovoltaics," *Sol. Energ. Mat. Sol. Cells*, vol. 91, pp. 954–985, 2007.

[4] G. Yu, C. Zhang, and A. J. Heeger, "Dual-function aemiconducting polymer devices: Light-emitting and photodetecting diodes," *Appl. Phys. Lett.*, vol. 64, pp. 1540–1542, 1994.

[5] S. Darling and F. You, "The case for organic photovoltaics," *RSC Adv.*, vol. 3, pp. 17633–17648, 2013.

[6] H. Shirakawa, E. J. Louis, A. G. MacDiarmid, C. K. Chiang, and A. J. Heeger, "Synthesis of electrically conducting organic polymers: halogen derivatives of polyacetylene, (CH)," *J. Chem. Soc., Chem. Commun.*, pp. 578–580, 1977.

[7] N. S. Sariciftci, D. Braun, C. Zhang, V. I. Srdanov, A. J. Heeger, G. Stucky, and F. Wudl, "Semiconducting polymer-buckminsterfullerene heterojunctions: Diodes, photodiodes, and photovoltaic cells," *Appl. Phys. Lett.*, vol. 62, pp. 585–587, 1993.

[8] M. Granström, K. Petritsch, A. C. Arias, A. Lux, M. R. Andersson, and R. H. Friend, "Laminated fabrication of polymeric photovoltaic diodes," *Nature*, vol. 395, pp. 257–260, 1998.

[9] G. Yu, J. Gao, J. C. Hummelen, F. Wudl, and A. J. Heeger, "Polymer photovoltaic cells: enhanced efficiencies via a network of internal donor-acceptor heterojunctions," *Science*, vol. 270, pp. 1789–1791, 1995.

[10] J. J. M. Halls, C. A. Walsh, N. Greenham, E. A. Marseglia, R. Friend, S. C. Moratti, and A. Holmes, "Efficient photodiodes from interpenetrating polymer networks," *Nature*, vol. 376, pp. 498–500, 1995.

[11] S. Karg, W. Riess, V. Dyakonov, and M. Schwoerer, "Electrical and optical characterization of poly(phenylene-vinylene) light emitting diodes," *Synt. Met.*, vol. 54, pp. 427–433, 1993.

[12] M. Dang, L. Hirsch, and G. Wantz, "P3ht:pcbm, best seller in polymer photovoltaic research," *Adv. Mater.*, vol. 23, pp. 3597–3602, 2011.

[13] L. Lu and L. Yu, "Understanding low bandgap polymer ptb7 and optimizing polymer solar cells based on it," *Adv. Mater.*, no. DOI: 10.1002/adma.201400384, 2014.

[14] J. Y. Kim, S. H. Kim, H.-H. Lee, K. Lee, X. Ma, W.and Gong, and A. J. Heeger, "New architecture for high-efficiency polymer photovoltaic cells using solution-based titanium oxide as an optical spacer," *Adv. Mater.*, vol. 18, pp. 572–576, 2006.

[15] Z. He, C. Zhong, X. Huang, W.-Y. Wong, H. Wu, L. Chen, S. Su, and Y. Cao, "Simultaneous enhancement of open-circuit voltage, short-circuit current density, and fill factor in polymer solar cells," *Adv. Mater.*, vol. 23, pp. 4636–4643, 2011.

[16] W. J. D. Beenken, "Excitons in conjugated polymers: Do we need a paradigma change?," *physica status solidi (a)*, vol. 206, pp. 2750–2756, 2009.

[17] D. Kurrle and J. Pflaum, "Exciton diffusion length in the organic semiconductor diindenoperylene," *Appl. Phys. Lett.*, vol. 92, pp. 133306–1–133306–3, 2008.

[18] H. Wang, H.-Y. Wang, B.-R. Gao, L. Wang, Z.-Y. Yang, X.-B. Du, Q.-D. Chen, J.-F. Song, and H.-B. Sun, "Exciton diffusion and charge transfer dynamics in nano phase-separated p3ht/pcbm blend films," *Nanoscale*, vol. 3, pp. 2280–2285, 2011.

[19] P. Peumans, A. Yakimov, and R. S. Forrest, "Small molecular weight organic thin-film photodetectors and solar cells," *J. Appl. Phys.*, vol. 93, pp. 3693–3723, 2003.

[20] A. Cook, S. amd Furube, R. Katoh, and L. Han, "Estimate of singlet diffusion lengths in pcbm films by time-resolved emission studies," *Chem. Phys. Lett.*, vol. 478, pp. 33–36, 2009.

[21] L. Onsager, "Initial recombination of ions," *Phys. Rev.*, vol. 54, pp. 554–557, 1938.

[22] C. L. Braun, "Electric field assisted dissociation of charge transfer states as a mechanism of photocarrier production," *J. Chem. Phys.*, vol. 80, pp. 4157–4161, 1984.

[23] M. Pope and C. E. Swenberg, "Electronic processes in organic crystals and polymers," *Oxford University Press*, 1999. 2nd.

[24] A. Miller and E. Abrahams, "Impurity conduction at low concentrations," *Phys. Rev.*, vol. 120, pp. 745–755, 1960.

[25] W. F. Pasveer, J. Cottaar, C. Tanase, R. Coehoorn, P. A. Bobbert, P. W. M. Blom, D. M. de Leeuw, and M. A. J. Michels, "Unified description of charge-carrier mobilities in disordered semiconducting polymers," *Phys. Rev. Lett.*, vol. 94, pp. 206601–1–206601–4, 2005.

[26] H. Houili, E. Tutis, I. Batistic, and L. Zuppiroli, "Investigation of the charge transport through disordered organic molecular heterojunctions," *J. Appl. Phys.*, vol. 100, pp. 033702–1–033702–12, 2006.

[27] H. Bässler, "Charge transport in disordered organic photoconductors - a Monte Carlo simulation study," *Phys. Status Solidi b*, vol. 175, pp. 15–56, 1993.

[28] C. Deibel and V. Dyakonov, "Polymer-fullerene bulk heterojunction solar cells," *Rep. Prog. Phys.*, vol. 73, pp. 096401–1–096401–39, 2010.

[29] A. Kumar, G. Li, Z. Hong, and Y. Yang, "High efficiency polymer solar cells with vertically modulated nanoscale morphology," *Nanotechnology*, vol. 20, pp. 165202–1–165202–4, 2009.

[30] C. Gu, Y. Chen, Z. Zhang, S. Xue, S. Sun, H. Zhong, C.and Zhang, Y. Lv, F. Li, F. Huang, and Y. Ma, "Achieving high effi ciency of ptb7-based polymer solar cells via integrated optimization of both anode and cathode interlayers," *Adv. Energy. Mater.*, vol. 4, no. DOI: 10.1002/aenm.201301771, 2014.

[31] V. D. Mihailetchi, L. J. A. Koster, J. C. Hummelen, and P. W. M. Blom, "Photocurrent generation in polymer-fullerene bulk heterojunctions," *Phys. Rev. Lett.*, vol. 93, pp. 216601–1–216601–4, 2004.

[32] R. Sokel and R. C. Hughes, "Numerical analysis of transient photoconductivity in insulators," *J. Appl. Phys.*, vol. 53, pp. 7414–7424, 1982.

[33] A. Petersen, T. Kirchartz, and T. A. Wagner, "Charge extraction and photocurrent in organic bulk heterojunction solar cells," *Phys. Rev. B*, vol. 85, pp. 045208–1–045208–11, 2012.

[34] T. Xu and L. Yu, "How to design low bandgap polymers for highly efficient organic solar cells," *Mater. Today*, vol. 17, pp. 11–15, 2013.

[35] P. E. Shaw, A. Ruseckas, and I. D. W. Samuel, "Exciton diffusion measurements in poly(3-hexylthiophene)," *Adv. Mater.*, vol. 20, pp. 3516–3520, 2008.

[36] M. Liedtcke, A. Sperlich, H. Kraus, A. Baumann, C. Deibel, M. Wirix, J. Loos, C. Cardona, and V. Dyakonov, "Triplet exciton generation in bulk-heterojunction solar cells based on endohedral fullerenes," *J. Am. Chem. Soc.*, vol. 133, pp. 9088–9094, 2011.

[37] L. J. A. Koster, E. C. P. Smits, V. D. Mihailetchi, and P. W. M. Blom, "Device model for the operation of polymer/fullerene bulk heterojunction solar cells," *Phys. Rev. B*, vol. 72, pp. 085205–1–085205–9, 2005.

[38] A. Salleo, T. W. Chen, and A. R. Völkel, "Intrinsic hole mobility and trapping in a regioregular poly(thiophene)," *Physical Review B*, vol. 70, pp. 115311–115315, 2008.

[39] L. Pauling, *The Nature of the Chemical Bond*. Oxford University Press, 1960.

[40] M. Wang, X. Hu, P. Liu, W. Li, X. Gong, and Y. Huang, F.and Cao, "Donor-acceptor conjugated polymer based on naphtho[1,2-c:5,6-c]bis[1,2,5]thiadiazole for high-performance polymer solar cells," *J. Am. Chem. Soc.*, vol. 133, pp. 9638–9641, 2011.

[41] Y. Liang, Z. Xu, J. Xia, S.-T. Tsai, Y. Wu, G. Li, C. Ray, and L. Yu, "For the bright future-bulk heterojunction polymer solar cells with power conversion efficiency of 7.4%," *Adv. Mater.*, vol. 22, p. E135–E138, 2010.

[42] C. Brabec, M. Heeney, I. McCulloch, and J. Nelson, "Influence of blend microstructure on bulk heterojunction organic photovoltaic performance," *Chem. Soc. Rev.*, vol. 40, pp. 1185–1199, 2011.

[43] G. Strobl, "Colloquium: Laws controlling crystallization and melting in bulk polymers," *Rev. Mod. Phys.*, vol. 81, pp. 1287–1330, 2009.

[44] G. Strobl, "The physics of polymers," *Springer-Verlag Berlin Heidelberg*, 2007.

[45] R. Becker, "Die keimbildung bei der ausscheidung in metallischen mischkristallen," *Ann. Physik*, vol. 32, pp. 128–140, 1938.

[46] F. P. Price, "Nucleation," *Dekker, New York*, 1969.

[47] W. Hu, "Progress in understanding of polymer crystallization," *Springer-Verlag Berlin Heidelberg*, 2007.

[48] M. V. Massa and K. Dalnoki-Veress, "Homogeneous crystallization of poly(ethylene oxide) confined to droplets: The dependence of the crystal nucleation rate on length scale and temperature," *Phys. Rev. Lett.*, vol. 92, pp. 255509–1–255509–4, 2004.

[49] G. Strobl, "From the melt via mesomorphic and granular crystalline layers to lamellar crystallites: A major route followed in polymer crystallization?," *Eur. Phys. J. E*, vol. 3, pp. 165–183, 2000.

[50] Goderis, "Primary and secondary crystallization in a homogeneous ethylene-1-octene copolymer: Crystallinity heterogeneity studied by saxs," *Macromolecules*, vol. 35, pp. 5840–5853, 2002.

[51] H. Spanggaard and F. C. Krebs, "A brief history of the development of organic and polymeric photovoltaics," *Sol. Energ. Mat. Sol. Cells*, vol. 83, pp. 125–146, 2004.

[52] M. A. Ruderer, S. Guo, R. Meier, H.-Y. Chiang, V. Körstgens, J. Wiedersich, J. Perlich, S. V. Roth, and P. Müller-Buschbaum, "Solvent-induced morphology in polymer-based systems for organic photovoltaics," *Adv. Funct. Mater.*, vol. 21, pp. 3382–3391, 2011.

[53] M. Dang, H. Wantz, G.and Bejbouji, M. Urien, O. Dautel, L. Vignau, and L. Hirsch, "Polymeric solar cells based on p3ht:pcbm: Role of the casting solvent," *Sol. Energ. Mat. Sol. Cells*, vol. 95, pp. 3408–3418, 2011.

[54] U. Vongsaysy, D. Bassani, L. Servant, B. Pavageau, G. Wantz, and H. Aziz, "Formulation strategies for optimizing the morphology of polymeric bulk heterojunction organic solar cells: A brief review," *SPIE J. Photon. Energy.*, vol. 4, pp. 040998–1–040998–22, 2014.

[55] F. Machui, "Determination of solubility parameters for organic semiconductor formulations," *Macromol. Chem. Phys.*, vol. 46, pp. 6217–6224, 2011.

[56] H. Hoppe and N. S. Sariciftci, "Morphology of polymer/fullerene bulk heterojunction solar cells," *J. Mater. Chem*, vol. 16, pp. 45–61, 2006.

[57] M. Tolan, "X-ray scattering from soft-matter thin films," *Springer-Verlag Berlin Heidelberg*, 1999.

[58] J. Lekner, "Reflection theory and the analysis of neutron reflection data," *Physica B*, vol. 173, pp. 99–111, 1991.

[59] H. Dosch, B. W. Batterman, and D. C. Wack, "Depth-controlled grazing-incidence diffraction of synchrotron x radiation," *Phys. Rev. Lett.*, vol. 56, pp. 1144–1147, 1986.

[60] W. Rodrigues, O. Sakata, T.-L. Lee, D. A. Walko, D. L. Marasco, and M. J. Bedzyk, "X-ray scattering studies of surfactant mediated epitaxial growth of si/ge/si(001) heterostructures," *J. Appl. Phys.*, vol. 88, pp. 2391–2394, 2000.

[61] F. Abelès, "La theorie generale des couches minces," *J. Phys. Radium*, vol. 11, pp. 307–310, 1950.

[62] L. G. Parratt, "Surface studies of solids by total reflection of x-rays," *Phys. Rev.*, vol. 95, pp. 359–369, 1954.

[63] M. Schalke and M. Lösche, "Structural models of lipid surface monolayers from x-ray and neutron reflectivity measurements," *Adv. Colloid Interface Sci.*, vol. 88, pp. 243–274, 2000.

[64] H. Kiessig, "Interferenz von röntgenstrahlen an dünnen schichten," *Ann. Phys.*, vol. 10, pp. 769–788, 1931.

[65] C. Braun, "Parratt32," *HMI Berlin*, 2002.

[66] P. Müller-Buschbaum and M. Stamm, "Correlated roughness, long-range correlations, and dewetting of thin polymer films," *Macromolecules*, vol. 31, pp. 3686–3692, 1998.

[67] P. Müller-Buschbaum, J. Gutmann, C. Lorenz, T. Schmitt, and M. Stamm, "Decay of interface correlation in thin polymer films," *Macromolecules*, vol. 31, pp. 9265–9272, 1998.

[68] S. K. Sinha, E. B. Sirota, S. Garoff, and H. B. Stanley, "X-ray and neutron scattering from rough surfaces," *Phys. Rev. B*, vol. 38, pp. 2297–2311, 1988.

[69] V. Holý and T. Baumbach, "Nonspecular x-ray reflection from rough multilayers," *Phys. Rev. B*, vol. 49, pp. 10668–10676, 1994.

[70] Y. Yoneda, "Anomalous surface reflection of x rays," *Phys. Rev.*, vol. 131, pp. 2010–2013, 1963.

[71] A. Naudon, D. Babonneau, D. Thiaudière, and S. Lequien, "Grazing-incidence small-angle x-ray scattering applied to the characterization of aggregates in surface regions," *Physica B*, vol. 283, pp. 69–74, 2000.

[72] P. Müller-Buschbaum, "A basic introduction to grazing incidence small angle x-ray scattering," *Springer, Berlin*, 2009.

[73] P. Müller-Buschbaum, "Structure determination in thin film geometry using grazing incidence small-angle scattering," *Springer Berlin Heidelberg*, vol. Polymer Surfaces and Interfaces: Characterization, Modification and Applications, pp. 17–46, 2008.

[74] M. Hammond, R. J. Kline, A. A. Herzing, L. J. Richter, D. S. Germack, H.-W. Ro, C. L. Soles, D. A. Fischer, T. Xu, and L. Yu, "Molecular order in high-efficiency polymer/fullerene bulk heterojunction solar cells," *ACS Nano*, vol. 5, pp. 8248–8257, 2011.

[75] W. Chen, T. Xu, F. He, W. Wang, C. Wang, J. Strzalka, Y. Lin, J. Wen, D. Miller, J. Chen, K. Hong, L. Yu, and S. Darling, "Hierarchical nanomorphologies promote exciton dissociation in polymer - fullerene bulk heterojunction solar cells," *Nano Lett.*, vol. 11, pp. 3707–3713, 2011.

[76] L. Lu, T. Xu, W. Chen, J. M. Lee, Z. Luo, I. H. Jung, H. I. Park, S. O. Kim, and L. Yu, "The role of n-doped multiwall carbon nanotubes in achieving highly efficient polymer bulk heterojunction solar cells," *Nano Lett*, vol. 13, pp. 2365–2369, 2013.

[77] N. Kawasegi and N. Morita, "Three-dimensional lithography using combination of nanoscale processing and wet chemical etching," *Nanotechnology and Nanomaterials*, no. DOI: 10.5772/56354, 2013.

[78] J. S. Gutmann, P. Müller-Buschbaum, and M. Stamm, "Complex pattern formation by phase separation of polymer blends in thin films," *Faraday Discuss.*, vol. 112, pp. 285–297, 1999.

[79] A. Buffet, A. Rothkirch, R. Döhrmann, V. Körstgens, M. Abul Kashem, J. Perlich, G. Herzog, M. Schwartzkopf, R. Gehrke, P. Müller-Buschbaum, and S. Roth, "P03, the microfocus and nanofocus x-ray scattering (minaxs) beamline of the petra iii storage ring: the microfocus endstation.," *J Synchrotron Radiat*, vol. 19, pp. 647–653, 2012.

[80] V. Rawolle, M.and Körstgens, M. Ruderer, E. Metwalli, G. Guo, S.and Herzog, G. Benecke, A. Schwartzkopf, M.and Buffet, S. Perlich, J.and Roth, and P. Müller-Buschbaum, "Note: Comparison of grazing incidence small angle x-ray scattering of a titania sponge structure at the beamlines bw4 (doris iii) and p03 (petra iii)," *Rev. Sci. Instrum.*, vol. 83, pp. 106104–1–3, 2012.

[81] P. Müller-Buschbaum, "Grazing incidence small-angle x-ray scattering: an advanced scattering technique for the investigation of nanostructured polymer films," *Anal. Bioanal. Chem.*, vol. 376, pp. 3–10, 2003.

[82] Z. He, C. Zhong, S. Su, M. Xu, H. Wu, and Y. Cao, "Enhanced power-conversion efficiency in polymer solar cells using an inverted device structure," *Nature Photon.*, vol. 6, pp. 591–595, 2012.

[83] B. Liu, R.-Q. Png, J.-K. Tan, and P. K. H. Ho, "Evaluation of built-in potential and loss mechanisms at contacts in organic solar cells: Device model parameterization, validation, and prediction," *Adv. Energy. Mater.*, vol. 4, no. DOI: 10.1002/aenm.201200972, 2013.

[84] M. Yamada, T. Akasaka, and S. Nagase, "Carbene additions to fullerenes," *Chem. Rev.*, vol. 113, pp. 7209–7264, 2013.

[85] P. H. Wöbkenberg, D. D. Bradley, D. Kronholm, J. C. Hummelen, D. M. de Leeuw, M. Cölle, and T. D. Anthopoulos, "High mobility n-channel organic field-effect transistors based on soluble c60 and c70 fullerene derivatives," *Synt. Met.*, vol. 158, pp. 468–472, 2008.

[86] Y. Li, "Molecular design of photovoltaic materials for polymer solar cells: Toward suitable electronic energy levels and broad absorption," *Acc. Chem. Res.*, vol. 45, pp. 723–733, 2012.

[87] J. Peet, J. Y. Kim, N. E. Coates, W. L. Ma, D. Moses, A. J. Heeger, and G. C. Bazan, "Efficiency enhancement in low-bandgap polymer solar cells by processing with alkane dithiols," *Nat. Mater.*, vol. 6, pp. 497–500, 2007.

[88] S. J. Lou, J. M. Szarko, T. Xu, L. Yu, T. J. Marks, and L. X. Chen, "Effects of additives on the morphology of solution phase aggregates formed by active layer components of high-efficiency organic solar cells," *J. Am. Chem. Soc.*, vol. 133, pp. 20661–20663, 2011.

[89] P. Müller-Buschbaum, N. Hermsdorf, S. V. Roth, J. Wiedersich, S. Cunis, and R. Gehrke, "Comparative analysis of nanostructured diblock copolymer films," *Spectrochimica Acta Part B*, vol. 59, pp. 1789–1797, 2004.

[90] D. W. Schubert and T. Dunkel, "Spin coating from a molecular point of view: Its concentration regimes, influence of molar mass and distribution," *Materials Research Innovations*, vol. 7, pp. 314–321, 2003.

[91] J. H. Seo, A. Gutacker, Y. Sun, H. Wu, F. Huang, Y. Cao, U. Scherf, A. J. Heeger, and G. C. Bazan, "Improved high-efficiency organic solar cells via incorporation of a conjugated polyelectrolyte interlayer," *J. Am. Chem. Soc*, vol. 133, pp. 8416–8419, 2011.

[92] L. Ye, Y. Jing, X. Guo, H. Sun, S. Zhang, M. Zhang, L. Huo, and J. Hou, "Remove the residual additives toward enhanced efficiency with higher reproducibility in polymer solar cells," *J. Phys. Chem. C*, vol. 117, pp. 14920–14928, 2013.

[93] D. Mühlbacher, M. Scharber, M. Morana, Z. Zhu, D. Waller, R. Gaudiana, and C. Brabec, "High photovoltaic performance of a low-bandgap polymer," *Adv. Mater.*, vol. 18, pp. 2884–2889, 2006.

[94] B. C. Thompson and J. M. Fréchet, "Polymer–fullerene composite solar cells," *Angew. Chem. Int. Ed.*, vol. 47, pp. 58–77, 2008.

[95] J. Szarko, J. Guo, Y. Liang, B. Lee, B. Rolczynski, J. Strzalka, T. Xu, S. Loser, T. Marks, L. Yu, and L. Chen, "When function follows form: Effects of donor copolymer side chains on film morphology and bhj solar cell performance," *Adv. Mater.*, vol. 22, pp. 5468–5472, 2010.

[96] F. C. Krebs and T. Jensen, "Fluorinated molecules relevant to conducting polymer research," *J. Fluor. Chem.*, vol. 120, pp. 77–84, 2003.

[97] H.-Y. Chen, J. Hou, S. Zhang, Y. Liang, G. Yang, Y. Yang, Y. Yu, L.and Wu, and G. Li, "Polymer solar cells with enhanced open-circuit voltage and efficiency," *Nature Photon.*, vol. 3, pp. 649–653, 2009.

[98] H. Zhou, L. Yang, A. Stuart, S. Price, S. Liu, and W. You, "Development of fluorinated benzothiadiazole as a structural unit for a polymer solar cell of 7% efficiency," *Angew. Chem. Int. Ed.*, vol. 50, pp. 2995–2998, 2011.

[99] S. Guo, J. Ning, V. Körstgens, Y. Yao, E. M. Herzig, S. V. Roth, and P. Müller-Buschbaum, "The effect of fluorination in manipulating the nanomorphology in ptb7:pc71bm bulk heterojunction system," *Adv. Energy. Mater.*, no. DOI: 10.1002/aenm.201401315, 2014.

[100] F. Liu, W. Zhao, J. R. Tumbleston, C. Wang, Y. Gu, D. Wang, A. L. Briseno, H. Ade, and T. P. Russell, "Understanding the morphology of ptb7:pcbm blends in organic photovoltaics," *Adv. Energy. Mater.*, vol. 4, no. DOI: 10.1002/aenm.201301377, 2014.

[101] S. Price, A. Stuart, L. Yang, H. Zhou, and W. You, "Fluorine substituted conjugated polymer of medium band gap yields 7polymer-fullerene solar cells," *J. Am. Chem. Soc.*, vol. 133, pp. 4625–4631, 2011.

[102] H. Zhou, Y. Zhang, J. Seifter, S. Collins, C. Luo, G. C. Bazan, T.-Q. Nguyen, and A. J. Heeger, "High-efficiency polymer solar cells enhanced by solvent treatment," *Adv. Mater.*, vol. 25, pp. 1646–1652, 2013.

[103] H. J. Son, W. Wang, T. Xu, Y. Liang, Y. Wu, G. Li, and L. Yu, "Synthesis of fluorinated polythienothiophene-co-benzodithiophenes and effect of fluorination on the photovoltaic properties," *J. Am. Chem. Soc.*, vol. 133, pp. 1885–1894, 2011.

[104] X. Fan, G. J. Fang, P. L. Qin, F. Cheng, and X. Zhao, "Rapid phase segregation of p3ht:pcbm composites by thermal annealing for high-performance bulk-heterojunction solar cells," *Appl. Phys. A.*, vol. 105, pp. 1003–1009, 2011.

[105] H. Tang, G. Lu, L. Li, Y. Wang, and X. Yang, "Precise construction of pcbm aggregates for polymer solar cells via multi-step controlled solvent vapor annealing," *J. Mater. Chem.*, vol. 20, pp. 683–688, 2010.

[106] B. A. Collins, Z. Li, E. Tumbleston, J. R.and Gann, C. R. McNeill, and H. Ade, "Absolute measurement of domain composition and nanoscale size distribution explains performance in ptb7:pc 71 bm solar cells," *Adv. Energy. Mater.*, vol. 3, pp. 65–74, 2013.

[107] J. Perlich, M. Memesa, A. Diethert, E. Metwalli, W. Wang, S. V. Roth, A. Timmann, and P. Gutmann, J. S.and Müller-Buschbaum, "Preservation of the morphology of a self-encapsulated thin titania film in a functional multilayer stack: An x-ray scattering study," *Chem. Phys. Chem.*, vol. 10, pp. 799–805, 2009.

[108] E. Ruderer, M.and Metwalli, W. Wang, G. Kaune, S. Roth, and P. Müller-Buschbaum, "Thin films of photoactive polymer blends," *Chem. Phys. Chem.*, vol. 10, pp. 664–671, 2009.

[109] R. Meier, H. Chiang, M. Ruderer, S. Guo, V. Körstgens, J. Perlich, and P. Müller-Buschbaum, "In situ film characterization of thermally treated microstructured conducting polymer films," *Polym. Phys.*, vol. 50, pp. 631–641, 2012.

[110] W. Krätschmer, L. D. Lamb, and D. Fostiropoulos, K.and Huffman, "Solid c60: a new form of carbon," *Nature*, vol. 347, pp. 354–358, 1990.

[111] E. Verploegen, R. Mondal, C. J. Bettinger, S. Sok, M. F. Toney, and Z. Bao, "Effects of thermal annealing upon the morphology of polymer-fullerene blends," *Adv. Funct. Mater.*, vol. 20, pp. 3519–3529, 2010.

[112] P. Kohn, S. Huettner, H. Komber, V. Senkovskyy, A. Tkachov, R.and Kiriy, R. H. Friend, U. Steiner, J. Huck, W.T.S.and Sommer, and M. Sommer, "On the role of single regiodefects and polydispersity in regioregular poly(3-hexylthiophene): Defect distribution, synthesis of defect-free chains, and a simple model for the determination of crystallinity," *J. Am. Chem. Soc.*, vol. 134, pp. 4790–4805, 2012.

[113] N. Treat, M. Brady, G. Smith, M. Toney, E. Kramer, C. Hawker, and M. Chabinyc, "Interdiffusion of pcbm and p3ht reveals miscibility in a photovoltaically active blend," *Adv. Energy. Mater.*, vol. 1, pp. 82–89, 2011.

[114] S. Albrecht, S. Janietz, W. Schindler, J. Frisch, J. Kurpiers, J. Kniepert, S. Inal, P. Pingel, K. Fostiropoulos, N. Koch, and D. Neher, "Fluorinated pcpdtbt with enhanced open circuit voltage and reduced recombination for highly efficient polymer solar cells," *J. Am. Chem. Soc.*, vol. 134, pp. 14932–14944, 2012.

[115] A. C. Tumbleston, J. R.and Stuart, E. Gann, and H. You, W.and Ade, "Fluorinated polymer yields high organic solar cell performance for a wide range of morphologies," *Adv. Funct. Mater.*, vol. 23, pp. 3463–3470, 2013.

[116] Y. Zhang, J. Zou, C.-C. Cheuh, H.-L. Yip, and A. K.-Y. Jen, "Significant improved performance of photovoltaic cells made from a partially fluorinated cyclopentadithiophene/benzothiadiazole conjugated polymer," *Macromolecules*, vol. 45, pp. 5427–5435, 2012.

[117] S. Guo, E. M. Herzig, A. Naumann, G. Tainter, J. Perlich, and P. Müller-Buschbaum, "Influence of solvent and solvent additive on the morphology of ptb7 films probed via x-ray scattering," *J. Phys.Chem. B*, vol. 118, pp. 344–350, 2014.

[118] S. Guo, M. A. Ruderer, M. Rawolle, V. Körstgens, C. Birkenstock, J. Perlich, and P. Müller-Buschbaum, "Evolution of lateral structures during the functional stack build-up of p3ht:pcbm based bulk heterojunction solar cells," *ACS Appl. Mater. Interfaces*, vol. 5, pp. 8581–8590, 2013.

[119] M. Rispens, A. Meetsma, R. Rittberger, C. Brabec, N. Sariciftci, and J. Hummelen, "Influence of the solvent on the crystal structure of pcbm and the efficiency of mdmo-ppv:pcbm plastic solar cells," *Chem. Commun.*, pp. 2116–2118, 2003.

[120] L. Ye, S. Zhang, W. Ma, B. Fan, X. Guo, Y. Huang, H. Ade, and J. Hou, "From binary to ternary solvent: Morphology fine-tuning of d/a blends in pdpp3t-based polymer solar cells," *Adv. Mater.*, vol. 24, pp. 6335–6341, 2012.

[121] F. Liu, J. W. Gu, Y.and Jung, W. H. Jo, and T. P. Russell, "On the morphology of polymer-based photovoltaics," *J. Polym. Sci. Part B Polym. Phys.*, vol. 50, pp. 1018–1044, 2012.

[122] Y. Yao, J. Hou, Z. Xu, G. Li, and Y. Yang, "Effects of solvent mixtures on the nanoscale phase separation in polymer solar cells," *Adv. Funct. Mater.*, vol. 18, pp. 1783–1789, 2008.

[123] J. K. Lee, C. J. Ma, W. L.and Brabec, J. Yuen, J. S. Moon, J. Y. Kim, K. Lee, G. C. Bazan, and A. J. Heeger, "Processing additives for improved efficiency from bulk heterojunction solar cells," *J. Am. Chem. Soc.*, vol. 130, pp. 3619–3623, 2008.

[124] H.-C. Liao, C.-C. Ho, C.-Y. Chang, M.-H. Jao, S. B. Darling, and W.-F. Su, "Additives for morphology control in high-efficiency organic solar cells," *Mater. Today*, vol. 16, pp. 326–336, 2013.

[125] P. A. Troshin, H. Hoppe, J. Renz, M. Egginger, J. Y. Mayorova, A. E. Goryachev, A. S. Peregudov, R. N. Lyubovskaya, G. Gobsch, N. Serdar Sariciftci, and V. F. Razumov, "Material solubility-photovoltaic performance relationship in the design of novel fullerene derivatives for bulk heterojunction solar cells," *Adv. Funct. Mater.*, vol. 19, pp. 779–788, 2009.

[126] P. A. Troshin, D. K. Susarova, E. A. Khakina, A. A. Goryachev, O. V. Borshchev, S. A. Ponomarenko, V. F. Razumova, and N. Serdar Sariciftci, "Material solubility and molecular compatibility effects in the design of fullerene/polymer composites for organic bulk heterojunction solar cells," *J. Mater. Chem.*, vol. 22, pp. 18433–18441, 2012.

[127] M. Hoppe, H.and Niggemann, C. Winder, J. Kraut, R. Hiesgen, A. Hinsch, D. Meissner, and N. Serdar Sariciftci, "Nanoscale morphology of conjugated polymer/fullerbased bulk-heterojunction solar cells," *Adv. Funct. Mater.*, vol. 14, pp. 1005–1011, 2004.

[128] G. J. Hedley, A. J. Ward, A. Alekseev, C. T. Howells, E. R. Martins, L. A. Serrano, G. Cooke, A. Ruseckas, and I. Samuel, "Determining the optimum morphology in high-performance polymer-fullerene organic photovoltaic cells," *Nat. Commun.*, vol. 4, no. doi:10.1038/ncomms3867, 2013.

[129] A. Diethert, Y. Peykova, N. Willenbacher, and P. Müller-Buschbaum, "Near-surface composition profiles and the adhesive properties of statistical copolymer films being model systems of pressure sensitive adhesive films," *ACS Appl. Mater. Interfaces*, vol. 2, no. 7, pp. 2060–2068, 2010.

[130] L.-M. Chen, Z. Xu, Z. Hong, and Y. Yang, "Interface investigation and engineering - achieving high performance polymer photovoltaic devices," *J. Mater. Chem.*, vol. 20, pp. 2575–2598, 2010.

[131] H. Li, L. Tang, H.and Li, W. Xu, X. Zhao, and X. Yang, "Solvent-soaking treatment induced morphology evolution in p3ht/pcbm composite films," *J. Mater. Chem.*, vol. 21, pp. 6563–6568, 2011.

[132] X. Liu, W. Wen, and G. C. Bazan, "Post-deposition treatment of an arylated-carbazole conjugated polymer for solar cell fabrication," *Adv. Mater.*, vol. 24, pp. 4505–4510, 2012.

[133] M. A. Ruderer, R. Meier, L. Porcar, R. Cubitt, and P. Müller-Buschbaum, "Phase separation and molecular intermixing in polymer–fullerene bulk heterojunction thin films," *J. Phys. Chem. Lett.*, vol. 3, pp. 683–688, 2012.

[134] S. Guo, B. Cao, W. Wang, and P. Müller-Buschbaum, "Efficiency enhancement of polymer solar cells introduced by alcohol solvent treatment," *Adv. Energy. Mater.*, no. Submitted, 2014.

[135] M. A. Ruderer and P. Müller-Buschbaum, "Morphology of polymer-based bulk heterojunction films for organic photovoltaics," *Soft Matter*, vol. 7, pp. 5482–5493, 2011.

[136] Y. Wang, Y. Liu, S. Chen, R. Peng, and Z. Ge, "Significant enhancement of polymer solar cell performance via side-chain engineering and simple solvent treatment," *Chem. Mater.*, vol. 25, p. 3196–3204, 2013.

[137] P. Müller-Buschbaum, M. Kaune, G.and Haese-Seiller, and J.-F. Moulin, "Morphology determination of defect-rich diblock copolymer films with time-of-flight grazing-incidence small-angle neutron scattering," *J. Appl. Cryst.*, vol. 47, pp. 1228–1237, 2014.

[138] P. Müller-Buschbaum, "Time-of flight grazing incidence small angle neutron scattering - a novel scattering technique for the investigation of nanostructured polymer films," *Euro. Phys. J.*, vol. 167, pp. 107–112, 2009.

[139] H. Dosch, "Critical phenomena at surface and interfaces: Evanescent x-ray and neutron scattering," *Springer-Verlag, Heidelberg*, vol. 126, 1992.

[140] L. Chang, H. W. A. Lademann, J.-B. Bonekamp, K. Meerholz, and A. J. Moulé, "Effect of trace solvent on the morphology of p3ht:pcbm bulk heterojunction solar cells," *Adv. Funct. Mater.*, vol. 21, pp. 1779–1787, 2011.

List of publications

Publications related to the dissertation

- S. Guo, E. M. Herzig, A. Naumann, G. Tainter, J. Perlich, P. Müller-Buschbaum: Influence of solvent and solvent additive on the morphology of PTB7 films; *J. Phys. Chem. B* **2014**, *118*, 344-350.
- S. Guo, J. Ning, V. Körstgens, Y. Yao, E. M. Herzig, S. V. Roth, P. Müller-Buschbaum: The effect of fluorination in manipulating the nanomorphology in PTB7:$PC_{71}BM$ bulk heterojunction system; *Adv. Energy. Mater.* **2014**, DOI: 10.1002/aenm.201401315.
- S. Guo, C. Brandt, T. Andreev, E. Metwalli, W. Wang, J. Perlich, P. Müller-Buschbaum: A first step into space: performance and morphological evolution of P3HT:PCBM bulk heterojunction solar cells under AM0 illumination; *ACS Appl. Mater. Interfaces* **2014**, DOI: 10.1021/am504608p.
- S. Guo, B. Cao, W. Wang, J.-F. Moulin, P. Müller-Buschbaum: Efficiency enhancement of polymer solar cells introduced by alcohol solvent treatment; *Adv. Energy. Mater.* **2014**, In review.
- S. Guo, E. M. Herzig, A. Naumann, J. Perlich, P. Müller-Buschbaum: Solvent-nanomorphology-properties relationship in polymer based solar cells; *Adv. Funct. Mater.* **2014**, To be submitted.
- S. Guo, M. A. Ruderer, M. Rawolle, V. Körstgens, C. Birkenstock, J. Perlich, P. Müller-Buschbaum: Evolution of lateral structures during the functional stack build-up of P3HT:PCBM-based bulk heterojunction solar cells; *ACS Appl. Mater. Interfaces* **2013**, *5*, 8581-8590.
- W. Wang, S. Guo, J. Perlich, P. Müller-Buschbaum: Morphological Investigation of P3HT:PCBM bulk heterojunction with long-term solvent vapor treatment; *Macromolecules* **2014**, To be submitted.

- M. A. Ruderer, S. Guo, R. Meier, H.-Y. Chiang, V. Körstgens, J. Wiedersich, J. Perlich, S. V. Roth, P. Müller-Buschbaum: Solvent induced morphology in polymer-based systems for organic photovoltaics; *Adv. Funct. Mater.* **2011**, *21*, 3382-3391.

Further publications

- E. Metwalli, I. Krisch, I. Markovits, M. Rawolle, M. A. Ruderer, S. Guo, J. Perlich, S. Wyrzgol, L. Johannes, P. Müller-Buschbaum: Polymer coated PtCo nanoparticles deposited on diblock copolymer templates: Chemical selectivity versus topographical effects; *ChemPhysChem* **2014**, DOI: 10.1002/cphc.201402047.

- M. Rawolle, V. Körstgens, M. A. Ruderer, E. Metwalli, S. Guo, G. Herzog, G. Benecke, M. Schwartzkopf, A. Buffet, J. Perlich, S. V. Roth, P. Müller-Buschbaum: Comparison of grazing incidence small angle x-ray scattering of a titania sponge structure at the beamlines BW4 (DORIS III) and P03 (PETRA III); *Rev. Sci. Instr.* **2012**, *83*, 106104-106105.

- V. Körstgens, R. Meier, M. A. Ruderer, S. Guo, H.-Y. Chiang, J. Perlich, S. V. Roth, R. Gehrke, P. Müller-Buschbaum: Grazing incidence small and wide angle x-ray scattering combined with imaging ellipsometry; *Rev. Sci. Instr.* **2012**, *83*, 076107-076108.

- R. Meier, H.-Y. Chiang, M. A. Ruderer, S. Guo, V. Körstgens, J. Perlich, S. V. Roth, P. Müller-Buschbaum: In situ film characterization of thermally treated microstructured conducting polymer films; *J. Poly. Sci. Part B.* **2012**, *50*, 631-641.

Scientific reports

- S. Guo, J. Ning, V. Körstgens,Y. Yuan , E. M. Herzig, S. V. Roth,J. Perlich, P. Müller-Buschbaum: The effect of fluorination in manipulating the nanomorphology in PTB7:PC_{71}BM BHJ system; *Lehrstuhl für Funktionelle Materialien, Annual report 2013.*

- S. Guo, A. Naumann, E. M. Herzig, G. Tainter, J. Perlich, P. Müller-Buschbaum: The effect of solvents in manipulating the nano-morphology in the PTB7:PC_{71}BM BHJ system; *HASYLAB, Annual report 2012.*

- S. Guo, J. Perlich, P. Müller-Buschbaum: The effect of solovents in manipulating the nanomorphology of PTB7:$PC_{71}BM$ BHJ system; *Lehrstuhl für Funktionelle Materialien, Annual report 2012.*

- S. Guo, C. Brandt, T. Andreev, M. A. Ruderer, E. Metwalli, W. Wang, K. H. Scherer, J. Perlich, P. Müller-Buschbaum: X-ray assisted investigation on degradation of P3HT:PCBM bulk heterojunction solar cells; *HASYLAB, Annual report 2011.*

- S. Guo, M. A. Ruderer, M. Rawolle, V. Körstgens, J. Perlich, S. V. Roth, P. Müller-Buschbaum: Evolution of lateral structures during the functional stack build-up of P3HT:PCBM based bulk heterojunction solar cells; *Lehrstuhl für Funktionelle Materialien, Annual report 2011.*

- S. Guo, M. A. Ruderer, P. Müller-Buschbaum: Influence of different solvents on the morphology in P3HT:PCBM bulk heterojunction systems for organic photovoltaics; *Lehrstuhl für Funktionelle Materialien, Annual report 2010.*

- S. Guo, M. A. Ruderer, E. Metwalli, M. Rawolle, P. Müller-Buschbaum: A systematic X-ray scattering study on bulk heterojunction P3HT:PCBM solar cells; *HASYLAB, Annual report 2010.*

Conference talks

- S. Guo, J. Ning, V. Körstgens, Y. Yao, E. M. Herzig, S. V. Roth, P. Müller-Buschbaum: Influence of fluorine content in manipulating nanomorphology of PTB7-PCBM bulk heterojuntion systems; *DPG Frühjahrstagung*, Regensburg (Germany), March 2013.

- S. Guo, P. Müller-Buschbaum: Application of scattering techniques in investigating the nanomorphology of high efficient organic photovoltaics; *The delegation of Tsinghua University at TUM*, Garching (Germany), July 2013.

- S. Guo, P. Müller-Buschbaum: Novel polymer for high efficient organic solar cells; *Seminar für Lehrstuhl für Funktionelle Materialien*, Garching (Germany), June 2012.

- S. Guo, Polymer-based Solar Cells; *summer school*, Rudolfshütte (Austria), June 2012.

- S. Guo, P. Müller-Buschbaum: Novel polymer for high efficient organic solar cells; *Seminar für Lehrstuhl für Funktionelle Materialien*, Garching (Germany), June 2013.

Conference poster presentations

- S. Guo, B. Cao, W. Wang, J.-F. Moulin, P. Müller-Buschbaum: Efficiency enhancement of polymer solar cells introduced by alcohol solvent treatment; *DPG Frühjahrstagung*, Dresden (Germany), 31 Mar - 4 April 2014.

- S. Guo, J. Ning,V. Körstgens,Y. Yuan, S. V. Roth, P. Müller-Buschbaum: Influence of fluorine content in manipulating nanomorphology of PTB7:PCBM bulk heterojuntion systems; *NIM workshop "Young ideas in nanoscience"*, Hanns-Seidel-Stiftung (Germany), 19 - 20 November 2013.

- S. Guo, J. Ning,V. Körstgens,Y. Yuan, S. V. Roth, P. Müller-Buschbaum: Influence of fluorine content in manipulating nanomorphology of PTB7:PCBM bulk heterojuntion systems; *Nanosystems for the solar cell*, Ludwig-Maximilians-Universität München (Germany), 24 - 26 July 2013.

- S. Guo, J. Ning,V. Körstgens,Y. Yuan, S. V. Roth, P. Müller-Buschbaum: Influence of fluorine content in manipulating nanomorphology of PTB7:PCBM bulk heterojuntion systems; *3rd Colloquium of the Munich School of Engineering*, kloster banz (Germany), Garching (Germany), 4 Jul 2013.

- S. Guo, J. Ning,V. Körstgens,Y. Yuan, S. V. Roth, P. Müller-Buschbaum: Influence of fluorine content in manipulating nanomorphology of PTB7:PCBM bulk heterojuntion systems; *solartech go hybrid*, kloster banz (Germany), 11 - 13 April 2013.

- S. Guo, E. M. Herzig, A. Naumann, J. Perlich, P. Müller-Buschbaum: solvent induced nanomorphology of PTB7:PCBM bulk heterojuntion systems; *Tag der Physikerin*, Garching (Germany), 08 Feb 2013.

- S. Guo, M. A. Ruderer, M. Rawolle, V. Körstgens, J. Perlich, P. Müller-Buschbaum: A systematic X-ray scattering study on highly efficient bulk heterojuntion P3HT:PCBM solar cell; *DPG Frühjahrstagung*, Berlin (Germany), 25 - 30 Mar 2012.

- S. Guo, M. A. Ruderer, M. Rawolle, V. Körstgens, J. Perlich, P. Müller-Buschbaum: A systematic X-ray scattering study on highly efficient bulk heterojuntion P3HT:PCBM solar cell; *Tag der Physikerin*, Garching (Germany), 15 Feb 2012.

- S. Guo, M. A. Ruderer, R. Meier, H-Y. Chiang, S. V. Roth, J. Perlich, P. Müller-Buschbaum: Influence of different solvents on morphology in P3HT:PCBM bulk heterojunction systems for organic photovoltaics; *1st Colloquium of the Munich School of Engineering*, Garching (Germany), 18 Jul 2011.

- S. Guo, M. A. Ruderer, M. Rawolle, V. Körstgens, J. Perlich, P. Müller-Buschbaum: A systematic X-ray scattering study on highly efficient bulk heterojuntion P3HT:PCBM solar cell; *5th FRM II Science Meeting*, Burg Rothenfels (Germany), 06 - 09 Jun 2011.

- S. Guo, M. A. Ruderer, R. Meier, H-Y. Chiang, S. V. Roth, J. Perlich, P. Müller-Buschbaum: Influence of different solvents on morphology in P3HT:PCBM bulk heterojunction systems for organic photovoltaics; *DPG Frühjahrstagung*, Dresden (Germany), 13 - 18 Mar 2011.

- S. Guo, M. A. Ruderer, R. Meier, H-Y. Chiang, S. V. Roth, J. Perlich, P. Müller-Buschbaum: Influence of different solvents on morphology in P3HT:PCBM bulk heterojunction systems for organic photovoltaics; *HASYLAB User Meeting*, Hamburg (Germany), 27 - 28 Jan 2011.

Acknowledgments

I would like to thank Prof. Dr. Peter Müller-Buschbaum for giving me the opportunity to continue my work in the field of organic photovoltaics after my master thesis. I appreciate his open mind and high sense of responsibility to every student in the big group. His foreseeing point of view and abundant experience on scattering techniques greatly helped me throughout my Ph.D. period. I benefit a lot from all the extensive discussions. Also, I am very grateful for his trust in me so that I have the chances to supervise master students, to take responsibility for AFM laboratory course, and to participate in reviewing scientific publications. I highly appreciate the opportunities that he offered me to collaborate with Dr. Thomas Andreev and Christian Brandt from Airbus Defence and Space. I had very pleasant time working in EADS, and it was very precious experience for me to visit and perform experiments in a company. Additionally, financial support by TUM. solar in the frame of the Bavarian Collaborative Research Project "Solar Technologies go Hybrid" (SolTech) and by the GreenTech Initiative (Interface Science for Photovoltaics - ISPV) of the EuroTech Universities is greatly acknowledged.

I would like to thank Matthias A. Ruderer for his supervision during my master thesis time. His attitude toward research always inspired me through my whole Ph.D. period. Thanks very much for your patience and instant help anytime I asked.

Many thanks to my four wonderful master students and one working student: Jing Ning, Christian Jendrzejewski, Biye Cao, Rosa M. Torrademé, and Rui Wang. I had great time with Jing Ning during her whole master period. Her efficient work and specialty at preparing the presentation motivated me all the time. I'm very content with the topic I worked together with Biye. His serious attitude towards research and the promising results inspired me all the time. Rosa's diligent working attitude impressed me a lot. Christian's curiosity stimulated me to understand every detail thoroughly. I wish all the best for all of them.

Tremendous thanks go to my officemate David Magerl for his help in every aspect of life, especially for his special knowledge of writing macros for everyone in this Chair, and you are the best officemate ever! I'd like to thank all the beamtime partners in the past

4 years: I feel very honored to have a chance to be in a team with Dr. Volker Körstgens, Dr. Robert Meier, Dr. Hsin-Yin Chiang, Dr. Matthias A. Ruderer, Dr. Monika Rawolle, Dr. Ezz Metwalli, Weijia Wang, Dr. Eva M. Herzig, Gregory Tainter in BW4, DESY, Hamburg, and with Dr. Eva M. Herzig, Markus Schindler at ILL, Switzerland. I am more than grateful to Dr. Kuhu Sarkar for replacing me for one beamtime while I was ill. Great thanks also come to Christoph J. Schaffer, who replaced me for ILL beamtime due to my illness and helped me with physics and Python problems any time I asked. In addition, I would like to thank all the people who helped me to proofread my thesis: Dr. Volker Körstgens, Dr. Matthias A. Ruderer, Weijia Wang, Christoph J. Schaffer, Dr. Ezz Metwalli, Dr. Martine Philipp, Dr. Eva M. Herzig, and Stephan Pröller. All your corrections are really helpful for transforming my thesis to a better quality. I'm very thankful to Prof. Christine Papadakis for a lot interesting talks about science and daily life. I sincerely thank Prof. Martin Zacharias and Prof. Martin S. Brandt for their kind help so that I could happily finish my Ph.D. studies. Many thanks come to Dr. Martin A. Niedermeier and Dr. Volker Körstgens, who always listened to my problems and gave their wonderful suggestions in the past four years. Besides, I also would like to give my special thanks to our secretary Susanna Fink, Marion Waletzki, and Petra Douglas. They have done so much to help me go through all the Visa and organization problems. Moreover, I want to thank Dieter Müller for his help for fixing my computer problems all the time. Many thanks for all of your kind and always instant help in the past four years. I also want to thank all the other former and present members of Lehrstuhl für Funktionelle Materialien: Dr. Jan Perlich, Dr. Weinan Wang, Dr. Alexander Diethert, Dr. Qi Zhong, Dr. Jianqi Zhang, Wei Liu, Minglong He, William Hefter, Erik Braden, Anna Naumann, Majid Rasool, Daniel Moseguí González, Lin Song, Yuan Yao, Su Bo, Claudia Palumbiny, Johannes Schlipf, Nuri Hohn, Tobias Widmann, Felipe Martinez, Konstantinos Kyriakos, Natalya Vishnevetskaya, Margarita Dyakonova. All of them provided me a very friendly environment to work. I wish all my beloved colleagues a very happy life.

I'd like to give my sincere thanks to my flatmates Ralf Dahlhaus and Janine Aigner. Ralf Dahlhaus, his kindness, unique opinions about life, and great experience help me live in Munich with so much laughter. Janine's independence impresses me every day, and I would very much like to learn from her. She is the smartest girl I know so far. Janine, I'll send you message one day in the future when I can speak German (fluently), French, and Spanish. You two always provide me such a sweet home in Munich, and I really enjoy and appreciate it so much! I'm thankful to Qi Zhong for his delicious dishes and nice movies from time to time. I thank Weijia a lot for her thoughtful suggestions and kind help both with work and my daily life. I'm really touched everytime when I think of that you accompanied me for the whole operation day in the hospital. Also, I want to

thank my “families” in Munich: Hsin-Yin for listening to me any time I need, and her self-confidence, independence, and good sense of humor inspire me all the time. Hsin-Yin, we did it! I appreciate Kuhu’s help during my frequent moving, and sweet accompany in the past four years. A lot thanks go to David Behel and Nindiyasari Fitriana. All of them keep me away from feeling lonely and we had many great birthdays, Christmas, New Year’s Parties. I’m very grateful to Dr. Axel Strehle, who gave me lots of care and spiritual supports when I was ill in the long winter 2012. I wish a glorious cardiology career in front of you. Many thanks to my friend Kun Zhai, who took very good care of me during my operation in 2013. Thanks to my other international friends in Munich: Kie Norie, Mathias Götz, Fedor Baklanov, Jonny Elliott, Jochen Schönweiß, Sofia Ramirez, Zhehan Shang. I enjoyed my life so much with their companion.

I want to thank my parents for their supports and encouragements all the time, my sister and brother-in-law for taking best care of me while I was ill, and my younger brother for his abundant concerns and suggestions. I love my families so much, and always feel so warm in my heart every time when I think of them. I wish more and more happiness and success for everyone.

Last but not the least, I want to thank my soulmate Dr. Lin Yang for tons of discussions about life, work, and everything. Thank you for calming me down when I was furious, lighting me up when I was down, giving me hope when I felt lost and confused, and accepting me for the way I am. From you, I keep receiving positive energy and stay optimistic. Life is beautiful! Thank you!